

Processing Case Study with AVO and Pore Pressure Analyses: Eugene Island,
Gulf of Mexico

by
Christine Kuo

A thesis submitted to the Department of Earth and Atmospheric Sciences
in partial fulfillment of the requirements for the degree of

Master of Science

in Geophysics

Chair of Committee: Hua-Wei Zhou

Committee Member: Fred Hilterman

Committee Member: Jiajia Sun

Committee Member: Richard Verm

University of Houston

December 2019

ACKNOWLEDGEMENTS

I would like to take a moment to thank everyone who has helped me through this thesis, it's been a journey and I'm extremely thankful to those who supported me along the way. First and foremost, I'd like to thank my advisor Dr. Fred Hilterman, who would always take time out to meet whenever I needed guidance both in direction and with technical advice when using well log analysis programs such as JTIPs. Without whom I would not have been able to overcome all these hurdles that have presented themselves over the years and complete this thesis.

I'd like to thank Fairfield Industries for providing the seismic dataset, and Geokinetics Inc. (now SAExploration) for the well-log curves used in this research. I would also like to thank Geosystem Development Corporation for allowing me the use of GBSYS for processing.

Next, I'd like to thank the rest of my committee team, Dr. Hua-Wei Zhou, Dr. Jia-Jia Sun, and Dr. Richard Verm. First of all, I'd like thank Dr. Zhou, who pushes me to achieve a higher quality in my work, I am thankful for your high expectations that push me to achieve more than I thought possible. Next, I'd like to thank Dr. Sun, who so graciously came onto my committee team during my time of need, I am incredibly thankful for your generosity and kindness. I'd also like to thank Dr. Richard Verm, who's expertise in the field provides invaluable insight that I can apply to make my research more applicable for those who would use it as a guideline in seismic processing.

Finally, I'd like to thank my family. My mother for the ever-constant emotional support, even when I'm feeling defeated. I'd like to thank my father for his own knowledge and experience in the field, and for his unwavering support and certainty in my future. Last, but not least, I'd like to thank my brother, when we were younger, I always knew family was important, but with the amount of support and help you've given me without ever complaining has shown

me just how truly lucky I am to have you on my team, you've gone above and beyond and I hope one day I can repay it in kind, thank you kiddo. I couldn't have done this without any of you, and I thank you all deeply.

ABSTRACT

Seismic exploration uses numerous tools and techniques for detecting hydrocarbon reservoirs in conventional plays as found on the shelf of the northern Gulf of Mexico (GOM). The tools include seismic data-processing attributes, well-log calibration, and AVO (Amplitude Versus Offset) and pore pressure analyses. While the supporting theory for each method has been well established, an integration of the methods to a real exploration project can be confusing for the uninitiated. Given a seismic dataset and well-log curves, how exactly would someone process and analyze the data using the techniques listed? This research proposes a practical workflow for creating an end product for exploration applications.

Using a seismic dataset in the GOM and several well log datasets, an integration of the processed seismic image with pore pressure analysis, petrophysical analysis and calibrated seismic attributes derived from the petrophysical analysis indicates the area would be classified as a Class III AVO environment which is supported by the geologic background. The dataset is further processed to completion and then used to generate AVO and pore pressure fields. Available well logs in the area are then compared and tied to the seismic, in order to validate the presence of any potential hydrocarbon attributes. An abnormal overpressure zone is determined by seismic velocity analysis and confirmed by the structural continuity of reflections, which was bound within a fault block. The seismic attributes indicated a potential gas reservoir on the downthrown side of the fault block, which would correlate with the proximity of the abnormal pressure. The exploration tools of seismic data analysis, well log analysis, AVO analysis, and pore pressure analysis are found to be strongly correlated by this study.

TABLE OF CONTENTS

ACKNOWLEDGEMENTS	i
ABSTRACT.....	iv
TABLE OF CONTENTS	v
LIST OF TABLES	viii
LIST OF FIGURES	ix
1. INTRODUCTION.....	1
1.1 AVAILABLE DATA.....	1
1.2 SOFTWARE USED.....	2
1.3 EUEGENE ISLAND / SOUTH MARSH ISLAND SURVEY AREA	2
1.3.1 GEOLOGY BACKGROUND.....	3
1.4 WELL-LOG ANALYSIS	8
1.4.1 HYDROCARBON INDICATORS FROM WELL LOGS.....	8
1.4.2 WATER SATURATION AND POROSITY ESTIMATIONS.....	8
1.4.3 WELL LOCATIONS.....	11
1.4.4 WELL LOG CURVES AND CROSSPLOTS.....	13
1.5 AVO ANALYSIS	25
1.5.1 INTRODUCTION	25
1.5.2 AVO ATTRIBUTES	27
1.6 PORE PRESSURE ANALYSIS	31
1.6.1 INTRODUCTION	31
1.6.2 PORE PRESSURE TERMINOLOGY	31
1.6.3 UNIT CONVENTION.....	33

1.6.4	OVERPRESSURE IN THE GULF OF MEXICO	34
1.6.5	EMPIRICAL METHODS FOR PORE PRESSURE ESTIMATION	37
1.6.6	EFFECT OF PRESSURE ON SEISMIC VELOCITY.....	39
2.	PROJECT WORKFLOW.....	40
2.1	PROCESSING DESCRIPTION	45
2.1.1	TRACE EDITING	45
2.1.2	DECONVOLUTION	45
2.1.3	STATICS CORRECTION (ELEVATION AND RESIDUAL).....	46
2.1.4	RANDOM SPIKE NOISE ATTENUATION	46
2.1.5	DATA INTERPOLATION AND REGULARIZATION.....	46
2.1.6	CMP GATHER.....	47
2.1.7	NMO CORRECTION.....	47
2.1.8	VELOCITY ANALYSIS.....	47
2.1.9	STACK	49
2.1.10	MIGRATION.....	49
2.1.11	ANGLE MUTE.....	51
2.1.12	RADON FILTER.....	52
2.1.13	FX COHERENCY FILTER	52
2.1.14	RESIDUAL VELOCITY ANALYSIS (AVEL).....	52
3.	PROCESSING RESULTS AND INTERPRETATION	53
3.1	PROCESSING QUALITY CONTROL.....	53
3.2	VELOCITY ANALYSIS COMPARISON.....	59
3.3	STACK COMPARISON	66
3.4	ANGLE GATHERS AND STACKS.....	76

3.5	FAULT DISCRIMINATION.....	85
3.6	AVO PROCESSING OUTPUTS.....	89
3.7	PORE PRESSURE PROCESSING OUTPUTS	91
3.8	COMPILING THE RESULTS.....	94
4.	DISCUSSION AND CONCLUSION	100
	BIBLIOGRAPHY.....	102

LIST OF TABLES

Table 1 Seismic acquisition parameters.....	2
Table 2 Characteristics of the four AVO Classes. (Rutherford and Williams 1989, Hilterman 2001, Castagna and Swan 1997).....	27
Table 3 Range of angles used for creating different angle gathers.....	51

LIST OF FIGURES

Figure 1.1 EI 26 survey area indicated by green rectangle. Each side of a block is 3 miles, and the entire survey consists of about 7.1 blocks..... 3

Figure 1.2 Bathymetry map of the GOM with EI 26 survey labeled by red rectangle. The south-east area of the 3D survey is in 6-m water depth. (ngdc.noaa.gov)..... 5

Figure 1.3 (A) Regional map with orientation of cross sections (B) and (C) outlined in black. The black inverted triangles at the top of cross sections (B) and (C) indicate the coast boundary. EI 26 area indicated by red rectangle. (Morris et al. 2015) 6

Figure 1.4 (A) Depth map to onset of abnormal pore pressure for the Gulf of Mexico (B) 3D map of constant pore pressure gradient (0.70 psi/ft) in the Gulf of Mexico, and (C) Cross section for red line shown in (A). 7

Figure 1.5 EI 26 (green) survey area with available well-log locations (red dots). The well numbers are unique identifiers assigned by Geokinetics..... 12

Figure 1.6 Well-log curves from Well 3149, from left to right: Gamma, Sand Volume, Neutron + Density Porosity, Resistivity, Spontaneous Potential, Sonic Estimate, and Water Saturation. Blue blocks on the right side indicate porous sand intervals..... 17

Figure 1.7 Well log curves from Well 6976, from left to right: Gamma, Sand Volume, Resistivity, Neutron + Density Porosity, Spontaneous Potential, P-wave velocity, and Water Saturation. Blocks on the right side indicate sands with different pore fluids (red = gas, blue = water). 18

Figure 1.8 Fluid substitution and crossplots derived from Well 6976. For the seismic attribute curves, red indicates gas sands, and blue indicates brine sands. In the lithology crossplots along the bottom, red (+) signs are hydrocarbons, yellow (+) signs are sands, grey (+) signs are shale, and blue (+) signs are brine..... 19

Figure 1.9 Seismic attribute crossplots derived from Well 6976. For the seismic attribute curves, red indicates gas sands, and blue indicates brine sands. For the seismic attribute crossplots, red (+) signs are gas sands, magenta (o) signs are shale, and blue (o) signs are brine sands 20

Figure 1.10 Seismic bandwidth filtered attributes derived from Well 6976. For the seismic attribute curves, red indicates gas sands, and blue indicates brine sands. For the seismic attribute crossplots, red (+) signs are gas sands, magenta (o) signs are shale, and blue (o) signs are brine sands..... 21

Figure 1.11 Seismic bandwidth filtered attributes derived from Well 6976, with a phase distortion of 70 degrees. For the seismic attribute curves, red indicates gas sands, and blue indicates brine sands. For the seismic attribute crossplots, red (+) signs are gas sands, magenta (o) signs are shale, and blue (o) signs are brine sands 22

Figure 1.12 Crossplot comparison from Figure 1.8, Figure 1.9, Figure 1.10, and Figure 1.11 (from top-down respectively) with the same focus window. The crossplots of the filtered seismic (second to bottom row) are tangled together and difficult to discriminate pore fluid or lithology in comparison to the crossplots at well log resolution (top row). The gas clusters are indicated by the red circles. 23

Figure 1.13 Reflectivity NIP crossplots indicating the presence of Class III reflections based on the positions of hydrocarbons vs. sands, red (+) signs are gas sands, magenta (o) signs are shale, and blue (o) signs are brine sands. Red ovals outline Class III reflection zones..... 24

Figure 1.14 Reflection coefficient vs. incident angle for four classes of AVO (Hilterman 2001)29

Figure 1.15 AVO class responses to brine vs. gas signatures. (Hilterman 2001)..... 29

Figure 1.16 AVO classes in terms of the intercept (A) and gradient (B) terms. (Zhang and Brown 2001) 30

Figure 1.17 Gradient vs. Intercept AVO response for brine and gas-saturated sands (Hilterman 2001, Castagna and Swan, 1997).....	30
Figure 1.18 Theoretical relationship between pore pressure, fracture gradient, hydrostatic gradient, mud weight, and overburden gradient (black curve) (Bruce et al 2002).....	34
Figure 1.19 (a) Pressure vs. depth plot of a hypothetical well with a decrease in effective pressure, (b) velocity trend in a well with abnormal pressure caused by smectite-to-illite transformation (Hilterman 2001).....	36
Figure 1.20 Different overpressure mechanisms' effect on effective stress, overburden minus pore pressure (Bowers et al. 2001)	36
Figure 1.21 Depth of geopressure onset (a), corresponding sand percentages (b) for 7000-8000 feet (2000-2500 m) depths. Red contour represents 8000 feet (2500 m) contour line for the onset depth of abnormal pore pressure (Hilterman 2001).....	37
Figure 2.1 Fairfield preprocessing workflow for the EI 26 survey dataset.	41
Figure 2.2 Seismic data processing workflow for EI 26.....	42
Figure 2.3 AVO processing workflow for EI 26	43
Figure 2.4 Pore pressure processing workflow for EI 26	44
Figure 2.5 Comparison of four types of migration methods based on how they handle dip, lateral velocity changes, and cost (Zhou 2014, Liner 1999).....	51
Figure 3.1 EI 26 Fold map. Fold ranges between 0 to 70. Red rectangle represents the area of the survey being processed.	55
Figure 3.2 EI 26 Fold map with the survey line placement overlaid on top. Some lines have irregularities in their placement, but overall the lines are sufficiently straight and evenly spaced.	56

Figure 3.3 EI 26 Single shot display. A shot is indicated with the red circle and active receivers are blue dots. 57

Figure 3.4 Preprocessed CDP gather with statics and deconvolution pre-applied by Fairfield where there are (A) data spikes which need to be attenuated, and (B) muted (empty) traces which were removed previously by Fairfield. 58

Figure 3.5 Initial interval velocity picking panel with semblance gather (left) and CDP gather (right) with NMO correction applied based on picks. The semblance gather only shows a faint trend, likely due to high noise in the CDP gather. 61

Figure 3.6 Final PSTM interval velocity picking panel with semblance gather (left) and CDP gather (right) with NMO correction applied based on picks. (A) indicates a high coherency zone in the semblance gather, which overall has noticeably stronger peaks and a clearer trend. 62

Figure 3.7 Final PSDM interval velocity picking panel with semblance gather (left) and CDP gather (right) with NMO correction applied based on picks. The PSDM semblance gather shows an improved coherency trend over PSTM. Red box indicates top of geopressure. 63

Figure 3.8 Smoothed interval velocity field from Kirchhoff PSTM velocity analysis. The main feature is the low velocity zone in the center of the field. Otherwise, the velocity trend is largely smooth in the vertical and lateral sense. 64

Figure 3.9 Smoothed interval velocity field from Kirchhoff PSDM velocity analysis. Compared to the PSTM velocity model, the PSDM velocity field shows a more nuanced low velocity zone at around the same time. 65

Figure 3.10 Preprocessed EI 26 stack. Due to the complex structures below ~3.5 seconds, there are many event crossovers (A). Pre-stack migration should be able to correct these and improve the reflection events. Bottom of the dataset (B) shows some artifacts, possibly instrument noise

during field recording. Overall quality of the section is decent and provides a broad perspective of the subsurface structure. 67

Figure 3.11 PSTM full stack section. Three faults (1), (2), and (3) are now identifiable from the stack. 68

Figure 3.12 PSDM full stack section. Compared to the PSTM, events and signals have been boosted without any significant structural changes. The three faults are now more easily resolved. 69

Figure 3.13 Preprocessed stack (top) and PSTM stack (bottom) from 1.0-3.5 seconds. From the PSTM section, three major faults are distinguishable while these are present but obscure and difficult to trace in the preprocessed section..... 70

Figure 3.14 Preprocessed stack (top) and PSTM stack (bottom) from 3.0-5.5 seconds. This time interval contains more complex geology and the preprocessed section has poor image quality in this area. After PSTM, amplitudes and continuity across the section is greatly improved, and fault dipping to the south also becomes visible. The preprocessed stack also contains false events known as the “bow-tie effect”, an error caused by reflections from synclines. These have been corrected by migration as well. 71

Figure 3.15 Preprocessed stack (top) and PSTM stack (bottom) from 0.0-1.5 seconds. Because the survey was performed via OBC in a very shallow marine environment, the top of the sections does not display the typical ocean bottom reflection seen in marine surveys. Instead it appears more similar to land data. Due to low signal quality from the unconsolidated sediments on the ocean floor, the top of the section is unclear across both sections. 72

Figure 3.16 PSTM stack (top) and PSDM stack (bottom) from 1.0-3.5 seconds. 73

Figure 3.17 PSTM stack (top) and PSDM stack (bottom) from 3.0-5.5 seconds. 74

Figure 3.18 PSTM stack (top) and PSDM stack (bottom) from 0.0-1.5 seconds.	75
Figure 3.19 PSTM full angle CDP gather.....	78
Figure 3.20 PSTM angle gathers from 0 to 15 degrees	79
Figure 3.21 PSTM angle gathers from 15 to 30 degrees	80
Figure 3.22 PSTM angle gather from 30 to 70 degrees.....	81
Figure 3.23 PSTM angle stack from 0 to 15 degrees.....	82
Figure 3.24 PSTM angle stack from 15 to 30 degrees, the arrows indicate flat spots.....	83
Figure 3.25 PSTM angle stack from 30 to 70 degrees, the arrows indicating flat spots	84
Figure 3.26 PSTM stack section with interpreted fault lines in black.	86
Figure 3.27 Time slice through the 3D stack volume at 1.9 seconds with interpreted faults in black.....	87
Figure 3.28 Time slice through the PSTM 3D volume at 5.8 seconds depth. A large syncline structure is observable and outlined with a black circle.	88
Figure 3.29 Well 3149 AVO (A*B) response	90
Figure 3.30 Bower's Method - Well 3149 pore pressure gradient field	92
Figure 3.31 Eaton's Method - Well 3149 pore pressure gradient field	93
Figure 3.32 Time slice through PSTM stack section at 2.1 seconds with well locations marked.	95
Figure 3.33 Well 3149 well-tie with processed seismic data from Inline 2230.	96
Figure 3.34 Velocity field tie with interpreted fault locations. Low velocity zone outlined in black.....	97
Figure 3.35 AVO A*B section tie with low velocity zone (black) and fault (yellow) locations..	98
Figure 3.36 Full stack section with low velocity zone and fault locations annotated	99

ABBREVIATIONS

EI	Eugene Island	R_t	True Formation Resistivity
GOM	Gulf of Mexico	R_o	Brine-saturated Formation Resistivity
S_w	Water Saturation	R_w	Formation Water Resistivity
n	Saturation Exponent	ρ_{LOG}	Density-log Value
ϕ	Porosity	ρ_{GR}	Grain Density
$\phi_{neutron}$	Neutron Porosity	ρ_{FL}	Fluid Density
$\phi_{density}$	Density Porosity	m	Cementation Exponent
RC	Reflection Coefficient	AI	Acoustic Impedance
ϕ	Angle of Incidence	SI	Shear Impedance
A	Intercept	V_p	P-wave Velocity
B	Gradient/Slope	V_s	S-wave Velocity
C	Curvature	PP	Pore Pressure
OBG	Overburden Gradient	S	Overburden Stress
P_{hyd}	Normal Hydrostatic Pressure	Δt_{log}	Measured Sonic Log Value
Δt_n	Normal Sonic Log Value	x	Regional Constant
CDP	Common Depth Point	NMO	Normal Moveout
PSTM	Pre-Stack Time Migration	PSDM	Pre-Stack Depth Migration
AVA	Amplitude Versus Angle	AVO	Amplitude Versus Offset
OBC	Ocean Bottom Cable		

1. INTRODUCTION

This work presents a case study of the Eugene Island region in the Gulf of Mexico by using a combination of seismic data processing, AVO analysis, well log analysis, and pore pressure analysis. Each of these analysis techniques are widely used in exploration to search for potential hydrocarbons but they are often studied on an individual basis. The objective of this study is an integration of the above techniques with a field study and demonstrate how these techniques function together.

1.1 AVAILABLE DATA

A seismic dataset with limited processing was provided by Fairfield Industries and the well-log curves were supplied by Geokinetics Inc. (now SAExploration). Details concerning the seismic dataset are given in Table 1. The Eugene Island dataset is referred to as EI 26 for convenience since the center of the survey lies inside Eugene Island Block 26.

The marine field acquisition generated a narrow-azimuth survey since two active receiver lines were positioned 1650-ft apart and five source lines at 330-ft spacing were shot between the receiver lines. The receivers were hydrophones positioned near the ocean bottom. Both the source and receiver lines were essentially perpendicular to the shore line and often reached lengths of 75 miles with all receivers active during acquisition.

Additionally, approximately 40 suites of well-log data located in EI 26 area were made available. Unfortunately, some logs were missing either depth intervals of data, entire log curves, or even both. Wells used for the seismic-well tie were selected based on reasonably complete logs with an acceptable depth range and the availability of important and relevant well-log

curves. For the most part, the potential well logs available consisted of the gamma ray, spontaneous potential, sonic, bulk density, neutron porosity, resistivity, and computed sand-percentage curves.

Eugene Island/South Marsh Island Survey	
Info\Area	La., EI 26
X	1825492-1874992
Y	257065-221095
Inline	2119-2338
Xline	800-1700
Inline Interval	1
Xline Interval	1
Inline Spacing (ft)	165
Xline Spacing (ft)	55
Area (mi²)	64
Blocks (mi²)	7.1
Sample Rate (ms)	4
Nyquist (Hz)	125
Trace Length (s)	7.8

Table 1 Seismic acquisition parameters

1.2 SOFTWARE USED

The workflow utilized PetroSeismic Software’s **JTIPS Well Log Modeler** for well-log loading, editing and analyses; **MATLAB** for miscellaneous plotting tasks and calculations; **QGIS** for survey mapping and locating wells; **Kingdom** for certain interpretation plots; and Geosystem Development Corporation’s **GBSYS** processing suite for seismic data QC, data processing, migration, AVO analysis, and pore pressure analysis.

1.3 EUEGENE ISLAND / SOUTH MARSH ISLAND SURVEY AREA

Located south of Louisiana in the GOM, the EI 26 survey (Figure 1.1) covers regions from both the Eugene Island and South Marsh Island protracted areas. The survey coordinate system is defined under the Louisiana South FIPS NAD27 (US Feet) projection system. The shot and receiver lines are orthogonal to each other.

From the bathymetry shown in Figure 1.2, the water depth for EI 26 ranges between 3-6 meters (10-20 feet) deep. Shallow marine data often introduce processing obstacles due to strong multiple responses.

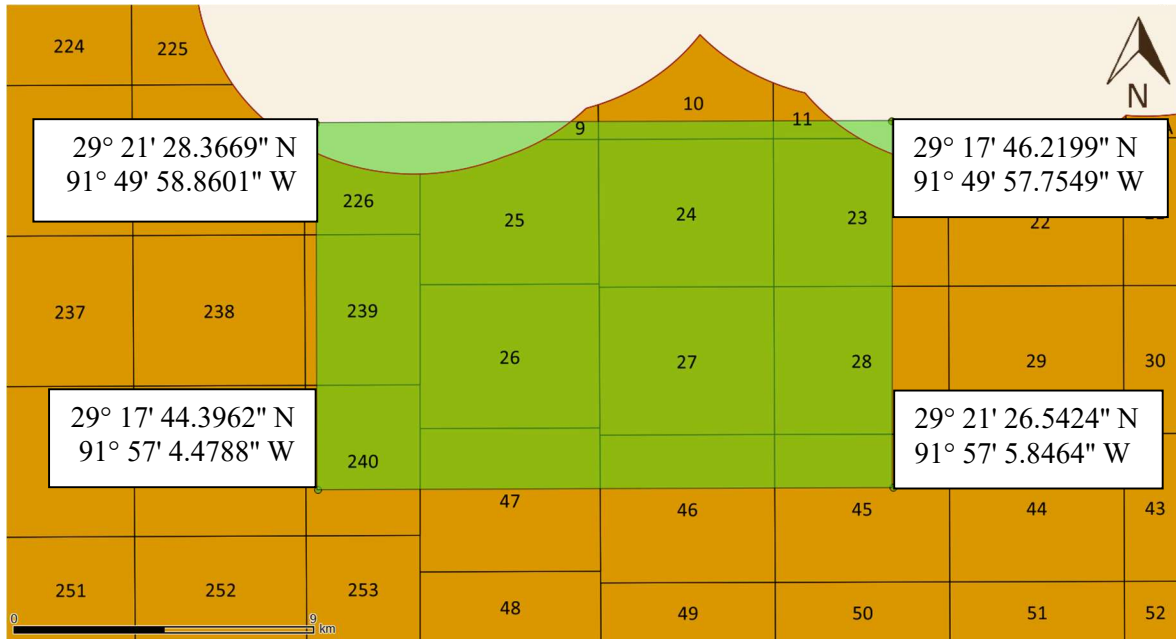


Figure 1.1 EI 26 survey area indicated by green rectangle. Each side of a block is 3 miles, and the entire survey consists of about 7.1 blocks

1.3.1 GEOLOGY BACKGROUND

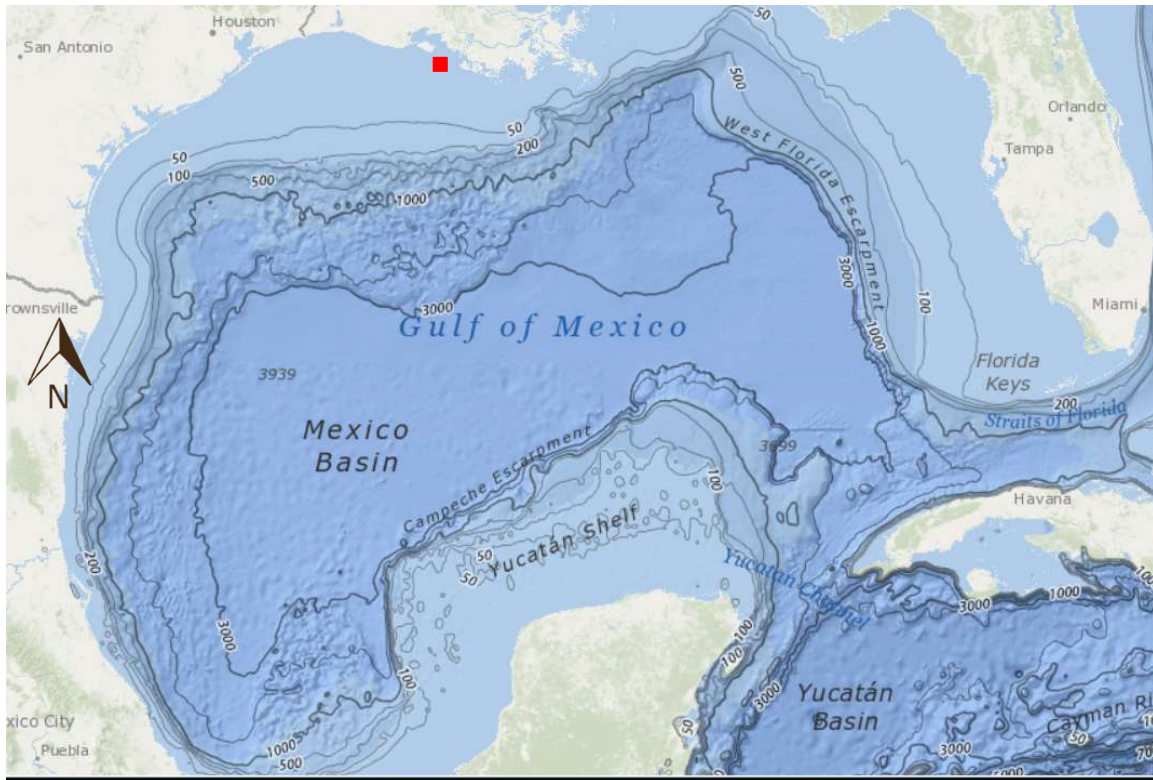
Figure 1.3 displays typical geologic cross sections running N-S on both sides of EI 26. Although the cross sections are approximately 125 miles apart and they straddle EI 26 survey, they still represent a baseline for the regional geology. The Gulf of Mexico region south of Louisiana can be split into three components: the Louisiana Inner Shelf, Louisiana Outer Shelf, and Deep Water (Figure 1.4). The Louisiana Inner Shelf is an area which reaches approximately 50 miles off the southern coast of Louisiana. The EI 26 survey area can be classified as part of the Inner Shelf region. The onset of abnormal pore pressure (overpressure or geopressure) is much shallower in the Outer Shelf than in the Inner Shelf and Deep Water areas as shown in Figure 1.4.

It can also be seen in Figure 1.4 (a) that the western edge of the Inner Shelf is marked by the border between Louisiana and Texas. The Inner Shelf is fed by the Mississippi River, and the shallower sands to the west are deposited by the various river systems of Texas. It can therefore be concluded that the Inner Shelf of Louisiana consists of deltaic sands, while the Outer Shelf consists of older turbidites. Likewise, the sand deposits offshore Texas are controlled by longshore currents that lead to barrier sand bars.

The geological history which led to this modern pressure distribution is likely due to two main factors: (1) Although the Inner Shelf has a higher sand percentage overall (Hilterman 2001), low sediment accumulation rates (SAR) during the late Miocene to early Pliocene across the Inner Shelf led to a period of very high SAR in Outer Shelf. This period of swift sediment deposition contributed to higher compaction disequilibrium. (2) The Inner Shelf is closest to the shore, so more of the sediments here will be coarser grained and have higher permeabilities, which will allow overpressures to reach equilibrium more easily compared to the Outer Shelf. (Morris et al. 2015). The mechanism and significance behind the overpressure trend are discussed further in Section 1.6.4.

The South Marsh Island and Eugene Island geology evaluated in this study is comprised of four-way closures and fault traps with deltaic sands at depths from 1,800-4,300 meters (5,900-14,100 feet). Geologic epochs of hydrocarbon-bearing layers generally range from middle to late Miocene. Salt domes are not present although salt sills and pillow-like features have been observed in the area. The hydrocarbon fields have been heavily developed, and most reservoirs are significantly if not completely depleted. Fluid pore pressures are generally hydrostatic down to about 3000 meters (9840 feet). Most faults in the region can be traced to the water bottom,

indicating the region is recently active. The area is predominantly a gas-bearing region with gas production volume on the scale of a thousand times that of oil (Losh and Cathles 2009).



Position: -91.726° , 29.275°
Elevation: -6 meters

Figure 1.2 Bathymetry map of the GOM with EI 26 survey labeled by red rectangle. The southeast area of the 3D survey is in 6-m water depth. (ngdc.noaa.gov)

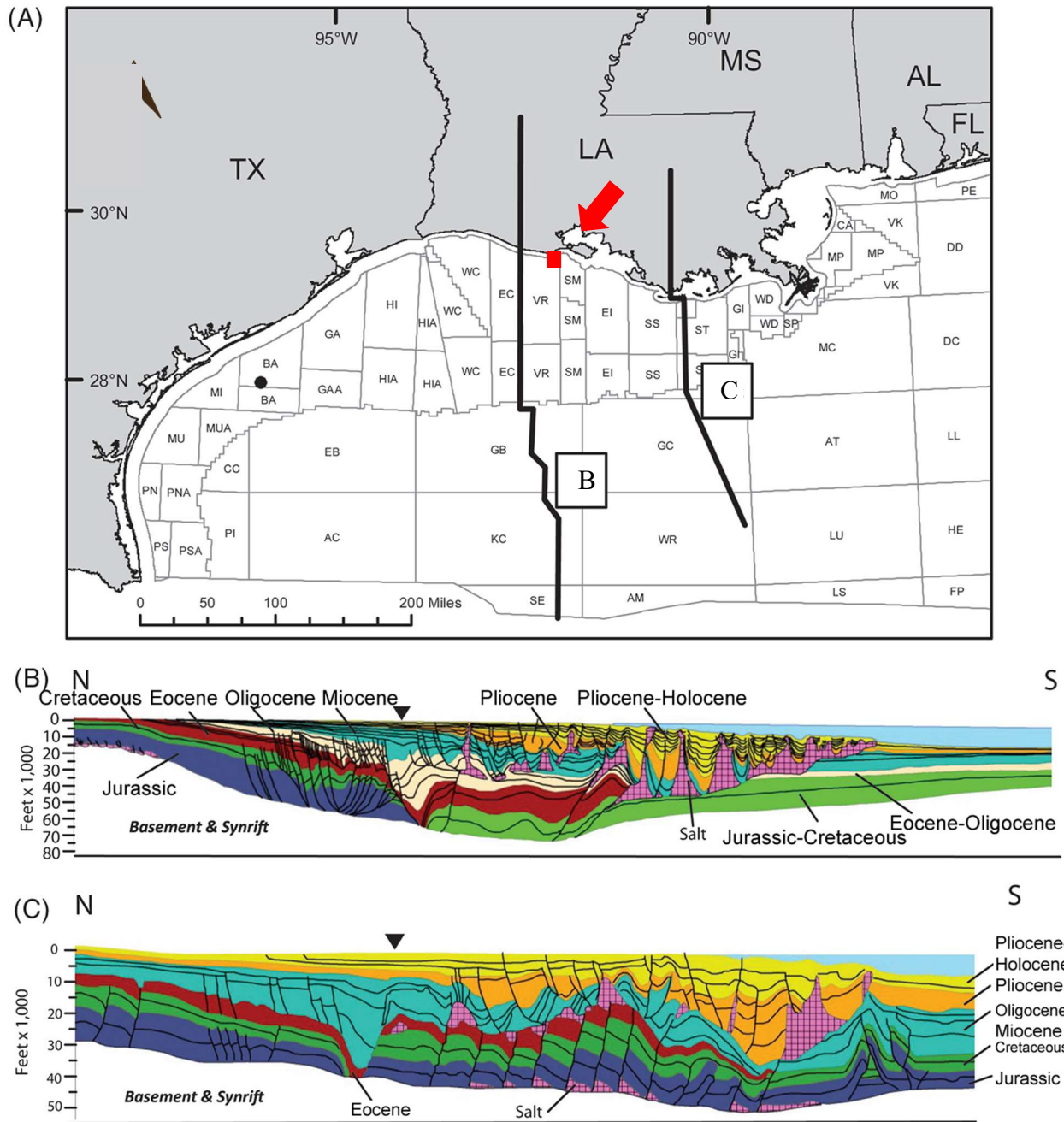


Figure 1.3 (A) Regional map with orientation of cross sections (B) and (C) outlined in black. The black inverted triangles at the top of cross sections (B) and (C) indicate the coast boundary. EI 26 area indicated by red rectangle. (Morris et al. 2015)

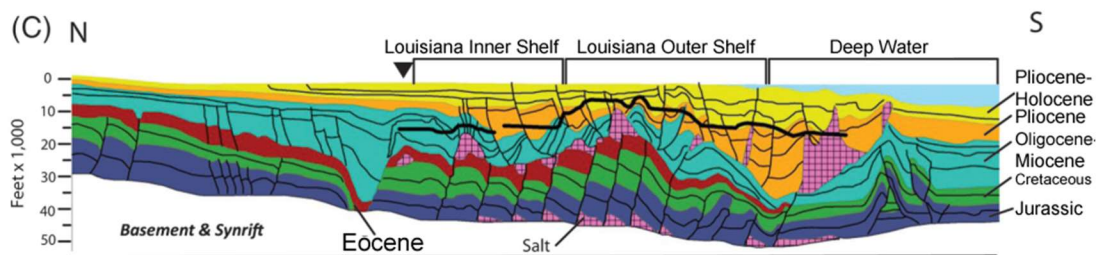
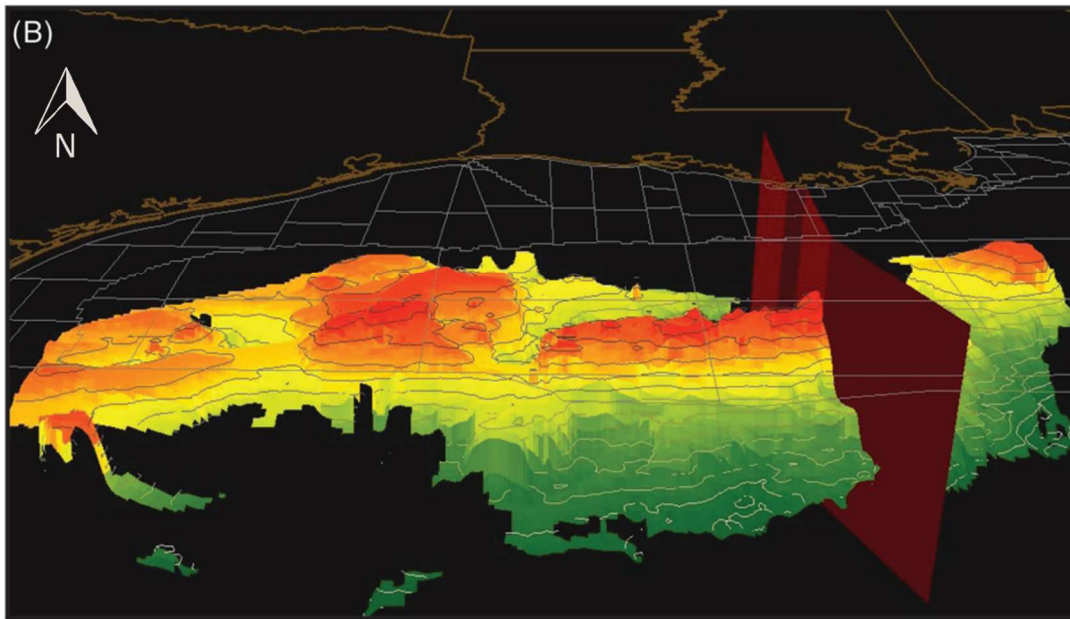
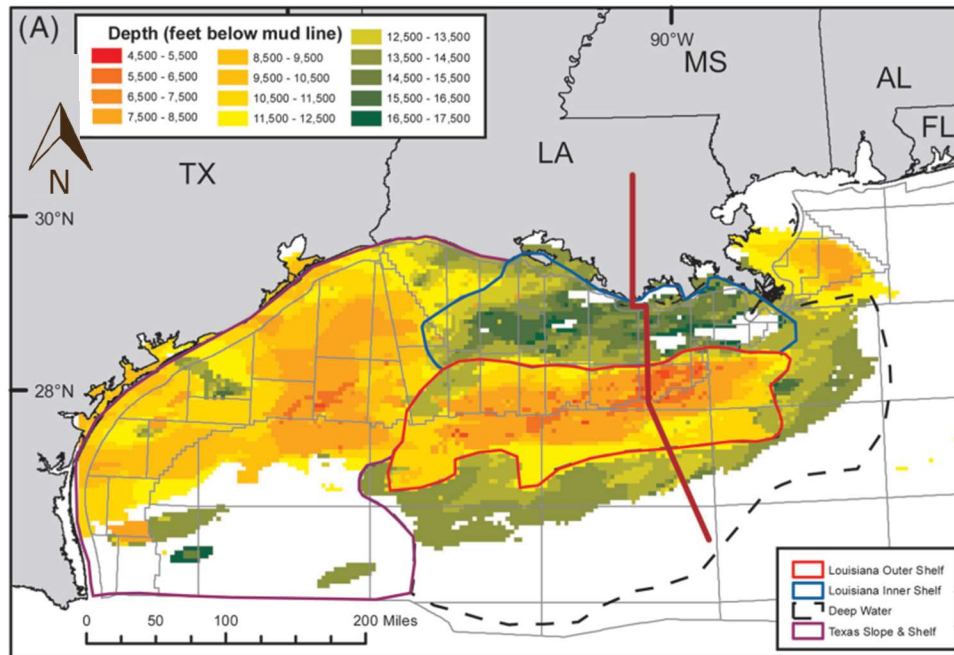


Figure 1.4 (A) Depth map to onset of abnormal pore pressure for the Gulf of Mexico (B) 3D map of constant pore pressure gradient (0.70 psi/ft) in the Gulf of Mexico, and (C) Cross section for red line shown in (A).

1.4 WELL-LOG ANALYSIS

1.4.1 HYDROCARBON INDICATORS FROM WELL LOGS

Since the area within the EI 26 survey vicinity is generally known to contain much higher concentrations of gas versus oil from its geologic background, there are certain hydrocarbon well log indicators that will be focused on. In addition, due to the proximity of the survey area to the shore, it is anticipated that the surface sediments are unconsolidated. This will also pose a challenge for the seismic data-processing phase. With these considerations, the following is a list of typical well-log responses for a desirable gas-saturated sand layer.

1. P-wave velocity decrease. Unconsolidated sands are more sensitive to gas saturation than consolidated sands and subsequently have a greater percentage velocity drop going from brine to gas saturation.
2. Low gamma. Indicates low shale/clay content; that is, more sand.
3. Neutron-density porosity crossover. Indicates gas saturation.
4. High resistivity. Indicates organic matter/hydrocarbons.
5. Negative spontaneous potential. Indicates permeability.

Note that a single positive response from a well log is not a solid indicator of hydrocarbons. In order to confidently interpret a depth layer as hydrocarbon-bearing, it is necessary to have multiple well log curves indicate as such.

1.4.2 WATER SATURATION AND POROSITY ESTIMATIONS

Water saturation, S_w , is defined as the ratio between the volume of water and the total available pore volume for water to occupy,

$$S_w = \frac{\text{Volume of water}}{\text{Total pore volume}} \quad (1.1)$$

Quantifying water saturation in a porous medium from well-log data is commonly achieved via a variant of Archie's (1942) equation:

$$S_w^n = \frac{aR_w}{\varphi^m R_t} \quad (1.2)$$

where S_w = water saturation, n = saturation exponent, R_w = formation water resistivity, φ = porosity, m = cementation exponent, and R_t = true formation resistivity. If there is a water layer below the hydrocarbons in the same reservoir, then a variant of S_w involves the Formation Factor, defined as

$$\frac{R_o}{R_w} = \frac{a}{\varphi^m} \quad (1.3)$$

where R_o = expected brine-saturated formation resistivity, R_w = formation water resistivity, a = constant, and φ = porosity, and m = cementation exponent.

A low water saturation estimate derived from the resistivity log is often indicative of either low porosity or a larger percentage of hydrocarbon fluids. Such an indicator paired with other well-log curves is useful for identifying the percentage of each pore fluid.

For exploration purposes, our main interest is in hydrocarbon saturation, S_{HYD} , which is defined as the remainder between 100% saturation and water saturation,

$$S_{HYD} = (1 - S_w) \quad (1.4)$$

By calculating water saturation and simply subtracting it from one, it becomes possible to estimate the total volume of hydrocarbons for extraction which is important for economics and risk analysis.

But without lab core measurements or other borehole measurements in the hydrocarbon interval, commonly assumed values will be used for the constants where $n = 2$, $m = 2$, and $a = 1$ for carbonates and 0.9 for sandstone. The formation water resistivity, R_w , is calculated in adjacent sand zones where $S_w = 1$. R_w are in the range of $R_w = 0.04 - 0.07$. Inserting Equation 2.3 into Equation 2.2 and assuming $n = 2$ yields

$$S_w = (R_o / R_t)^{1/2} \quad (1.5)$$

When the formation is totally water saturated, the porosity is estimated with the density log as

$$\phi = \frac{\rho_{LOG} - \rho_{GR}}{\rho_{FL} - \rho_{GR}} \quad (1.6)$$

where ρ_{LOG} = density-log value, ρ_{GR} = grain density and ρ_{FL} = fluid density.

When the reservoir is gas saturated, the porosity ϕ can be estimated using the neutron porosity and density porosity curves:

$$\phi = \sqrt{\frac{(\phi_{neutron})^2 + (\phi_{density})^2}{2}} \quad (1.7)$$

where $\phi_{neutron}$ = neutron porosity, $\phi_{density}$ = density porosity, and ϕ = estimated porosity.

1.4.3 WELL LOCATIONS

Overall, there are 15 wells with sufficient logs available within the EI 26 survey, as depicted in Figure 1.5. Although some wells are missing header information, it is estimated the wells were drilled from the 1980's to 1990's. Of those 15 wells, only 10 have high quality logs which are useful for reservoir characterization. In order to obtain good results from the well-to-seismic tie, it is best to choose a well close to the center of the survey where seismic coverage is the highest. Well 3149 is located in a prime location with high seismic fold, but unfortunately 3149 is missing sonic log information at key depth intervals. This is compensated for by estimating the sonic log based on resistivity information to create a pseudo-sonic log. Well 6976 is also used for well tie studies despite the location being less desirable due to its proximity to the edge of the 3D survey.

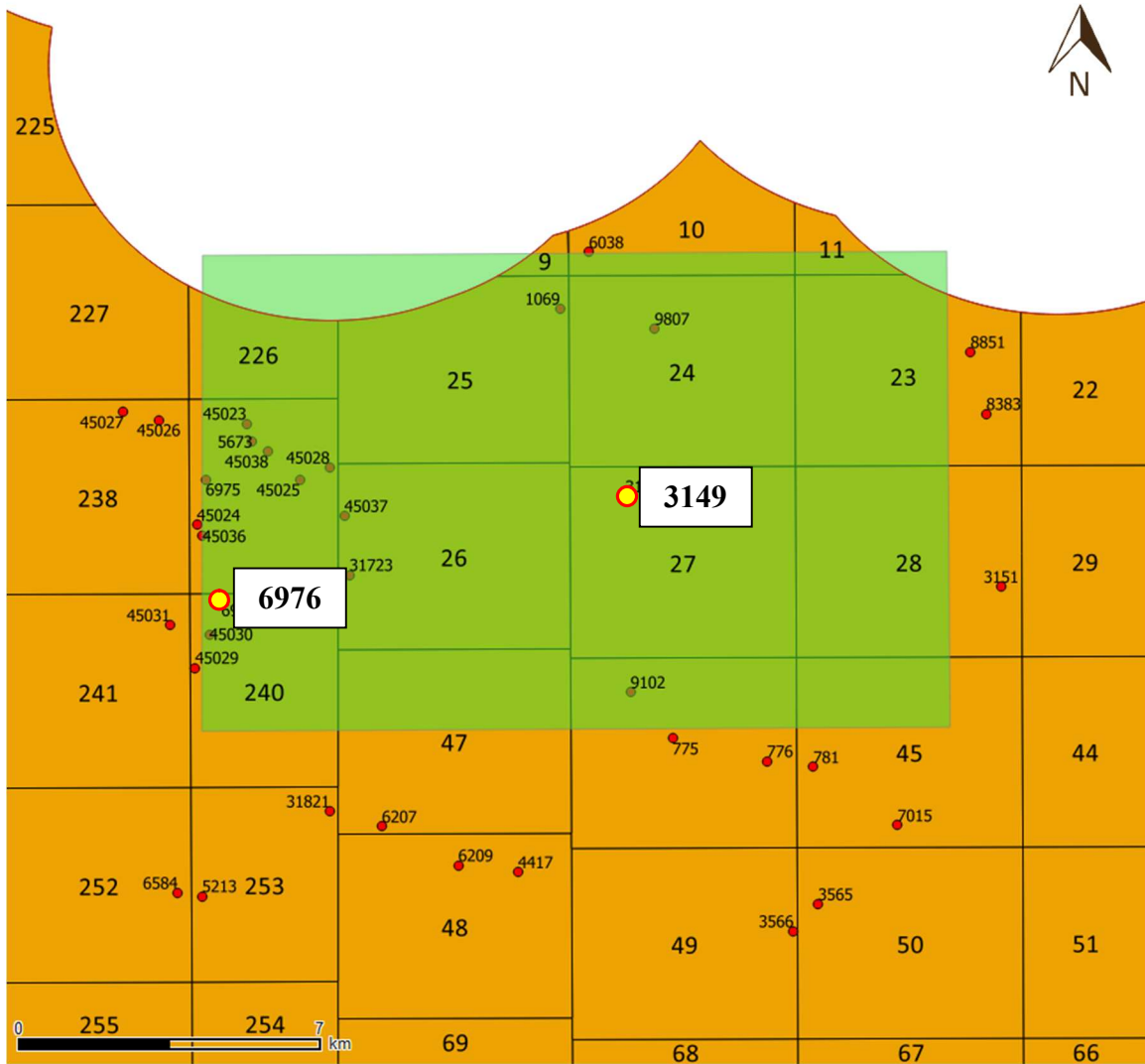


Figure 1.5 EI 26 (green) survey area with available well-log locations (red dots). The well numbers are unique identifiers assigned by Geokinetics.

1.4.4 WELL LOG CURVES AND CROSSPLOTS

From the geology background, it is known that the hydrocarbons in the area are predominantly gas. Water saturation values are a good indicator of potential hydrocarbons in a porous sandstone. Therefore, we would look for low gamma, high sand volume, high resistivity, low spontaneous potential, neutron-density crossover, and low water saturation. Figure 1.6 shows a well-log suite for Well 3149 and based on previously stated desirable properties, no gas-saturated intervals were found. The water-saturation curve was estimated with Equation 2.4 with an assumed R_w that was too large. This resulted in S_w values that need to be shifted towards $S_w = 1$. However, in Figure 1.7, for Well 6976, several potential hydrocarbon zones were identified. Again, the S_w curve needs to be shifted towards $S_w = 1$ so that the shale base line is $S_w = 1$.

The upper-right panels of Figure 1.8, Figure 1.9, and Figure 1.10 display different seismic attributes curves (AI, SI, bulk density, Poisson's ratio, and bulk modulus) and are used to address the sensitivity and calibration between the well log curves and seismic data. In the upper left of Figure 1.8, the well-log curves are displayed in depth at a sample interval of 1 ft. In the upper right, the well-log curves are displayed at a sample rate of 1 ms, which means approximately four 1-ft depth samples were averaged to get one 1-ms time sample. There is a loss of resolution for lithology and pore-fluid discrimination going from the depth samples at 1-ft sampling to the time samples at 1-ms sampling. The four crossplots at the bottom of the figure contain 1-ft depth samples and thus exhibit higher resolution when compared to crossplots displayed at time samples of 1 ms (Figure 1.9). Based on the separation of the gas saturated clusters from the sand and shale clusters, pore fluid discrimination is possible from the data. But due to the close proximity of the sand and shale clusters, lithology discrimination will be difficult.

Figure 1.9 and Figure 1.10 are designed to illustrate the rock-property resolution obtainable during seismic resolution. They depict seismic inversion estimates of rock-property attributes in the upper right time displays and lower crossplots. After depth-to-time conversion, the time curves in the upper right of Figure 1.9 were filtered with a 0-0-6-7 Hz Ormsby filter to simulate a low-frequency trend being added during a regular inversion process. This low-frequency trend is typically derived from seismic velocity analysis or a spatial interpolation of low-frequency trends from numerous well-log locations. Then in a 6-7-249-250 Hz filter was applied to the original time curve and added to the low-frequency filtered curve. In Figure 1.9, the action of the two filters is basically a “do nothing”. However, in Figure 1.10, a more realistic seismic passband of 6-7-30-40 Hz is applied for the high-frequency trend. Figure 1.10 is a zero phase representation of the bandwidth that seismic data have. Figure 1.11 uses the same passband but with a 70-degree phase shifted representation of the bandwidth seismic data may have.

The reason for applying two filters is that seismic data are often not zero-phase before inversion is done. However, the low-frequency trend is typically zero phase and if the high-frequency seismic is not zero-phase, the addition of the low and high trends will lower the resolution as the duration of the seismic wavelet increases (Papoulis, 1962) with jumps in the phase spectrum. This drop in resolution between zero phase and a 70-degree phase shifted wavelet can be observed in the crossplots in Figure 1.10 and Figure 1.11, respectively.

The crossplots from Figure 1.8, Figure 1.9, Figure 1.10 and Figure 1.11 were combined together in Figure 1.12. The upper row in Figure 1.12 illustrates that higher resolution for distinguishing lithology and pore-fluid that exists in well-log crossplots sampled at 1 feet versus the same data when examined at typical seismic resolution (bottom row). The well log

crossplots have the highest resolution, while the seismic inversion crossplots have a significant decrease in resolution due to a narrower frequency band. Additionally, a phase shifted wavelet further distorts the crossplots results.

A narrower depth interval between 7,370 and 7,670 feet focused on the hydrocarbon zones of interest. Crossplots for each vertical column (Figure 1.12) correlate with each other but the resolution decreases from top to bottom. The consequence of this crossplot comparison implies that inversion of the data at a seismic resolution will produce subpar results, and higher frequency data is needed for accurate inversion results.

The two CDP gathers in the upper-right corner of Figure 1.13 labeled in-situ synthetic and fluid sub synthetic represent the fluid substitution panel. In this example, the fluid substitution synthetic replaces the defined hydrocarbon intervals from the in-situ synthetic with brine, which produces a different reflection amplitude variation with offset. On a CDP gather, a Class III AVO response is exhibited with a large negative reflectivity from near-to-far offsets when compared to the brine-saturated synthetic. The Class III magnitude of the reflection normally becomes slightly larger with offset. The gas AVO signatures in Figure 1.13 are Class III anomalies. Additional information on AVO classification is shown in Figure 1.14, Figure 1.15, Figure 1.16 in Section 1.5.2. Based on the results of the fluid substitution, it should therefore be possible to discriminate between a gas-saturated sand layer and a brine-saturated sand layer at the depth of interest in this study.

Figure 1.13 also displays a crossplot comparison between calculated reflectivities from (B vs. NIP), (Poisson's reflectivity vs. NIP), and (NIS vs. NIP), where B = CDP reflectivity gradient, NIP = Normal Incident P-wave Reflectivity, Poisson's reflectivity = $\Delta\sigma/[1-(\sigma_2-\sigma_1)/2]^2$

where σ is Poisson's ratio and subscripts 1 and 2 refer to upper and lower layers, respectively, and NIS = Normal incident S-wave reflectivity.

Based on the reflectivity contrast between hydrocarbon saturated and brine-saturated sands, all three crossplots provide evidence of a Class III environment. All three crossplots have sufficient resolution for pore-fluid discrimination.

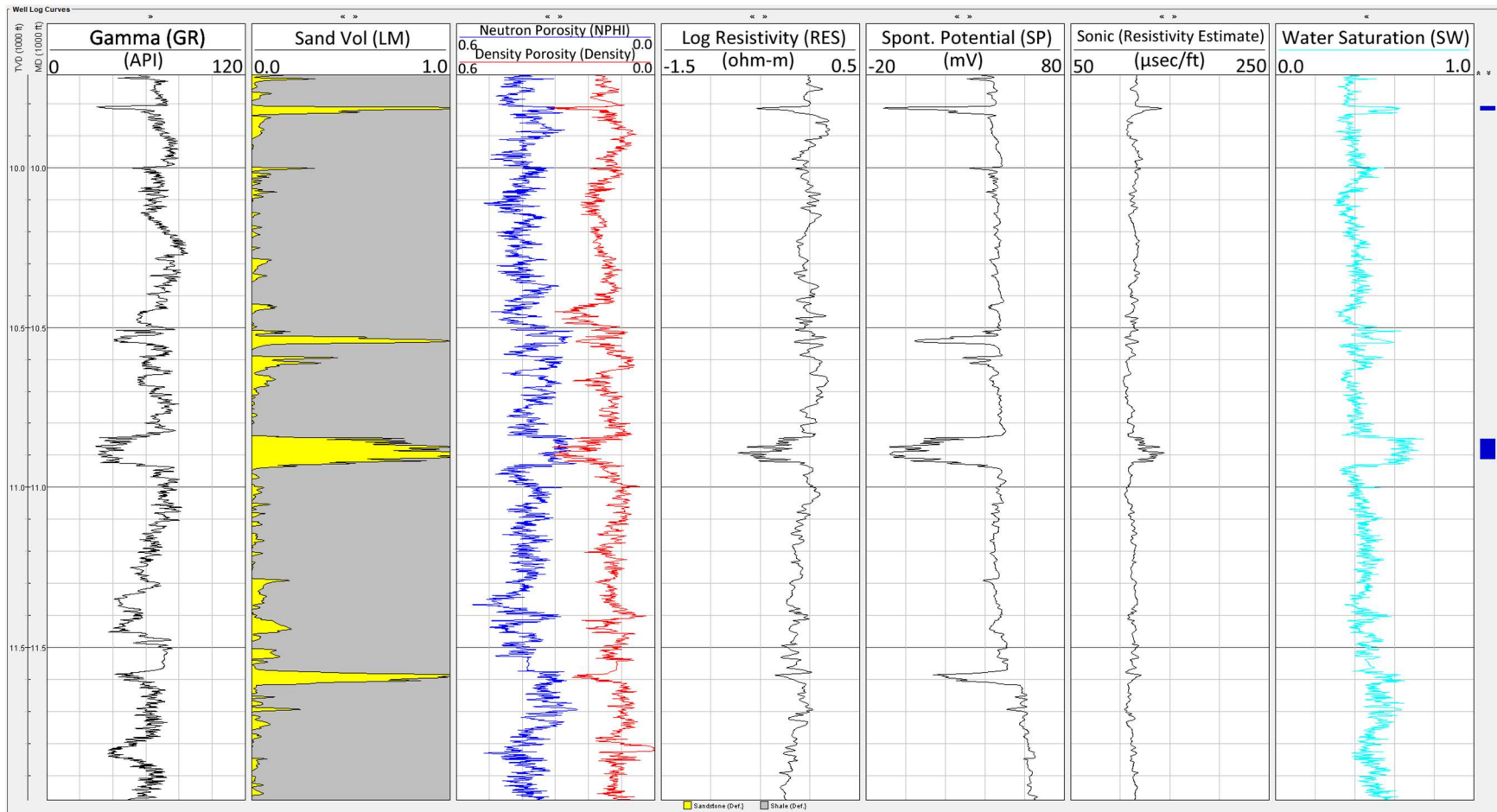


Figure 1.6 Well-log curves from Well 3149, from left to right: Gamma, Sand Volume, Neutron + Density Porosity, Resistivity, Spontaneous Potential, Sonic Estimate, and Water Saturation. Blue blocks on the right side indicate porous sand intervals.

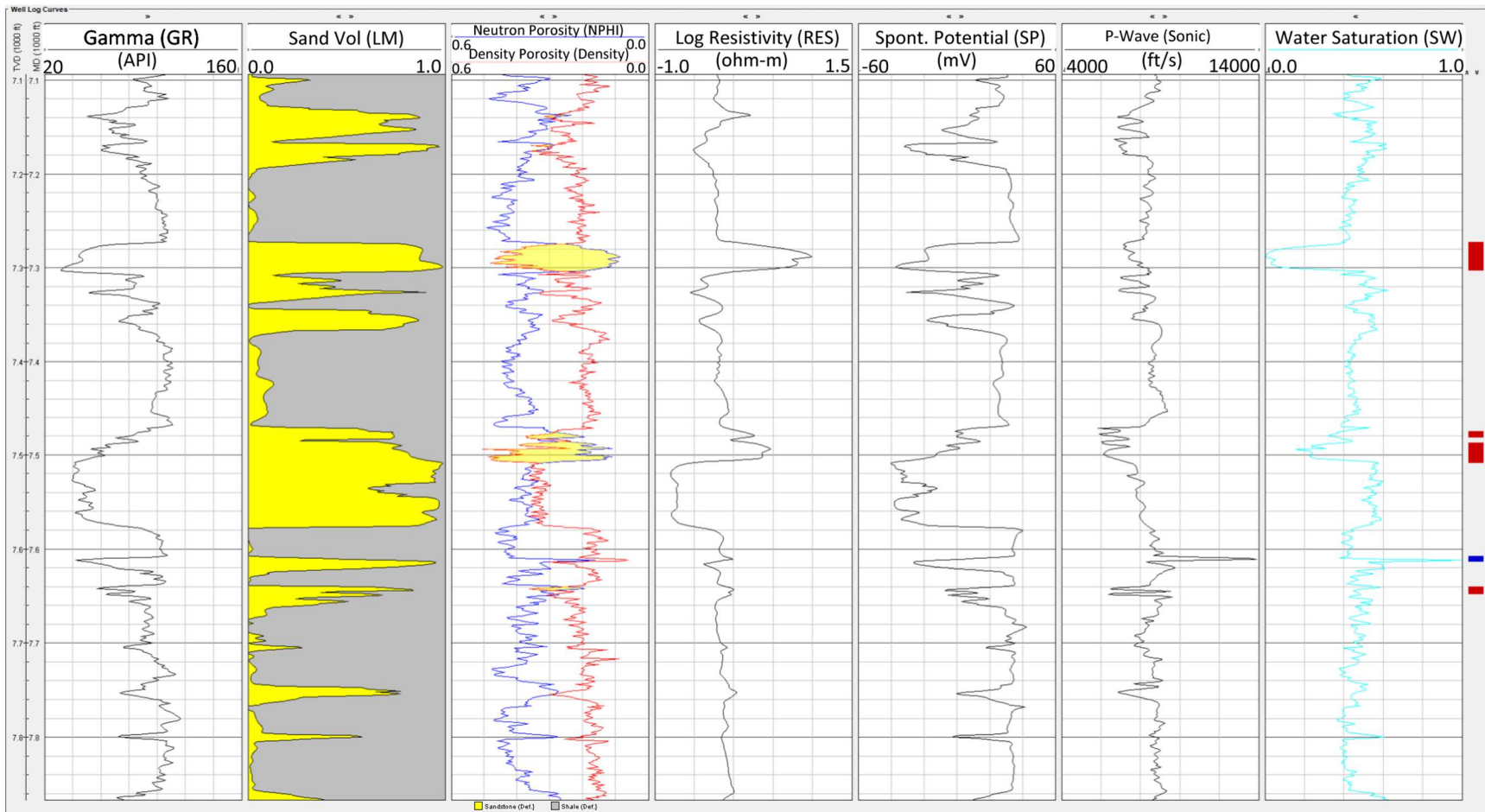


Figure 1.7 Well log curves from Well 6976, from left to right: Gamma, Sand Volume, Resistivity, Neutron + Density Porosity, Spontaneous Potential, P-wave velocity, and Water Saturation. Blocks on the right side indicate sands with different pore fluids (red = gas, blue = water).

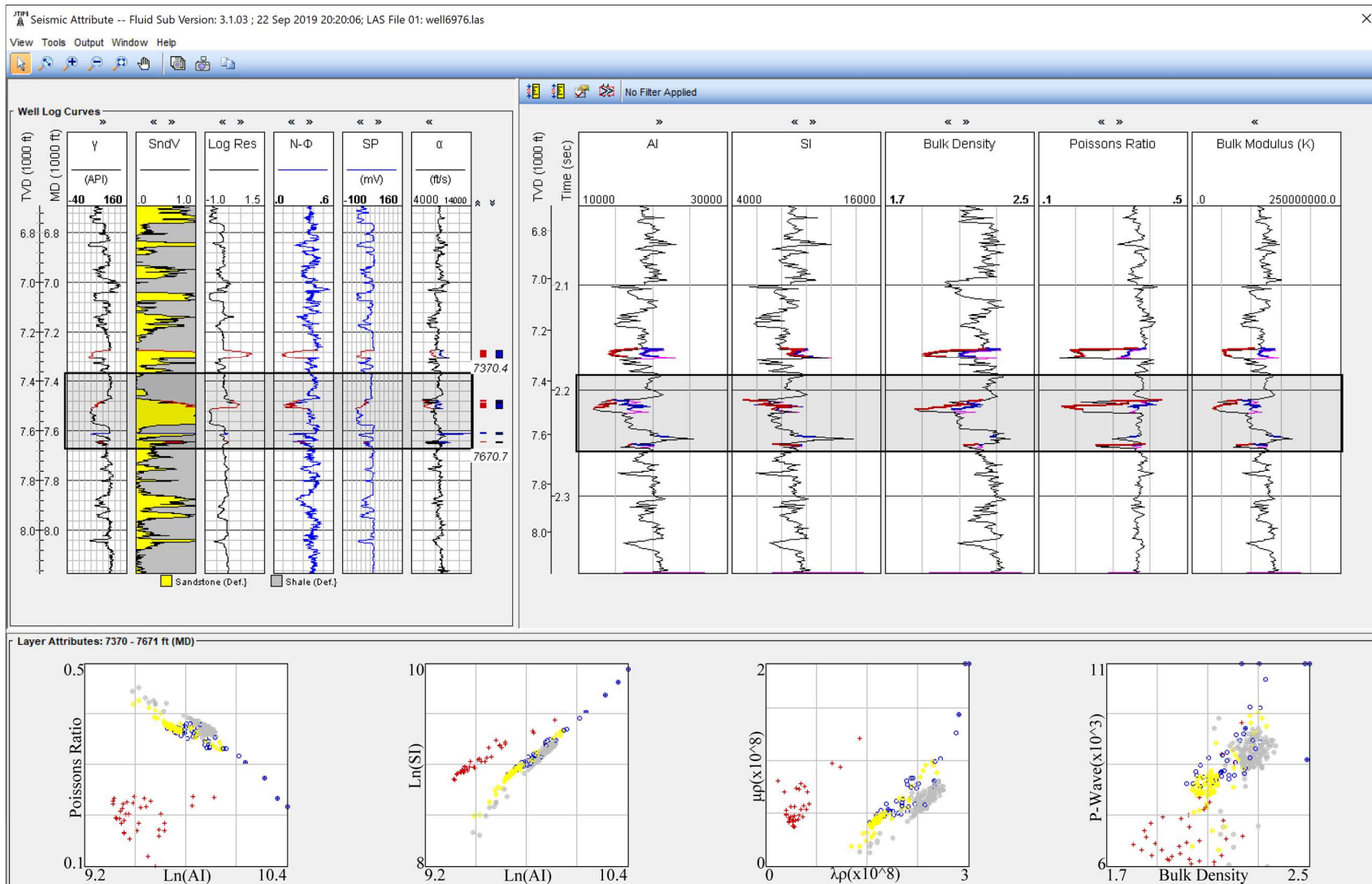


Figure 1.8 Fluid substitution and crossplots derived from Well 6976. For the seismic attribute curves, red indicates gas sands, and blue indicates brine sands. In the lithology crossplots along the bottom, red (+) signs are hydrocarbons, yellow (+) signs are sands, grey (+) signs are shale, and blue (+) signs are brine.

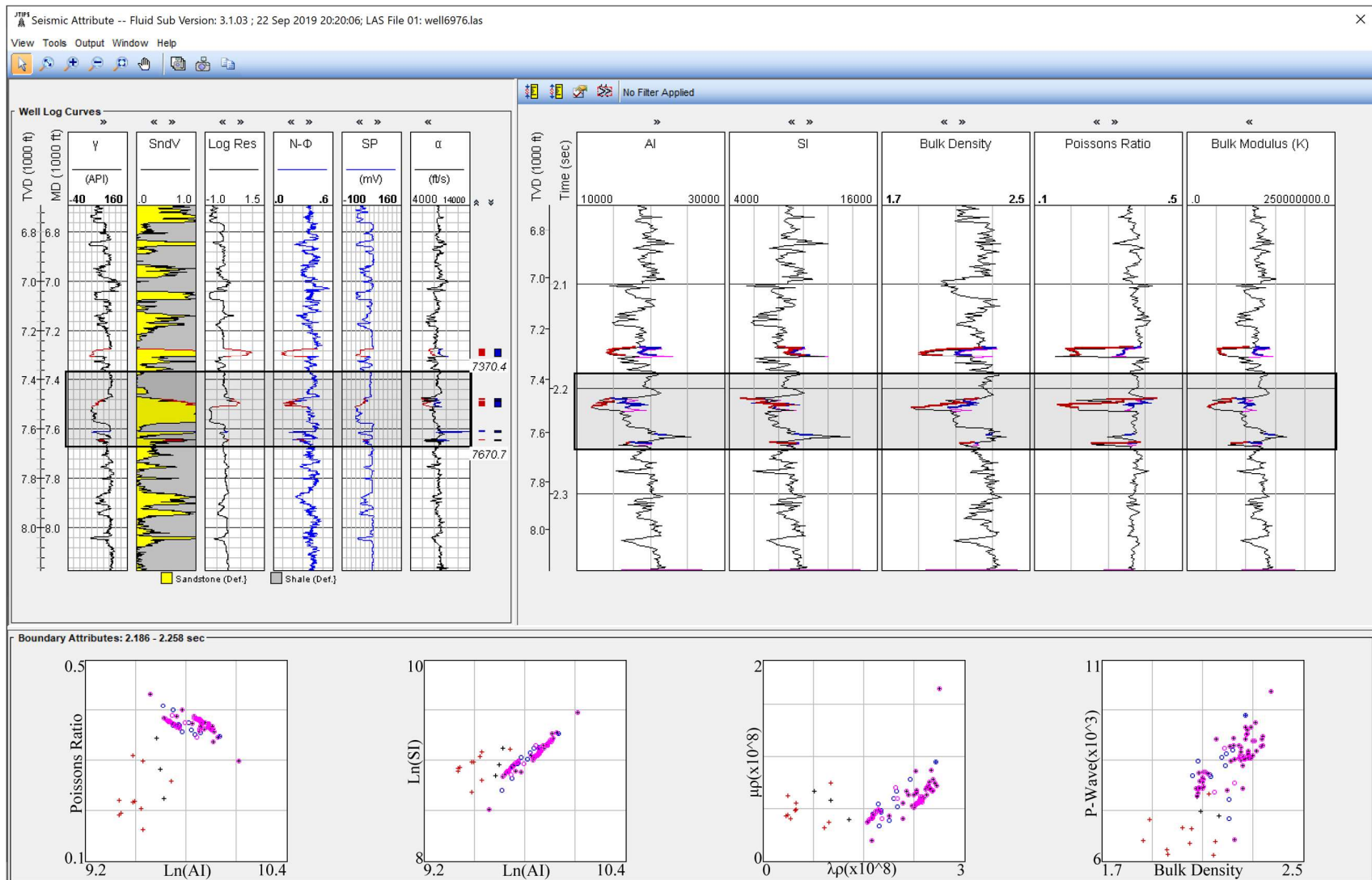


Figure 1.9 Seismic attribute crossplots derived from Well 6976. For the seismic attribute curves, red indicates gas sands, and blue indicates brine sands. For the seismic attribute crossplots, red (+) signs are gas sands, magenta (o) signs are shale, and blue (o) signs are brine sands

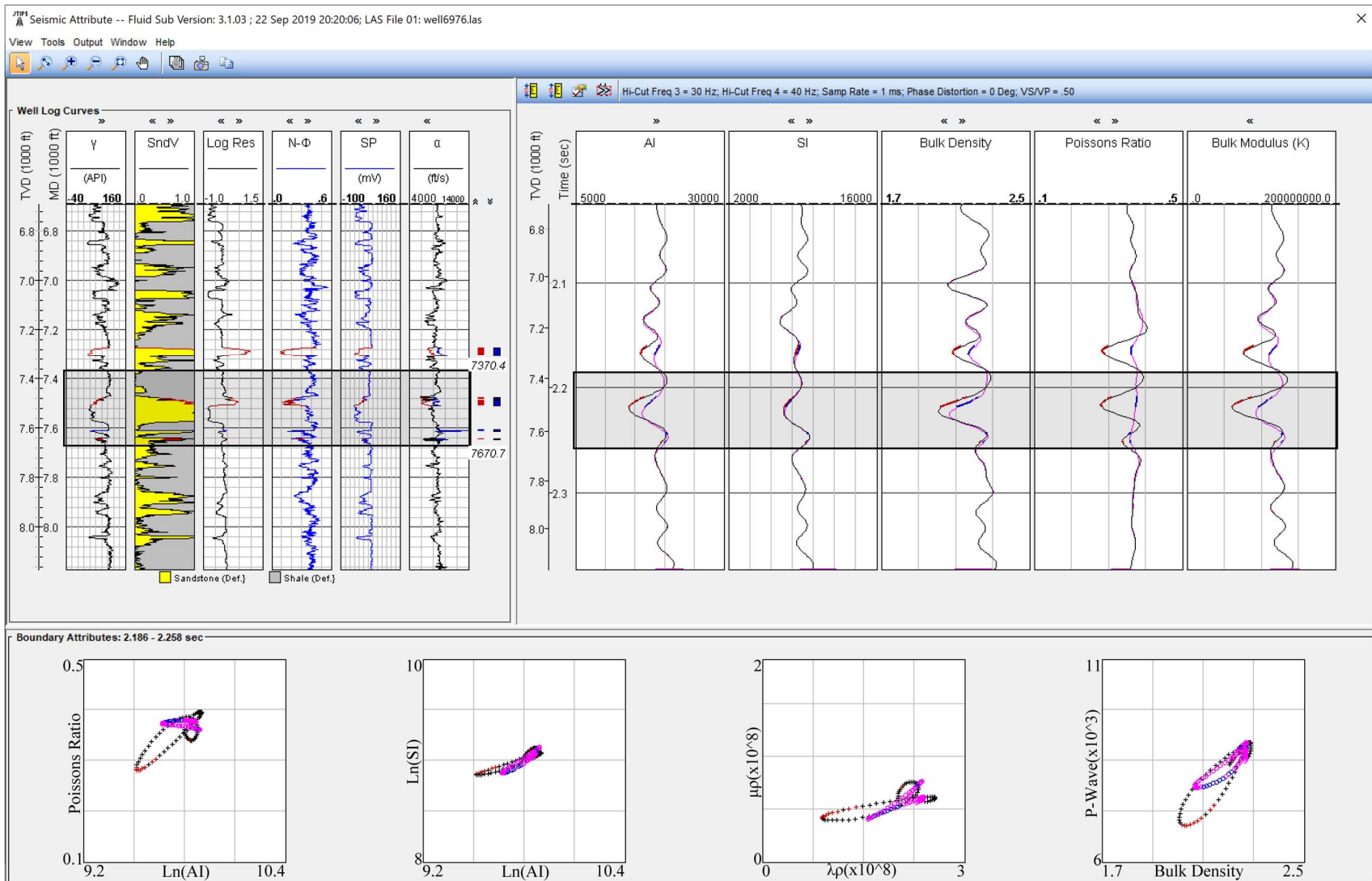


Figure 1.10 Seismic bandwidth filtered attributes derived from Well 6976. For the seismic attribute curves, red indicates gas sands, and blue indicates brine sands. For the seismic attribute crossplots, red (+) signs are gas sands, magenta (o) signs are shale, and blue (o) signs are brine sands

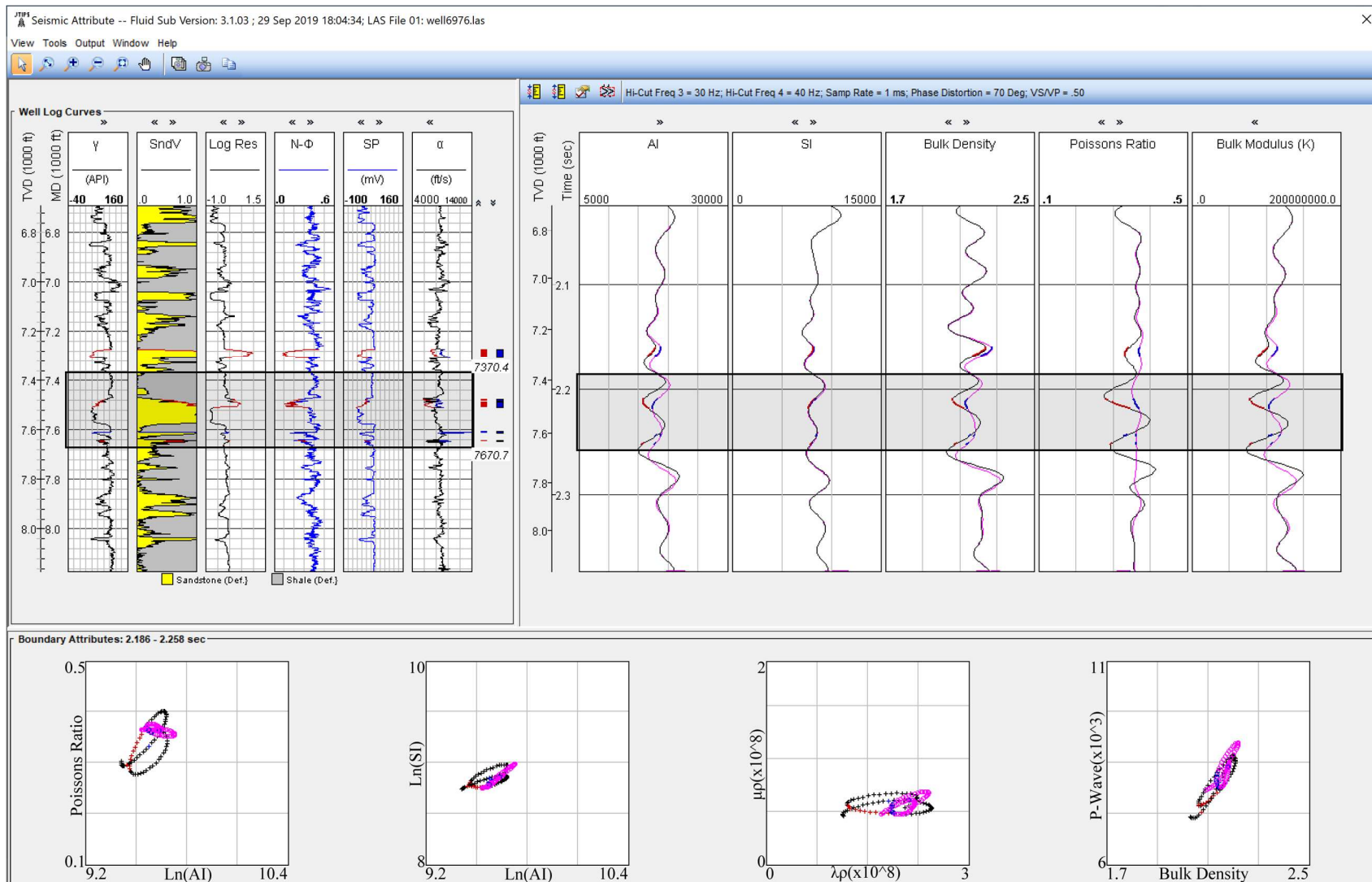


Figure 1.11 Seismic bandwidth filtered attributes derived from Well 6976, with a phase distortion of 70 degrees. For the seismic attribute curves, red indicates gas sands, and blue indicates brine sands. For the seismic attribute crossplots, red (+) signs are gas sands, magenta (o) signs are shale, and blue (o) signs are brine sands

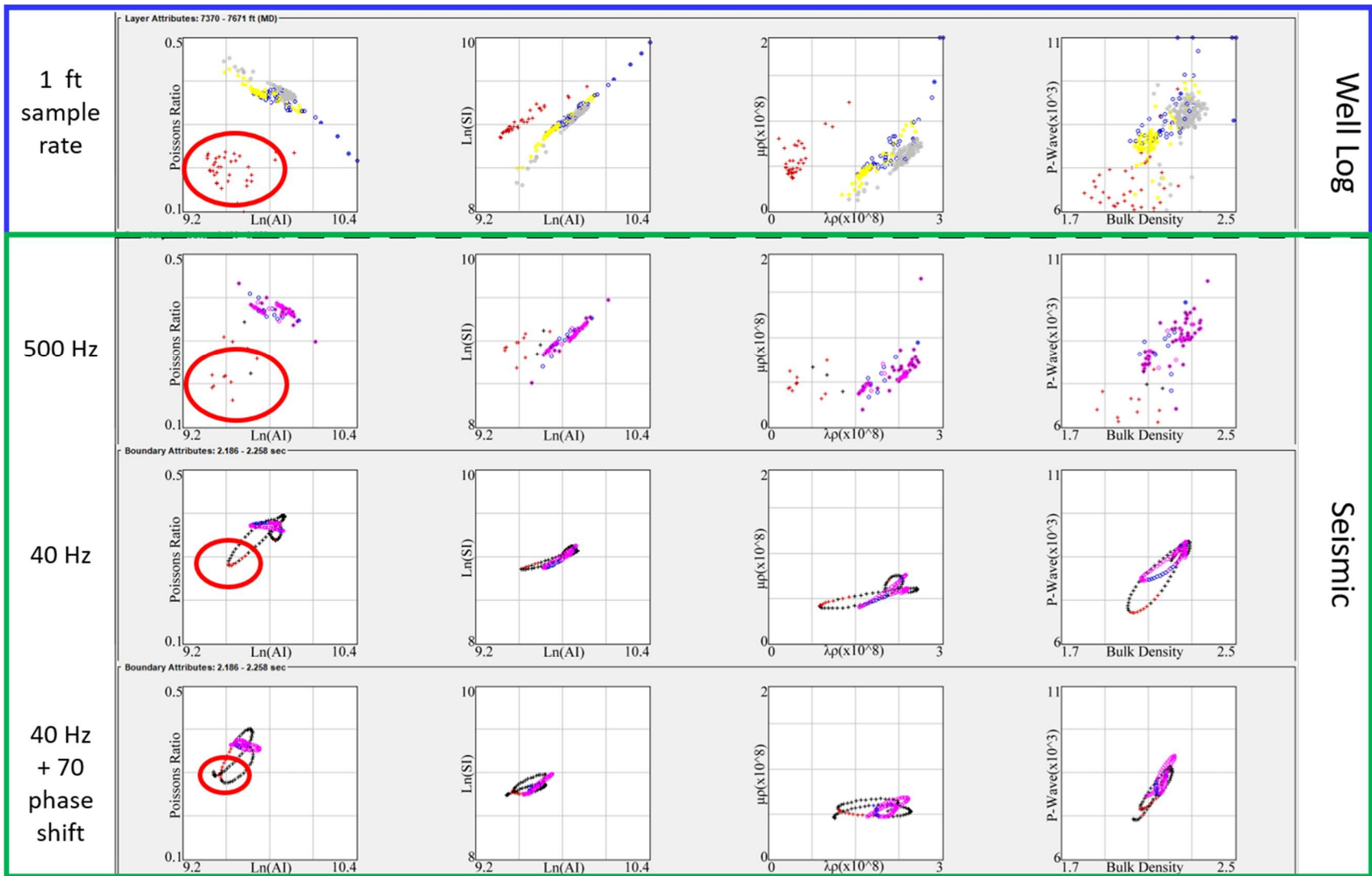


Figure 1.12 Crossplot comparison from Figure 1.8, Figure 1.9, Figure 1.10, and Figure 1.11 (from top-down respectively) with the same focus window. The crossplots of the filtered seismic (second to bottom row) are tangled together and difficult to discriminate pore fluid or lithology in comparison to the crossplots at well log resolution (top row). The gas clusters are indicated by the red circles.



Figure 1.13 Reflectivity NIP crossplots indicating the presence of Class III reflections based on the positions of hydrocarbons vs. sands, red (+) signs are gas sands, magenta (o) signs are shale, and blue (o) signs are brine sands. Red ovals outline Class III reflection zones.

1.5 AVO ANALYSIS

1.5.1 INTRODUCTION

AVO is short for Amplitude Variation with Offset but this terminology is misleading as most applications of AVO are actually AVA, or Amplitude Variation with Angle. Ideally, AVO provides insight to the elastic properties of a formation's P-wave velocity (V_p), S-wave velocity (V_s), and density, which are arranged in different seismic attributes to predict the petrophysical products of lithology, porosity and pore-fluid type and quantity.

AVO analysis is derived from the Zoeppritz equation, which defines the division of seismic amplitude at a boundary. Unfortunately, the full Zoeppritz equation is too complex for practical applications, such as inversion; so numerous linear approximations have been developed as alternatives, such as the Aki-Richards equation

$$RC(\phi) \approx \underbrace{\frac{1}{2} \left(\frac{\Delta\alpha}{\alpha} + \frac{\Delta\rho}{\rho} \right)}_A + \underbrace{\left[\frac{1}{2} \frac{\Delta\alpha}{\alpha} - 2 \left(\frac{\Delta\beta}{\alpha} \right)^2 \left(\frac{2\Delta\beta}{\beta} + \frac{\Delta\rho}{\rho} \right) \right]}_B \sin^2 \theta + \underbrace{\frac{1}{2} \frac{\Delta\alpha}{\alpha}}_C (\sin^2 \theta \tan^2 \theta) \quad (1.8)$$

where RC represents the reflection coefficient, ϕ is the angle of incidence and θ is the average of the incident and transmitted angles. α , β , and ρ represent the P-wave, S-wave and density averages of the upper and lower media, respectively, while Δ values represent the lower minus upper elastic properties. (Aki and Richards 1980; Shuey 1985).

Equation 2.8 is further simplified to,

$$RC(\theta) \approx A + B \sin^2 \theta + C \sin^2 \theta \tan^2 \theta \quad (1.9)$$

where A is called the intercept; B, gradient/slope; C, curvature and, θ is the incident angle.

The C term is used for describing the behavior of far offsets but is often (and will be) ignored for this research. The simplified equation is the basis of what is called the intercept-gradient method, a tool for identifying different AVO class signatures.

There are four main AVO classes that are commonly attributed to different AVO responses. These are called Class I, Class II, Class III, and Class IV (Rutherford and Williams, 1989, and Castagna and Swan, 1997). The characteristics of the four AVO classes are described in Table 2 and their typical reflection curves as a function of incident angle are depicted in Figure 1.14 and Figure 1.15. These curves vary depending on numerous physical properties (Wang, 2001) but the explorationist is mainly interested in the AVO variation related to changes in the petrophysical properties of pore-fluid content, porosity, and lithology. As an example, the AVO signatures for three AVO Classes are shown in Figure 1.15 for variation of pore-fluid content, gas versus brine saturation.

By plotting the gradient (B) vs. intercept (A) (Figure 1.16), the seismic response for the different AVO classes fall into different quadrants compared to the background trend. For brine vs. gas saturated sands, the theoretical gradient vs. intercept responses are shown in Figure 1.17. The separation of the gas A-B points from the brine-saturated points in Figure 1.17 is the basis that provides a method for distinguishing pore-fluid type in field data.

AVO Class	Description
Class I	Dim spot High impedance sands Decrease in magnitude with higher incident angles
Class II	Possible phase reversal of normal incidence Near-zero impedance contrast between shale over sand Increase in magnitude with higher angles
Class III	Bright spot Low impedance sands Increase in magnitude with higher angles
Class IV	Low impedance sands Decrease in magnitude with higher angles

Table 2 Characteristics of the four AVO Classes. (Rutherford and Williams 1989, Hiltermann 2001, Castagna and Swan 1997)

1.5.2 AVO ATTRIBUTES

AVO attributes are derived from the reflection amplitude variables A and B. These attributes are used to highlight and draw attention to expected AVO behavior with respect to variations of petrophysical properties. As shown in Figure 1.17, a gas-saturated sand slope-intercept plot derived from field data will fall to the lower left of the background trend which represents the shale-over-shale AVO signature or shale-over-brine saturated sands.

A popular AVO attribute is the AVO product, $A*B$ (Hiltermann 2001) which is the intercept multiplied by the gradient. This attribute works best on Class III (bright spot) AVO responses because Class III AVO signatures have a large negative intercept and a negative slope, therefore the product produces a strong positive response. Compared to other AVO classes which involve phase reversals and dim spots, the $A*B$ AVO product makes the recognition of Class III anomalies easier but identifying what is causing the anomalies requires further analysis.

Another aspect of AVO methods involves the study of different impedance behavior. The most basic impedance relationships are acoustic impedance (AI) and shear impedance (SI):

$$AI = \rho V_p$$

$$SI = \rho V_s$$

Other impedance methods such as lambda-rho ($\lambda\rho$), mu-rho ($\mu\rho$), and V_p/V_s are derivatives of AI and SI where:

$$\lambda\rho = AI^2 - 2SI^2$$

$$\mu\rho = SI^2$$

$$\frac{V_p}{V_s} = \frac{AI}{SI}$$

Poisson's ratio (σ) can also be related to V_p , V_s through:

$$\sigma = \frac{V_p^2 - 2V_s^2}{2(V_p^2 - V_s^2)}$$

Cross plotting these impedance values, well log curves, and other properties such as Poisson's ratio is used to help discriminate between different types of pore fluid content such as in Figure 1.8, Figure 1.9, and Figure 1.10.

Cross-plotting different rock-property attributes derived from well-log data provides a visual and quantitative assessment of whether pore-fluid type and lithology can be discriminated from the actual seismic data. The position in the crossplot that the various clusters of lithology and pore fluid reside allow the interpreter to color-code a seismic section based on a two-dimensional color table (Verm and Hilterman, 1995) so that the section displays lithologies and/or pore-fluid saturants with different colors.

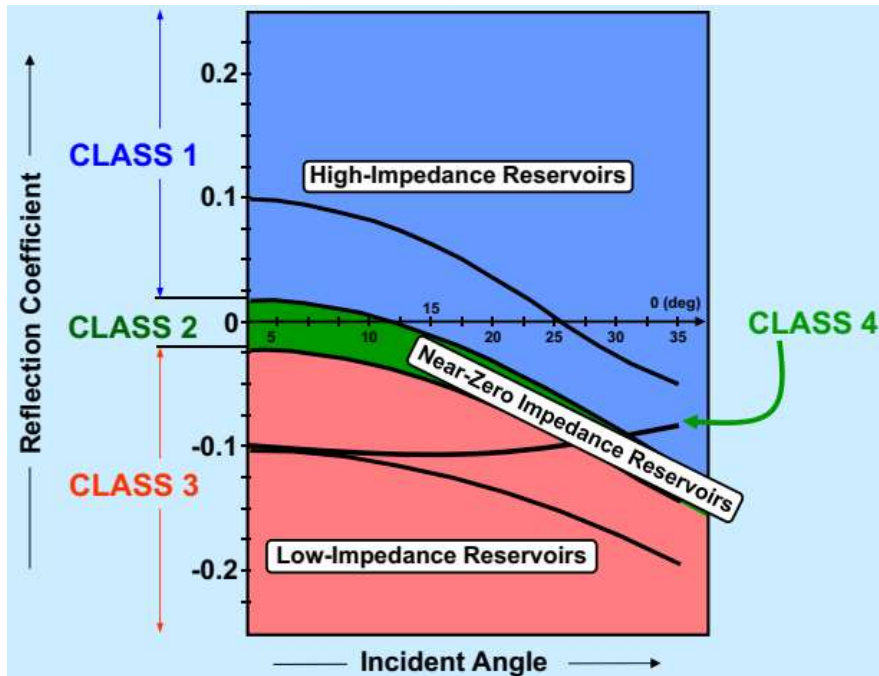


Figure 1.14 Reflection coefficient vs. incident angle for four classes of AVO (Hilterman 2001)

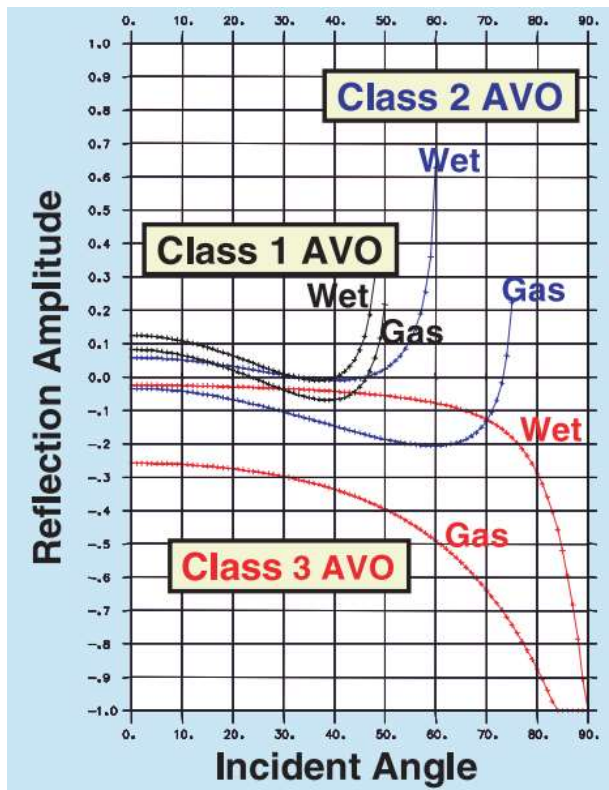


Figure 1.15 AVO class responses to brine vs. gas signatures. (Hilterman 2001)

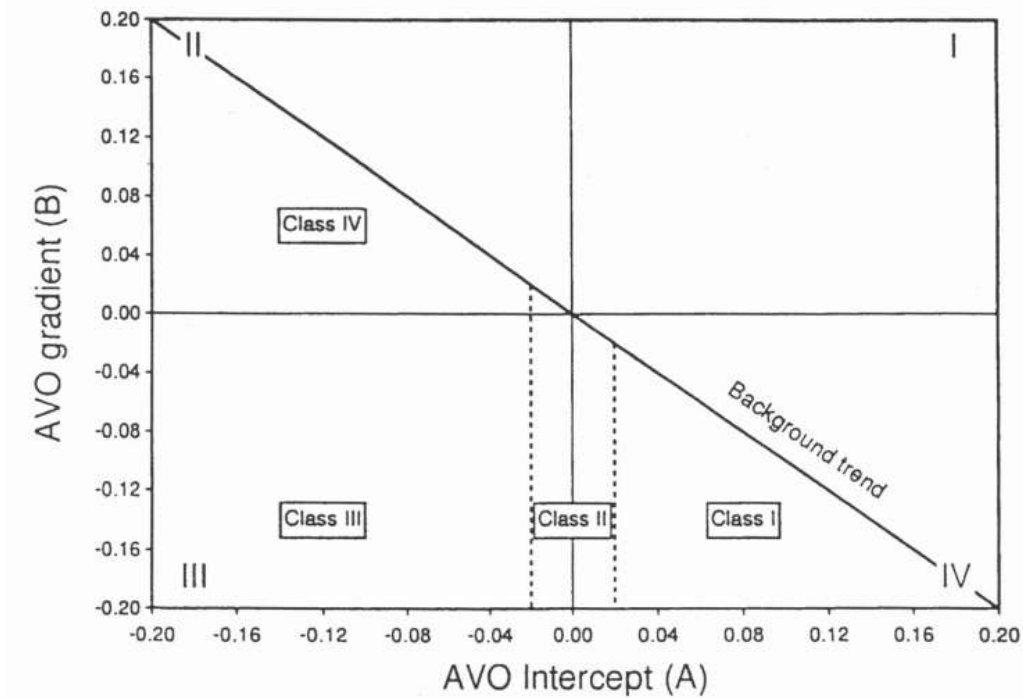


Figure 1.16 AVO classes in terms of the intercept (A) and gradient (B) terms. (Zhang and Brown 2001)

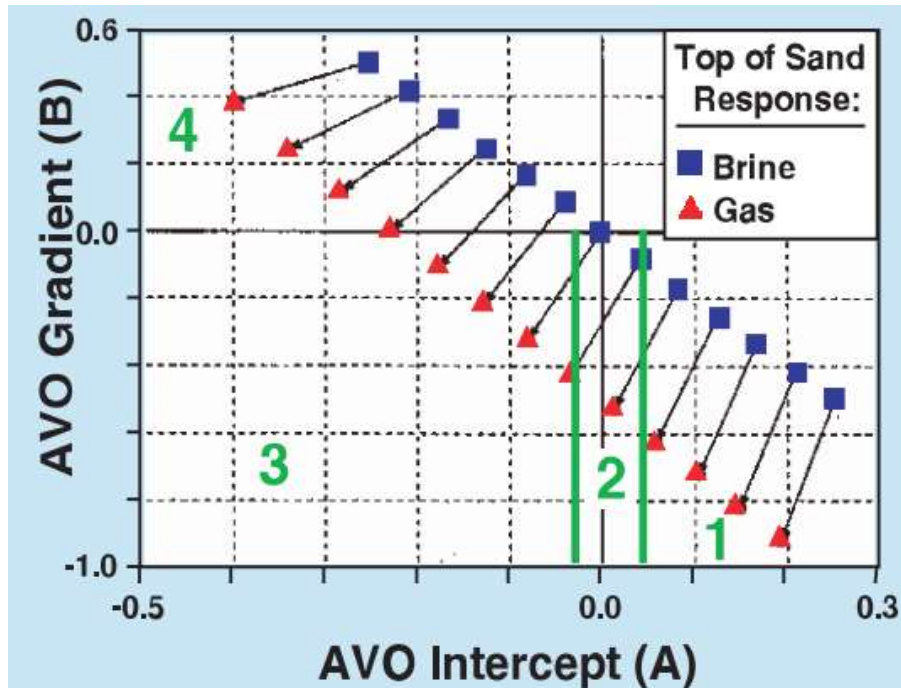


Figure 1.17 Gradient vs. Intercept AVO response for brine and gas-saturated sands (Hilterman 2001, Castagna and Swan, 1997)

1.6 PORE PRESSURE ANALYSIS

1.6.1 INTRODUCTION

Pore pressure analysis is another aspect of exploration which is usually used in areas with young sedimentary content such as the Gulf of Mexico. Traditionally, pore pressure information aids drilling efforts to predict and prevent hazards. One of the most dangerous hazards are blowouts, an uncontrollable eruption of fluids from the well. The inclusion of fluids like hydrocarbons in certain environments may cause anomalously high pore pressures and lead to life-threatening situations. The weight of overlying rock and sediments causes significant pressure buildup in subsurface structures, so proper mud-weight compensation for these different pore pressure regimes at varying depths is of primary concern.

Therefore, one of the primary goals of pore pressure analysis is detecting sudden increases or decreases in pore pressure prior to drilling, which will allow field teams to mitigate risks. Blowouts in particular have the potential to damage not just the drill mechanism and drilling team but also the subsurface formation.

Besides safety concerns, pore pressure prediction is used to identify rock properties of formations. In short, conducting a pore pressure analysis is a pre-drill requirement which provides additional benefits to the interpreter.

1.6.2 PORE PRESSURE TERMINOLOGY

Before discussing pore pressure prediction, it is necessary to define the types of pressures which are used to constrain and describe pore-pressure trends.

They are:

1. Overburden (confining) pressure – sum of pressures exerted by overlying rock and fluids.

2. Pore pressure – pressure exerted on rock matrix by fluids within a rock’s pores.
3. Hydrostatic (normal) pressure – pressure exerted by a vertical column of water connected to the surface, typically around 0.465 psi/ft in the Gulf of Mexico.
4. Fracture (failure) pressure –pressure limit at which fractures in the formation will form if borehole pressure exceeds this limit.
5. Overpressure – difference between the pore pressure and hydrostatic pressure
6. Effective stress – difference between overburden and pore pressure
7. Mud weight (MW) – density of drilling fluid with units of (lb/gal) in GOM.
8. Abnormal pore pressure – referred to as “geopressure” or “overpressure”
9. Pressure gradients – pore pressure gradient (PPG), overburden gradient (OBG), fracture gradient (FG), hydrostatic gradient (HG), etc. refer to the change in pressure per unit depth for each type of pressure. They usually have units of (psi/ft).

(Bruce and Bowers 2002)

The interconnected relationship between pore pressure, fracture pressure, mud weight, and overburden pressure gradient curves are key to pore pressure analysis as depicted in Figure 1.18. The goal is to design and balance the mud weight curve to remain between the pore pressure and fracture gradient curves. An incorrect mud weight curve can lead to very severe complications.

There are three main issues which can occur. If the pressure of the mud being pumped into the borehole exceeds the fracture gradient, this could lead to cracks and fissures in the formation. If the mud weight is lower than the pore pressure gradient, the higher-pressure formation fluids may rupture the borehole and cause formation fluids to rush to the surface, resulting in a blowout. If the drill runs into an anomalously low pore pressure zone, a mud

weight which is too high could damage the reservoir itself. In order to find the optimal mud weight trend, a careful application of pore pressure analysis can help to increase not just safety, but potentially improve hydrocarbon extraction efficiency and productivity as well.

1.6.3 UNIT CONVENTION

At first glance, it may be confusing why the unit notation normally used for describing pore pressure is mud weight rather than psi/ft. Specifically, pore pressure *gradient* implies units with dimensions such as (psi/ft), or pressure change per unit depth. But in the industry, mud weight (lb/gal) is the standard unit for representing pore pressure gradients. Mud weight is preferred for the convenience of drilling crews. Knowing what the psi/ft value at a specific depth is not as applicable as knowing what the necessary mud weight pressure is at certain depths (Bruce and Bowers 2002).

The conversion between mud weight and psi/ft is simply (Bruce and Bowers 2002),

$$\text{Pressure Gradient } \left(\frac{\text{psi}}{\text{ft}} \right) = \text{Mud Weight } \left(\text{PPG or } \frac{\text{lb}}{\text{gal}} \right) \times 0.0519 \quad (1.10)$$

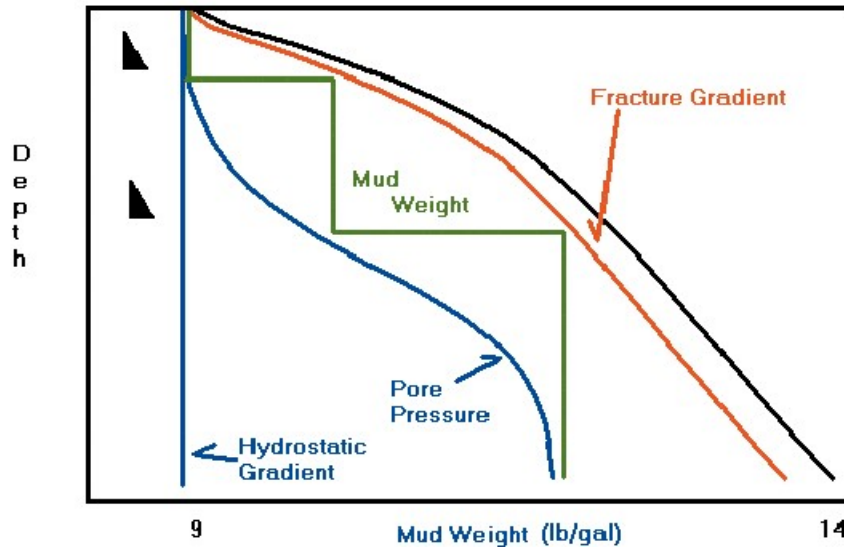


Figure 1.18 Theoretical relationship between pore pressure, fracture gradient, hydrostatic gradient, mud weight, and overburden gradient (black curve) (Bruce et al 2002)

1.6.4 OVERPRESSURE IN THE GULF OF MEXICO

Along the Gulf of Mexico's continental shelf, overpressure is generally caused by two factors, the most common being *compaction disequilibrium (undercompaction)*, and *unloading* (Yu 2013). The overpressure caused by compaction disequilibrium occurs when materials with low permeability trapping pore fluid is squeezed further by the deposition of new sediments. Unloading refers to a decrease in effective stress, which implies the difference between the overburden and pore pressure has also decreased. This occurs when the overburden pressure decreases due to processes like erosion and/or the pore pressure increases. Pore pressure increases due to fluid expansion can be caused by a variety of factors such as thermal expansion and hydrocarbon generation. Fluid expansion involves more complex processes, such as temperature increases, hydrocarbon maturation, and clay diagenesis (Bowers et al. 1995; Yu 2013). An illustration of how different overpressure mechanisms effect pore pressure is depicted in Figure 1.20.

Along the United States coast around the EI 26 survey area, the principle cause of overpressure has been found to be the smectite-illite transformation, a process which causes clay diagenesis (Bruce, 1984; Freed and Peacor, 1989). Overpressure in southern Gulf of Mexico blocks tend to originate from the compaction disequilibrium process due to lower sand and higher shale percentages.

The “onset of overpressure” or “top of overpressure” is an indicator of where the pressure trend deviates from the normal trend. Figure 1.19 displays an idealized example of how a decrease in effective pressure causing abnormal pressure can be observed in the velocity trend. In the deepwater Gulf of Mexico, the top of overpressure may be observed as shallow as a few hundred feet below the seafloor (Bowers 1995). For blocks near the shoreline like South Marsh Island and Eugene Island, the top of overpressure is expected to be considerably deeper. The depth at which the onset of geopressure occurs within the Gulf of Mexico can largely be attributed to the sand percentage. The relationship between overpressure and sand percentage is shown by the regional maps in Figure 1.21. Comparing the figures, the depth to the top of overpressure increases with higher sand percentages, with the tops of overpressure reaching maximum depth along the Louisiana coast. In particular, the EI 26 survey area is estimated to have a geopressure depth range of around 3,000-3,700 meters (10,000-12,000 feet) based on Figure 1.21.

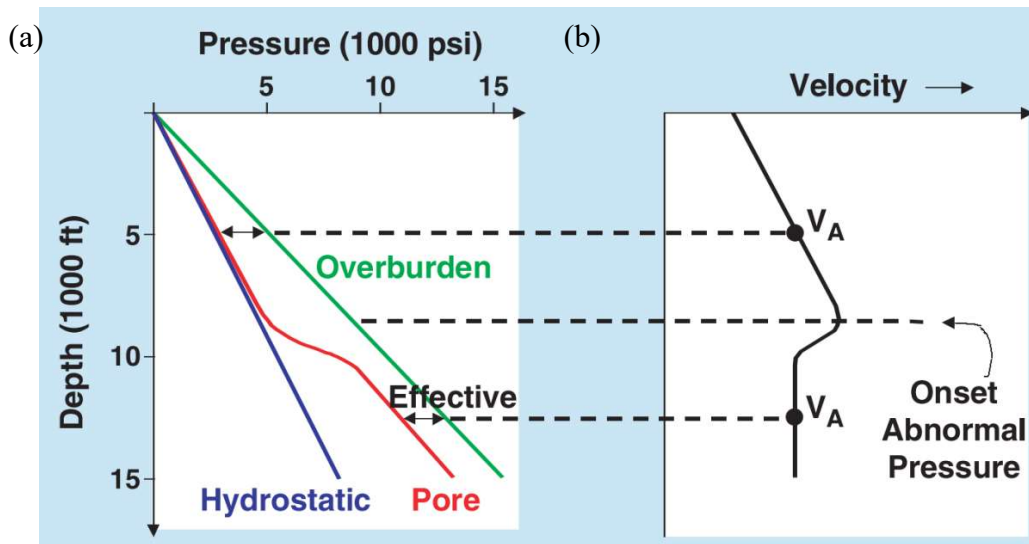


Figure 1.19 (a) Pressure vs. depth plot of a hypothetical well with a decrease in effective pressure, (b) velocity trend in a well with abnormal pressure caused by smectite-to-illite transformation (Hilterman 2001).

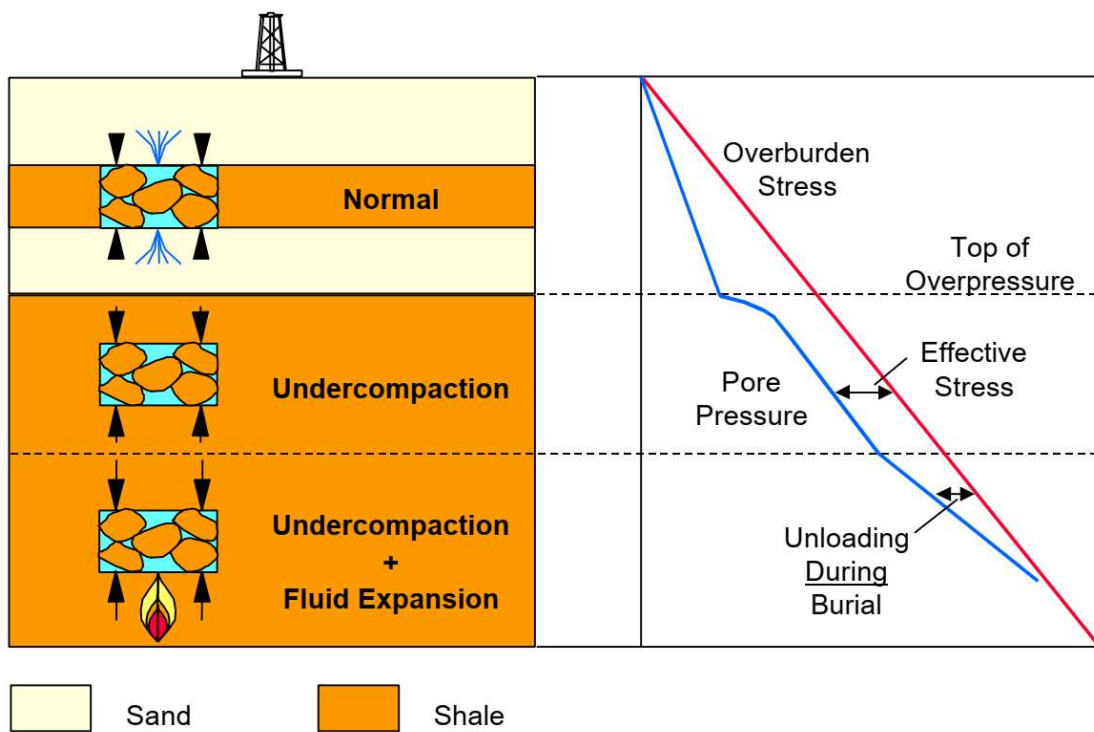
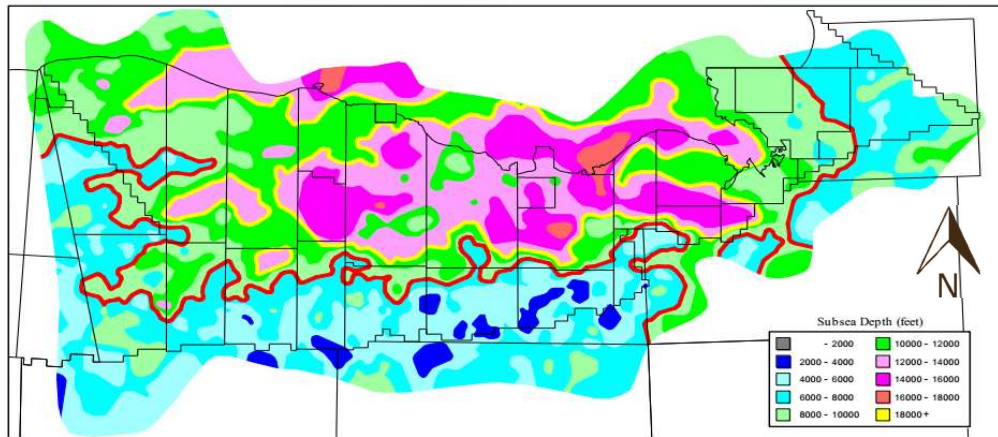


Figure 1.20 Different overpressure mechanisms' effect on effective stress, overburden minus pore pressure (Bowers et al. 2001)

(a)



(b)

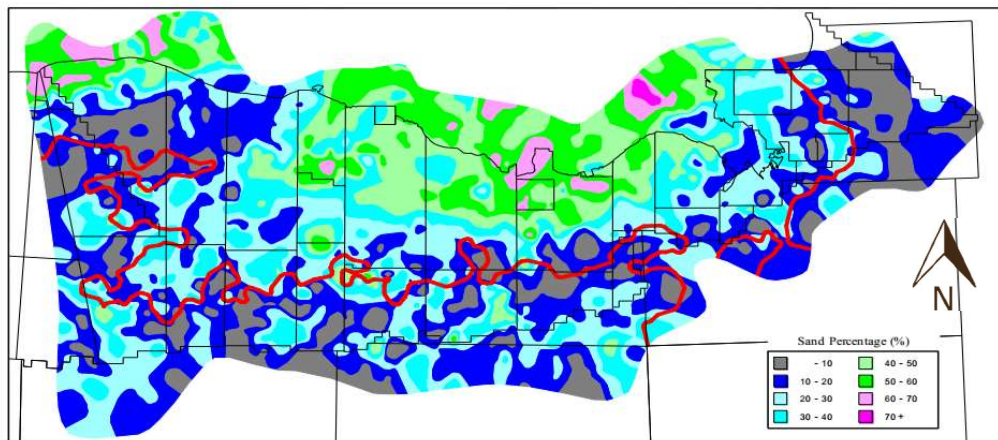


Figure 1.21 Depth of geopressure onset (a), corresponding sand percentages (b) for 7000-8000 feet (2000-2500 m) depths. Red contour represents 8000 feet (2500 m) contour line for the onset of abnormal pore pressure (Hilterman 2001).

1.6.5 EMPIRICAL METHODS FOR PORE PRESSURE ESTIMATION

There are two commonly used techniques for estimating pore pressure from shale formations that are drilled, called Eaton's Method and Bower's Method. In the equations below, pressure variables are functions of depth and refer to their respective locations at each depth point.

$$PP = S - (S - P_{hyd}) \left(\frac{\Delta t_n}{\Delta t_{log}} \right)^x \quad (1.11)$$

Eaton's method for calculating pore pressure from sonic logs is expressed in Equation 1.12, where PP = pore pressure, S = vertical or overburden stress, P_{hyd} = normal hydrostatic pressure, Δt_{log} = measured sonic log value, Δt_n = normal sonic log value, x = regional constant.

$$PPG = OBG - (OBG - P_{hyd}) \left(\frac{IntVel_{obs}}{IntVel_{nor}} \right)^x = OBG - \text{Effective stress gradient} \quad (1.12)$$

Eaton's Method for calculating pore pressure from seismic velocities, where PPG = pore pressure gradient, OBG = overburden gradient, P_{hyd} = normal hydrostatic gradient, $IntVel_{obs}$ = observed interval velocity, and $IntVel_{nor}$ = normal compaction trend for interval velocity. The exponent X can be changed to better match different regions, however, X = 3.0 is generally used in the Gulf of Mexico.

(Eaton 1972).

$$\text{Pore Pressure} = \text{Overburden Stress} - \text{Effective Stress } \sigma \quad (1.13)$$

Bowers' Method for calculating pore pressure (Bowers 1995)

Bowers assumes an Effective stress σ – velocity relationship

$$\sigma = \frac{1}{a} (V_{int} - V_{mudline})^{\frac{1}{b}} \quad (1.14)$$

This is an empirical relationship between stress and velocity where, V_{int} = interval velocity observed (m/s), $V_{mudline}$ = P-wave velocity at the mudline (sea floor or terrain surface) (m/s), while a and b are calibrated curve fitting parameters, (Bowers 1995).

Via Eaton's or Bower's method, there is an empirical method of using seismic velocity analysis to predict subsurface pore pressure trends. From either equation, accurate pore-pressure prediction requires very accurate *interval* seismic velocities, meaning interval velocity derived from conventional RMS velocities are questionable. Another implication is that a decrease in the

overall seismic velocity trend translates to an increase in pore pressure, and an increase in interval velocity will mean a decrease in pore pressure. Both methods also have variants which use highly accurate velocities derived from sonic logs, but they have significantly less spatial coverage compared to a velocity field from seismic data processing.

1.6.6 EFFECT OF PRESSURE ON SEISMIC VELOCITY

Pore pressure can change measured seismic response in at least one of four ways (Avseth, Mukerji, and Mavko 2005):

1. Increase in density of pore fluids due to increasing pore pressure, increasing velocity.
2. Porosity levels are maintained due to anomalous overpressure, decreasing velocity.
3. Compaction of material with increasing depth of burial reduces porosity, increasing velocity.
4. Stiffening of rock matrix due to increasing effective pressure reduces porosity, increasing velocity. Generally, an increase in effective pressure nearly always leads to higher seismic velocities.

From the equations in Eaton's and Bower's method, we can empirically determine the effect of pore pressure on seismic velocity. Since the equations depend on the subtraction of the observed over normal velocity fraction, a decrease in the overall seismic velocity trend translates to an increase in pore pressure, and an increase in interval velocity will mean a decrease in pore pressure. Consequently, since abnormal pore pressure reduces seismic velocity, measured AVO signatures and hydrocarbon responses will also be affected.

2. PROJECT WORKFLOW

The Fairfield speculative dataset for EI 26 dataset is not true raw data because Fairfield has already performed basic trace editing, statics, and deconvolution, as detailed in Figure 2.1. A processing report for the dataset was not available, so it is possible additional processing was performed by Fairfield. However, the SEG-Y header did include a basic outline of major processing steps which are included in the same figure. The following sections provide a detailed workflow of the seismic dataset for EI 26 that was processed through Geosystem Development Corporation's **GBSYS** program; the workflow itself is outlined in Figure 2.2.

Furthermore, the AVO and pore pressure processing workflows are outlined in Figure 2.3 and Figure 2.4, respectively.

It is important to reiterate that the processing workflow used in this thesis is restricted to **relative** amplitude processing, designed specifically for the application of later techniques such as AVO analysis which rely on amplitude information. More general processing procedures may use AGC (Automatic Gain Control) or spectral balancing, which can be harmful and destructive to amplitude variations. Such methods are used to make the seismic data more attractive and vibrant on a display, but also have the potential to be misleading.

It is also important to note that seismic processing is not an objective task. There will always be differences in processing between companies and individuals. Even using the same software package and following the same steps, different processors can produce very different results. One approach is not necessarily superior to another, but for interpretation, it is necessary to keep in mind the final seismic section is inherently biased.

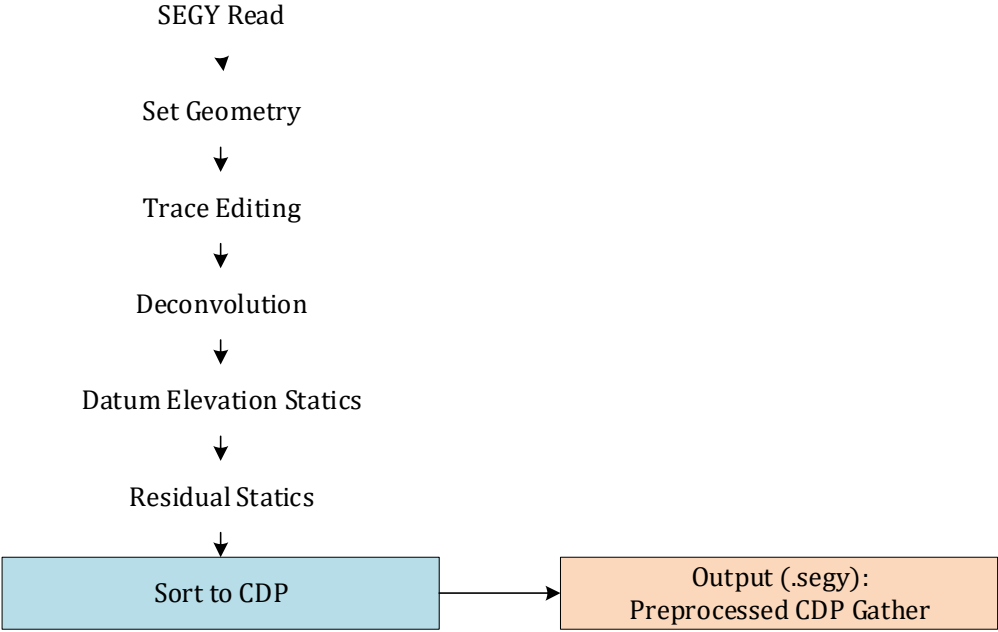


Figure 2.1 Fairfield preprocessing workflow for the EI 26 survey dataset.

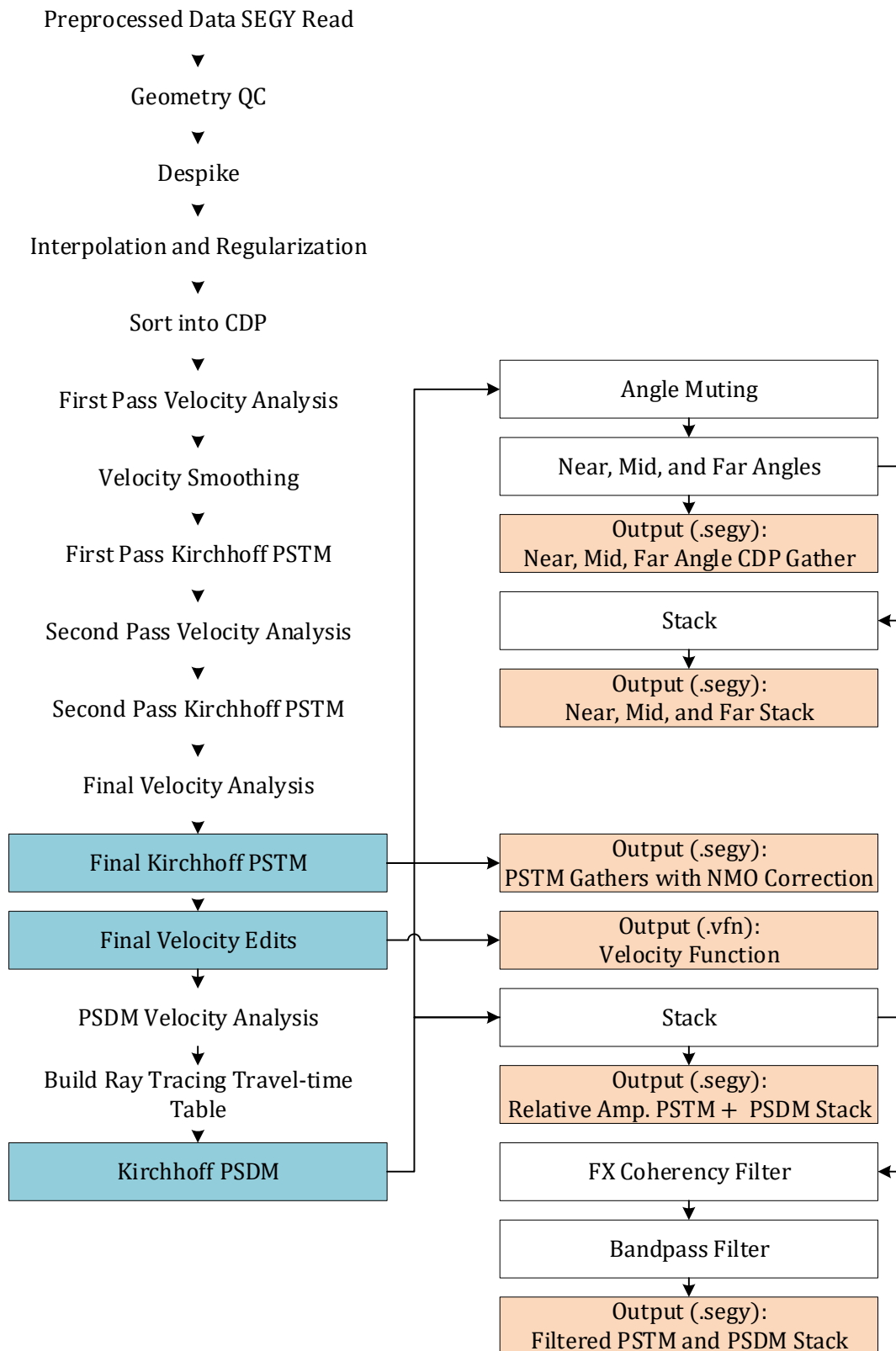


Figure 2.2 Seismic data processing workflow for EI 26.

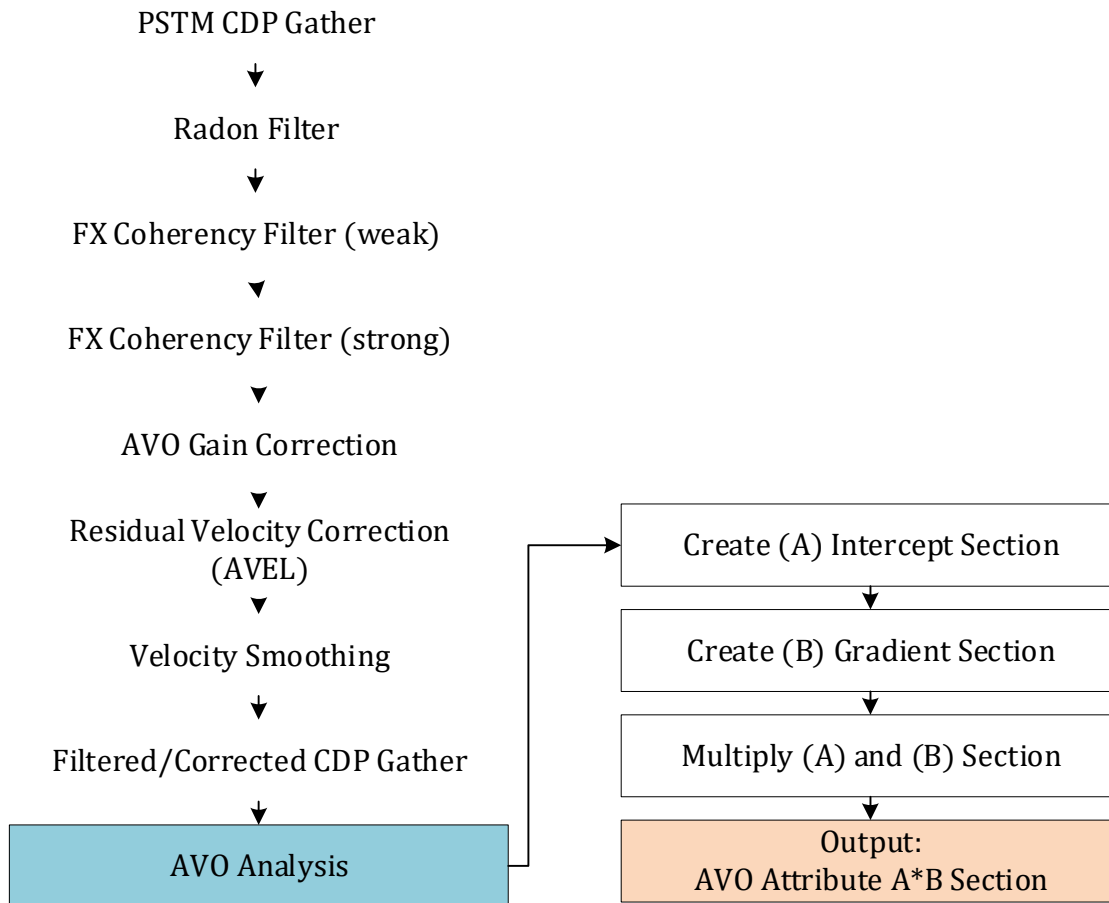


Figure 2.3 AVO processing workflow for EI 26

2.1 PROCESSING DESCRIPTION

Detailed, mathematical discussion of the processing techniques used will be avoided, not because it is trivial, but because such discussion is too theoretical given the practical goal of this paper. For the sake of brevity, the major processing steps will be summarized and evaluated based on their intended result.

The following subsections discuss in order the individual steps outlined in the processing flowchart Figure 2.1.

2.1.1 TRACE EDITING

During seismic acquisition, occasionally unfavorable conditions can cause what are known as “bad traces”. These can be due to a broken geophone (hydrophone), poor receiver placement, local noise, or even interference from wildlife and fish. Bad traces can be recognized by zero amplitudes at all times, signals that appear completely out-of-place next to other traces, or extremely high energy noise content. These traces contain negligible information about subsurface reflections and therefore need to be removed. This removal process is called trace editing. This process can be fairly labor intensive, as the processor needs to visually scan every trace and manually remove undesirable traces.

2.1.2 DECONVOLUTION

Deconvolution attempts to shrink the seismic wavelet into a spike or a known wavelet. This has the effect of improving resolution, reducing reverberations, and making the seismic wavelet consistent for each reflection. Fairfield specifically applied what is called “spiking deconvolution”.

2.1.3 STATICS CORRECTION (ELEVATION AND RESIDUAL)

The statics correction can be broadly described as a time shift for an entire trace to compensate for a variety of factors.

ELEVATION STATICS

Because the EI 26 survey was performed via ocean-bottom cable, or OBC, the receivers have different elevations corresponding to their location on the ocean floor. In order to remove the elevation effect from the data, a datum elevation static correction can “move” all the receivers to the mean sea level.

RESIDUAL STATICS

After performing the NMO correction, events between traces still may not line up as desired. These errors are typically small and are corrected via the residual statics correction.

The following subsections discuss in order the individual steps outlined in the processing flowchart in Figure 2.2.

2.1.4 RANDOM SPIKE NOISE ATTENUATION

Despike attenuates anomalously high amplitudes which have a negative effect on later processing techniques and therefore need to be removed.

2.1.5 DATA INTERPOLATION AND REGULARIZATION

Seismic data often has issues with missing information and irregular sampling, possibly due to acquisition design or equipment flaws. Interpolation and regularization are useful tools for satisfying the acquisition assumption upon which certain processing algorithms are based.

Interpolation fills in missing data and regularization is a method for making the seismic data more grid-like and evenly sampled, which is beneficial for migration algorithms.

2.1.6 CMP GATHER

The CMP (Common Mid-Point) gather is a special configuration for sorting seismic traces such that every trace within a CMP gather corresponds to the same surface midpoint between the trace's source and receiver locations. Sorting the traces into this configuration allows for the application of processing techniques, namely NMO corrections and stacking.

2.1.7 NMO CORRECTION

The normal moveout (NMO) traveltime curve refers to the hyperbolic relationship between traveltime and offset. From Sheriff (1995), the NMO equation is represented as:

$$t^2 = t_0^2 + \frac{x^2}{v^2} \quad (2.1)$$

where t_0 = traveltime at zero offset, t = recorded traveltime, x = offset, v = velocity of the medium.

Therefore, in a CDP gather, a reflection from a flat layer will appear as a hyperbolic curve. The purpose of the NMO correction is to remove the NMO or traveltime-offset effect, making it possible to stack CDP sections together.

2.1.8 VELOCITY ANALYSIS

Velocity picking is one of the core fundamentals of seismic data processing. Velocity analysis is performed by selecting CDP gathers at certain intervals and from that, creating a semblance gather, which can be thought of as a velocity spectrum. The semblance gather provides an indication of which velocity values provide the highest coherency when the traces are stacked. The CDP and semblance gather are placed side-by-side, so a processor then "picks" a specific velocity which applies the best (flattest) NMO correction. The process of picking

velocities is a labor and time-intensive task since it requires several iterations and significantly affects the quality of the final results, so it needs to be done carefully and accurately.

First Pass Velocity Analysis

The first pass was done at sparse intervals, the goal is to establish a baseline velocity trend before going into more detail in later passes. Velocities were picked every 40 lines, every 150 CDP, and approximately every 0.5 seconds.

Second Pass (Migration) Velocity Analysis

Using the first pass velocity field, migration is applied to take advantage of Kirchhoff migrations' focusing capabilities. If the first pass velocities were adequate, the semblance gather should be improved, highlighting the optimal velocity ranges. Post-migration velocities were picked every 20th line, every 60th CDP, and generally every 0.050 seconds but as fine as necessary depending on the data quality.

Final Pass (Migration) Velocity Analysis

Using the second pass velocity field, migration is reapplied. The difference in signal quality between the final and second pass may not be as large as between the second and first pass, but repeated velocity picking is important for steadily improving the accuracy of the velocity field. Again, post-migration velocities were picked at the same spatial interval and frequency as previous velocity analyses were picked.

Final Velocity Edits

Before finalizing the velocities, the velocity field is edited to remove any sharp "edges" in the data. For Kirchhoff migration, the velocity changes should be smoothly varying. By plotting the velocity field with the individual picks overlaid, the picks are slightly adjusted to smooth the velocity field.

For best results, velocity analysis should be performed by a processor and directed by an interpreter. Alone, the processor can only depend upon the semblance gather for guidance, which can be unreliable in very complex geologic environments. But if an interpreter indicates for example, that there is a known low-velocity layer around 3 seconds deep with estimated P-wave values, this knowledge can dramatically influence how the final image appears. Another example is the presence of salt bodies, which introduces additional challenges to velocity picking. Salt domes require manual picking of the salt formation and the application of a constant velocity (~4,300 m/s in the GOM) to that area. The stark density contrast between salt and the surrounding rock also makes it difficult to image events below the salt itself.

2.1.9 STACK

The stack is one of most powerful and well-known techniques associated with seismic processing. Compared to other signal processing techniques, the stack is also one of the simplest in concept, which is the summation of seismic traces together to produce a single trace. This method depends on the idea of wave interference, where ideally the coherent signal across many traces constructively interferes whereas noise destructively interferes or “stacks out”. Stacking many individual CDP gathers produces the quintessential “stack section”. Stacking must be applied to NMO corrected CDP gathers, so that flat events stack coherently.

2.1.10 MIGRATION

Seismic migration is primarily used for its ability to move reflection energy into its correct position in space and time. This process also has the added benefit of enhancing signal quality and reducing overall noise. In order to perform migration, it typically uses a wave equation approach, and a velocity model which is approximately correct. Migration can also be split into four categories, Post-Stack Time Migration, Post-Stack Depth Migration, Pre-Stack

Time Migration (PSTM), and Pre-Stack Depth Migration (PSDM). As their names imply, there are two main features of note for migration, pre-stack or post-stack, and time or depth. Generally, modern processing centers only use pre-stack migration methods thanks to significant improvements in computing speeds. Therefore, the migration options shrink to PSTM and PSDM. PSDM is very computation-expensive compared to PSTM so the choice may be restricted based on project deadlines and processing power.

Figure 2.5 compares the four types of migration categories based on how they handle certain geologic conditions as well as their respective costs. There are numerous migration algorithms that are currently applied to seismic data, but this research will only be concerned with Kirchhoff migration methods. Depending on how well the Kirchhoff algorithm is written, generally PSDM takes at least twice as long as PSTM. In terms of the Kirchhoff method, depth migration involves ray tracing, which is the most calculation intensive portion of the process.

The main difference between time migration and depth migration is their assumed velocity model. Time migration assumes there is no lateral change in velocity. Depth migration on the other hand accounts for lateral velocity variations, which makes it more versatile but also more expensive. Because of this difference in velocity assumptions, if the local geology is determined to have a relatively smooth and well-behaved lateral velocity function, PSTM is normally sufficient in imaging the subsurface. If the local geology displays significant changes across the survey and contains high dip layers, PSDM may be required.

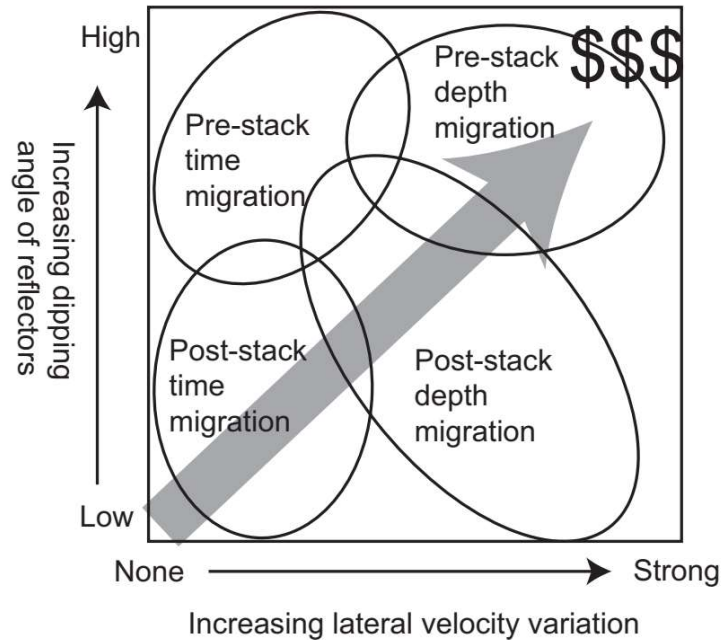


Figure 2.5 Comparison of four types of migration methods based on how they handle dip, lateral velocity changes, and cost (Zhou 2014, Liner 1999).

2.1.11 ANGLE MUTE

Angle muting involves limiting CDP gathers to a certain range of incident reflection angles, which are usually divided into three sections called near, mid, and far angles. Stacking the angle muted gathers then produces angle stacks. These can be used to help in pore-fluid and lithology discrimination. Typically, the far angle is limited to around 45 degrees or so, but with the very-far source-receiver offsets involved with this data set, the angle-mute limit was set to 70 degrees.

Angle Mute Parameters	
Near	0-15 degrees
Mid	15-30 degrees
Far	30-70 degrees

Table 3 Range of angles used for creating different angle gathers

2.1.12 RADON FILTER

The radon filter is a method commonly used for the attenuation of multiples and artifacts. Compared to other filters, radon filtering should be treated and applied very carefully because it is capable of significantly degrading near-offset signals.

2.1.13 FX COHERENCY FILTER

The FX filter attempts to remove incoherent noise from the input data. As the first part of the name implies, the process involves transforming the input gather into the frequency-space domain. The filter operates on the assumption that noise is spatially unpredictable, while signal is spatially predictable. By using linear prediction, what is spatially unpredictable is subtracted from the data and then it is transformed back into the time domain.

2.1.14 RESIDUAL VELOCITY ANALYSIS (AVEL)

Velocity picking is a subjective task, and small errors are inevitable and unavoidable. Originally developed by Swan (2001), AVEL is a method capable of minimizing errors in a velocity field, given that these errors are smaller than two-three percent. This improves the overall flatness of reflection events and therefore increases stacking potential. A flat response is of particular importance for AVO analysis and a high-resolution velocity field is crucial for pore pressure analysis.

3. PROCESSING RESULTS AND INTERPRETATION

This section will display the results of the processing workflow outlined in Figure 2.2.

3.1 PROCESSING QUALITY CONTROL

The EI 26 dataset already has geometry data, but it is still necessary to double check to ensure the integrity of the dataset and that the geometry has been read in correctly. One method for double checking is to display the fold map, which should outline the rectangular shape of the survey as in Figure 3.1. Although the data is marine-based, the acquisition method was completed via OBC or ocean bottom cable, which explains the survey pattern. The sharp discontinuity is a true representation of the survey, which could have been due to leasing restrictions, physical obstacles, or a variety of other acquisition difficulties. If the geometry was incorrectly defined, then the fold map likely would not form anything resembling the survey area.

It is also necessary to confirm receiver and shot positioning. Figure 3.2 displays the previous fold map but with survey lines overlaid on top. Each red dot indicates a receiver position. Overall, receiver lines are approximately linear although some lines have receivers which deviate from a straight line. For individual shots, typically only nearby receivers are set to be actively listening. Figure 3.3 displays a single shot, and which corresponding receivers were active and listening at the time. The active receivers span both sides of the shot and follow the survey pattern. If there were receivers listening at locations that did not make sense, such as at the far edges of the survey when the source is near the center, this would be an indication of incorrect geometry.

Figure 3.4 is a plot of the original, preprocessed CDP gather, and Figure 3.10 is the stack of Figure 3.4, where there are certain observations that can be made for deciding on a course of action.

1. Data spikes in the CDP gather are present and need to be attenuated. These also appear towards the bottom of the stack section. Additional data conditioning in addition to the preprocessing is necessary.
2. Reflection events are observable in the CDP gather and stack which is promising but are degraded by noise and artifacts. Particularly in the stack section, there are event crossovers which are indicators of synclinal features. These issues can be remedied through further processing, especially migration.
3. Some faults are already recognizable prior to migration, so it will be important to enhance these features and ensure that they are not lost after each processing step. Some interpolation applications may smooth over fault features which can significantly alter the data interpretation.
4. From the stack comparison in Figure 3.10, the region below ~3.5 seconds has more complex geology (higher dipping angles). This may make it difficult to obtain a clean image at larger depths. Anisotropy may also complicate imaging even further.
5. Because the data was acquired via OBC, the preprocessed CDP stack section (Figure 3.10) does not display the stereotypical ocean bottom reflection for marine data. The ocean bottom reflection in marine data is typically very strong due to the high impedance contrast between sea water and rock sediments. But since the receivers were in direct contact with the ocean bottom, the survey is more similar to land data, which is characteristically noisy.

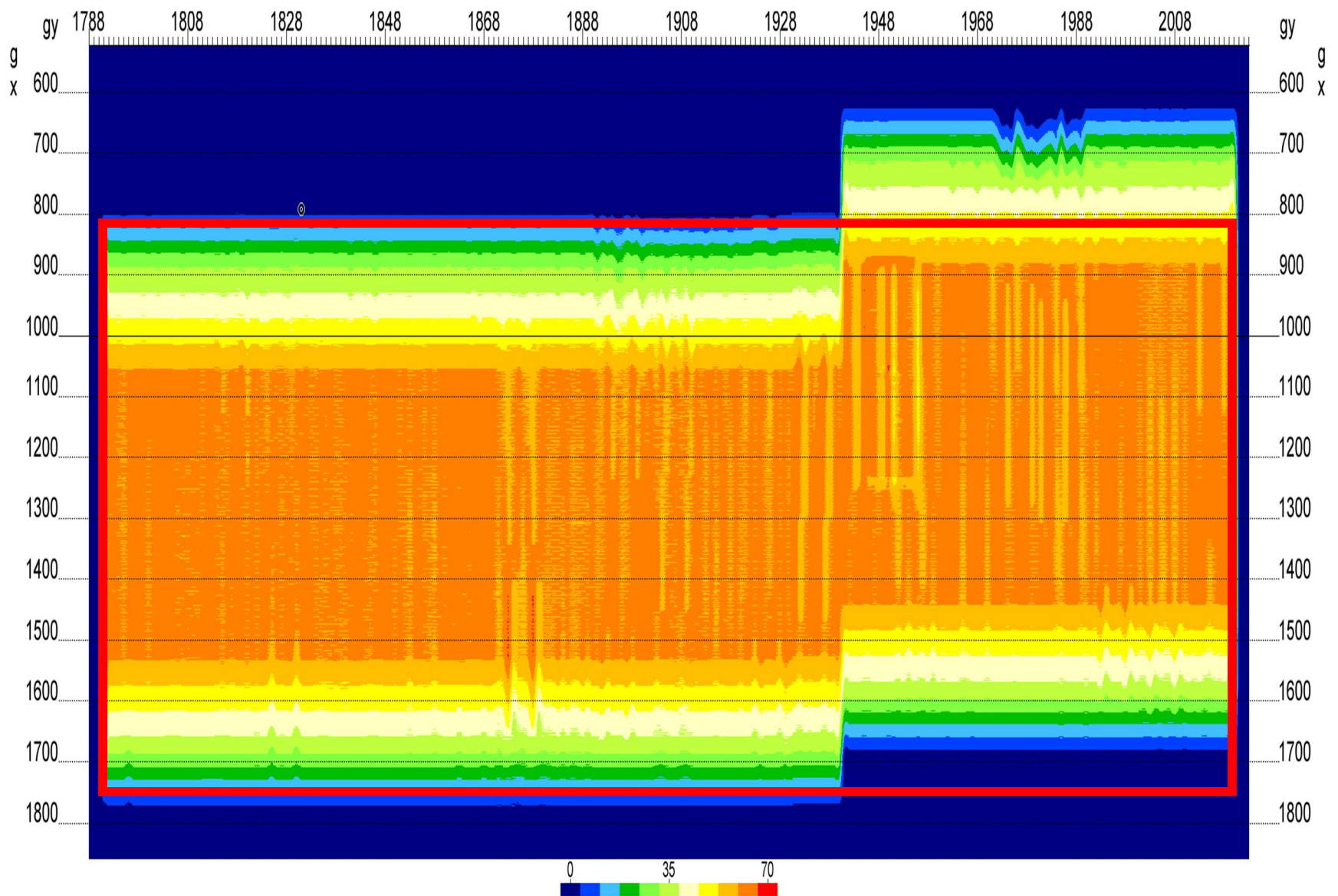


Figure 3.1 EI 26 Fold map. Fold ranges between 0 to 70. Red rectangle represents the area of the survey being processed.

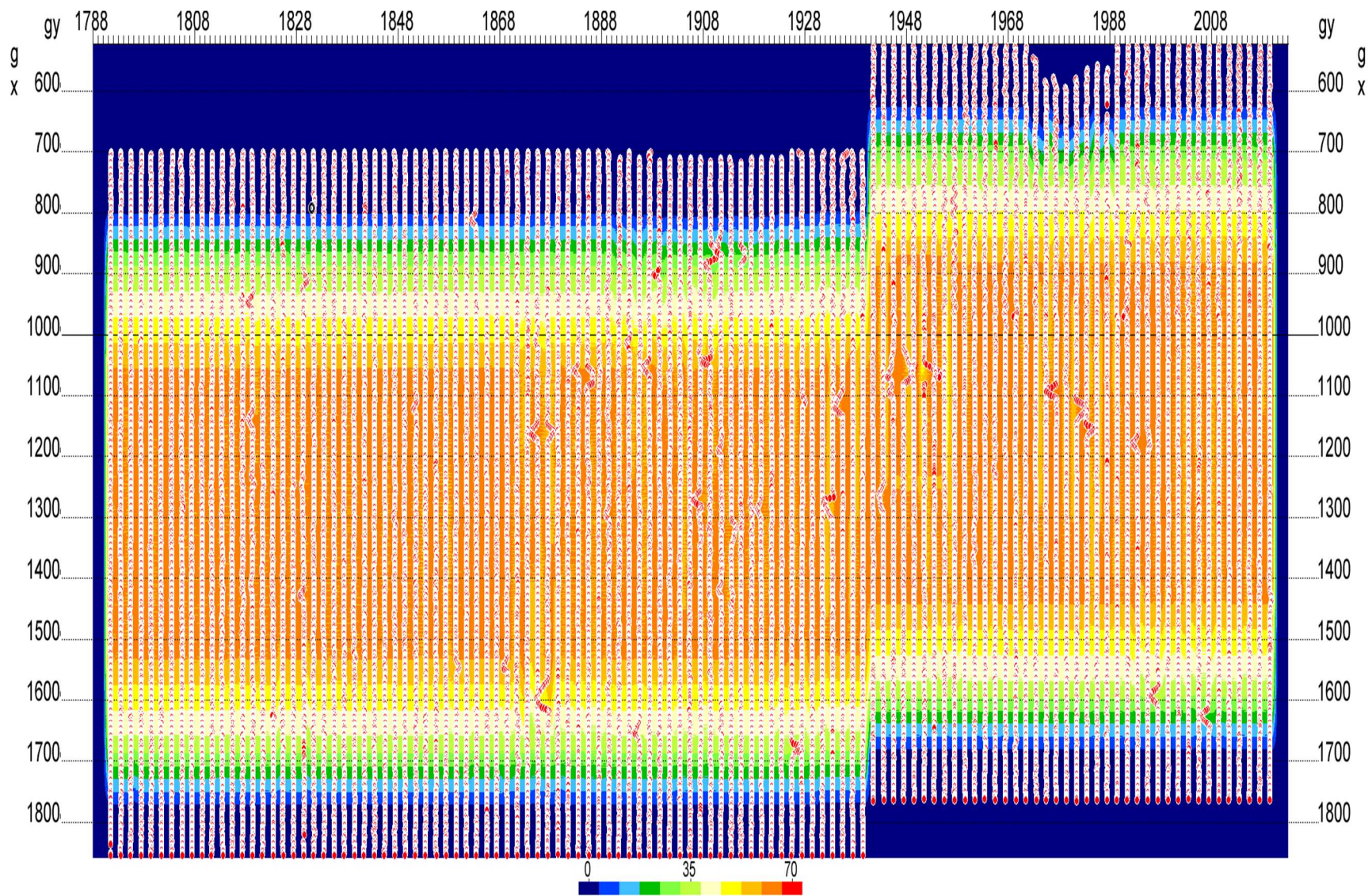


Figure 3.2 EI 26 Fold map with the survey line placement overlaid on top. Some lines have irregularities in their placement, but overall the lines are sufficiently straight and evenly spaced.

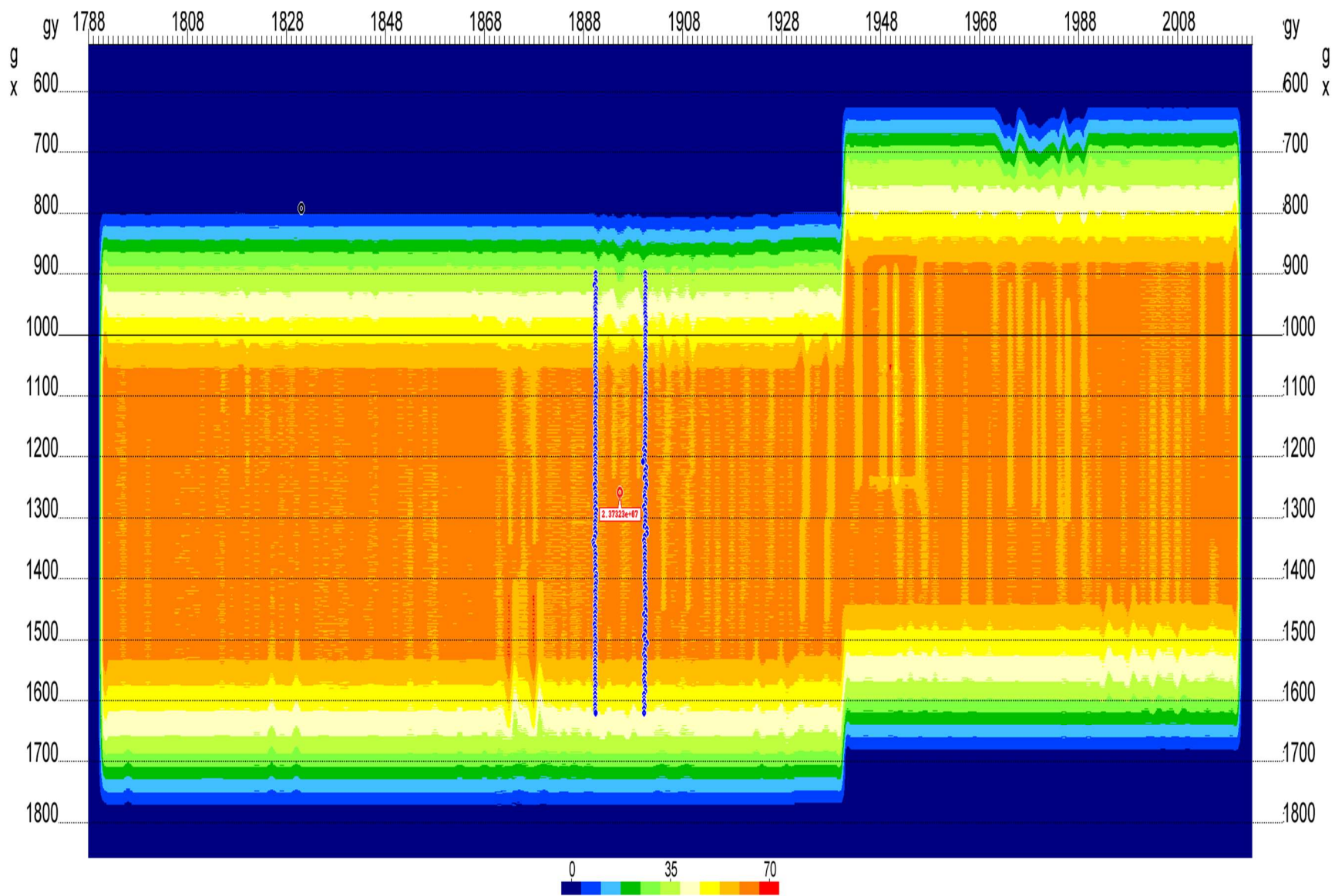


Figure 3.3 EI 26 Single shot display. A shot is indicated with the red circle and active receivers are blue dots.

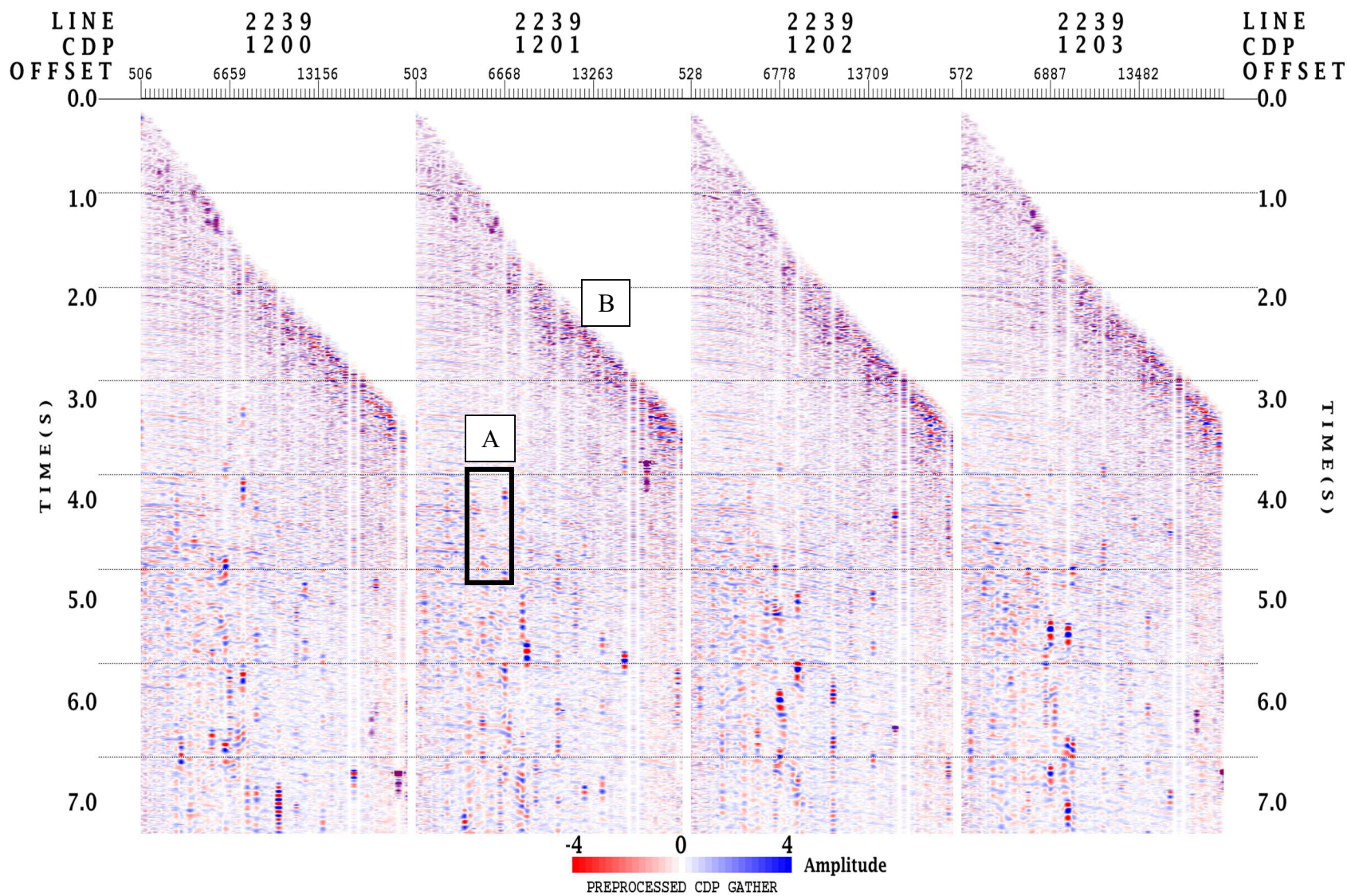


Figure 3.4 Preprocessed CDP gather with statics and deconvolution pre-applied by Fairfield where there are (A) data spikes which need to be attenuated, and (B) muted (empty) traces which were removed previously by Fairfield.

3.2 VELOCITY ANALYSIS COMPARISON

The end result of a velocity analysis is a velocity field, which is a series of hand-picked velocity values at CDP points throughout the survey area. This velocity field is used to calculate the NMO correction and flatten the CDP gather, making it possible to stack. The actual process of velocity picking is straightforward, the semblance and CDP gather are placed side-by-side and velocity picks are made at “hot spots” on the semblance gather.

Starting from the top, a processor works from time zero downwards and attempts to pick the velocity which best flattens events on the CDP gather. After making a series of picks at different times, a velocity trend is created. By following the trend of peaks in the semblance gather, it helps to outline a range of suitable velocities based on their coherency values. In this fashion, the processor picks velocities at different CDP locations across the survey, creating a velocity field as a result. This process is typically repeated multiple times inside a processing workflow and is usually one of the more time-consuming tasks.

The initial (before migration) velocity picking panel with a semblance and CDP gather is shown in Figure 3.5, the final PSTM velocity panel in Figure 3.6, and the final PSDM velocity panel in Figure 3.7. Based on the intensity of the colors in the chain of semblance gathers from preprocessed-to-PSTM-to-PSDM, the improvement in signal coherency is very noticeable. From the semblance gather in Figure 3.7, there appears to be a geopressure top picked around 3.0 seconds which should indicate an onset of abnormal pressure region. This can be estimated by superimposing two trend lines upon the image, and where the two lines intersect should indicate the onset of abnormal pressure.

Figure 3.8 and Figure 3.9 are the smoothed PSTM and PSDM picked interval velocity fields, respectively. The PSTM velocity field is much smoother and displays an “eye” or a

velocity reversal between 3 and 4 seconds. Comparatively, the PSDM velocity field contains more high frequency content, and the velocity reversal extends further across the section. The “rippling” in the PSDM velocity field is not necessarily intended to be an accurate geologic representation of the actual rock properties. In Figure 3.9, it appears as if the velocity control point for several CDP locations such as CDP 1650 have an “anomalous” pick around 3.5s. Removing this will make the PSDM field more similar to the PSTM field in Figure 3.8. The “anomalous” picks are not necessarily incorrect however. The benefits of PSDM includes better accountability for lateral velocity variations which in turn affects the semblance and CDP gather. Based on the velocity picking results, it could be interpreted that the area around 3.5 seconds exhibits a relative increase in lateral velocity variations which is emphasized by PSDM.

Because the primary concern for velocity analysis is to flatten events as much as possible, the resulting field often contains sharp edges and irregularities. Velocity smoothing is performed afterwards to smooth the velocity field, since geological events are generally smooth as well.

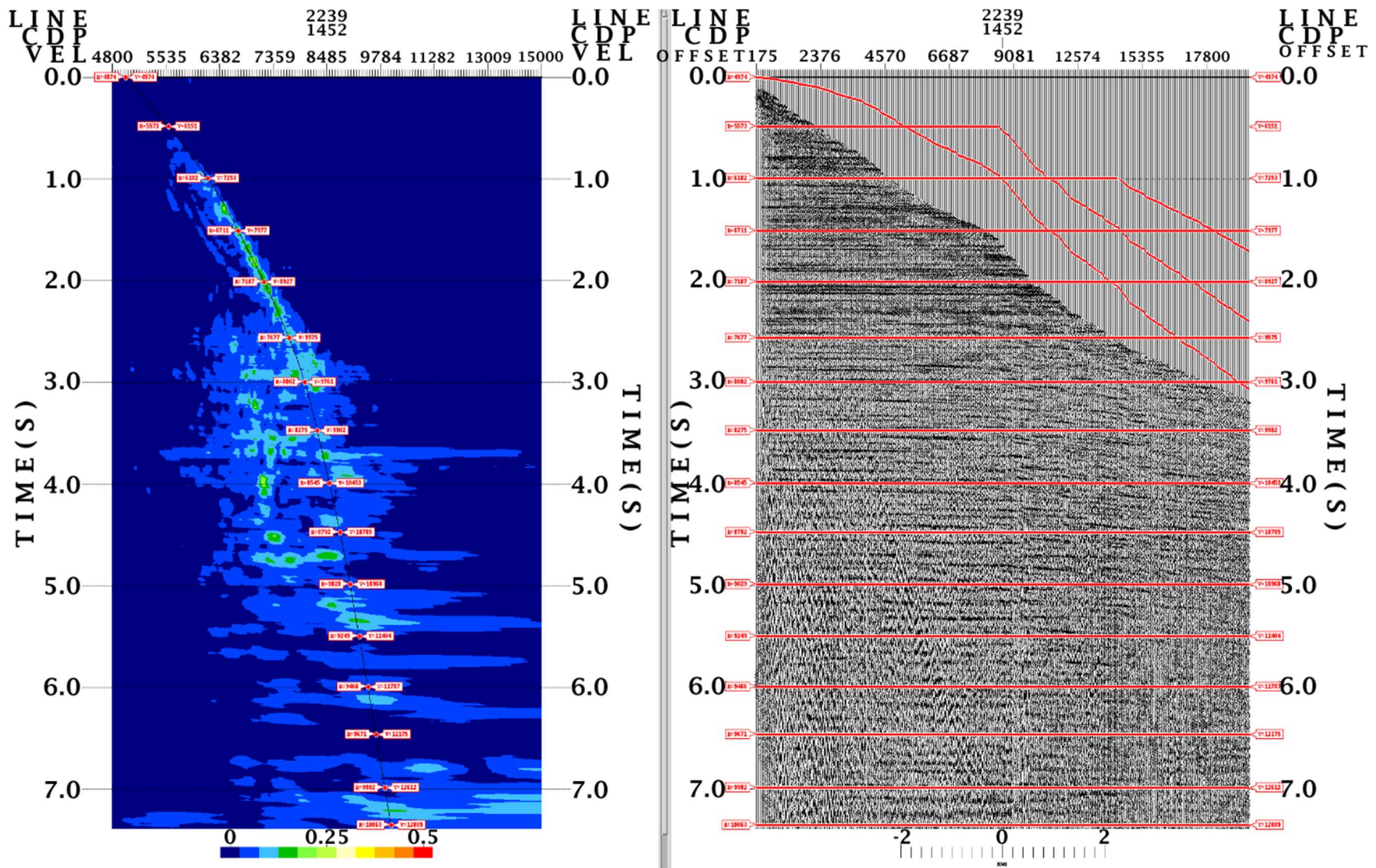


Figure 3.5 Initial interval velocity picking panel with semblance gather (left) and CDP gather (right) with NMO correction applied based on picks. The semblance gather only shows a faint trend, likely due to high noise in the CDP gather.

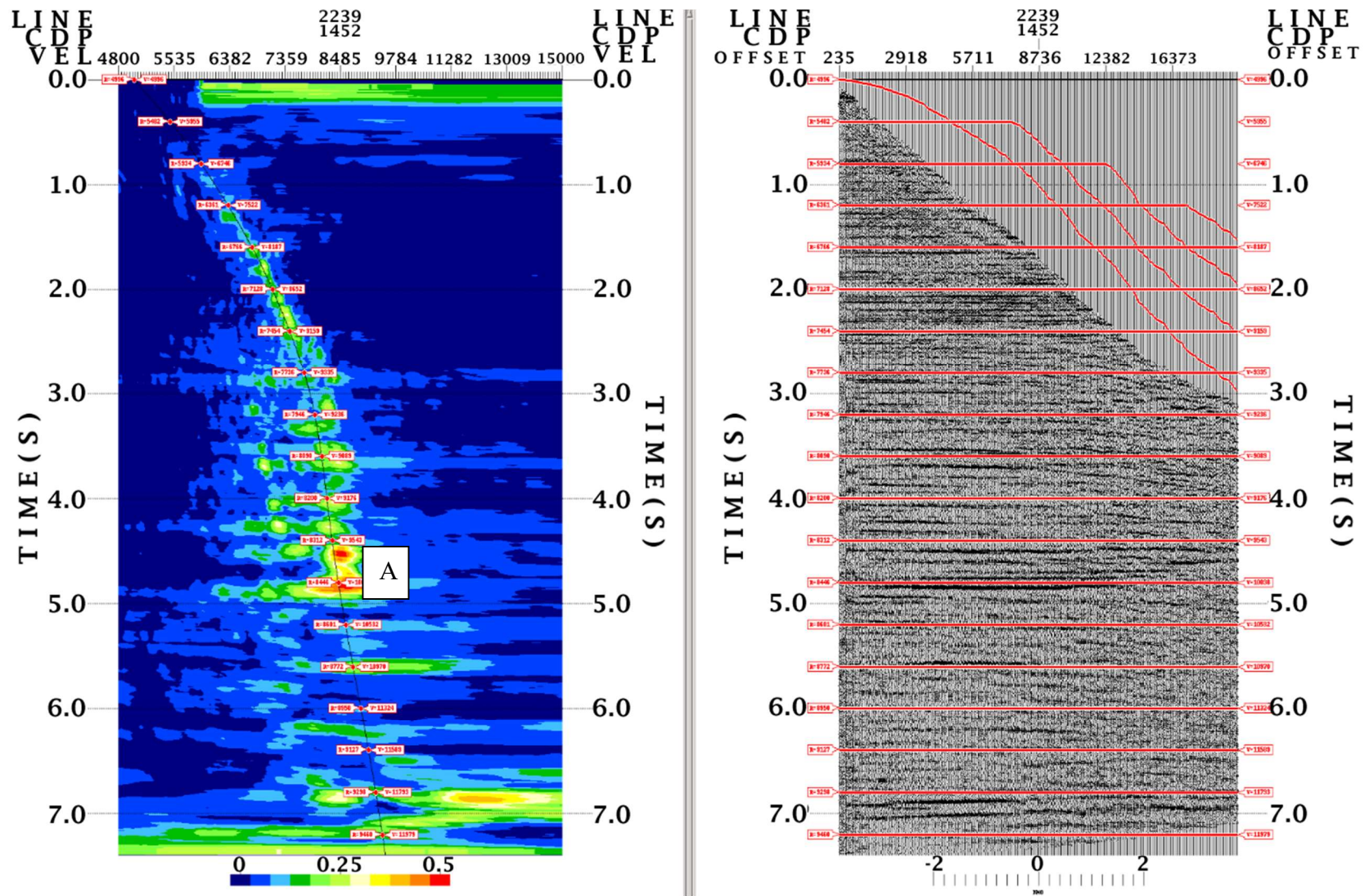


Figure 3.6 Final PSTM interval velocity picking panel with semblance gather (left) and CDP gather (right) with NMO correction applied based on picks. (A) indicates a high coherency zone in the semblance gather, which overall has noticeably stronger peaks and a clearer trend.

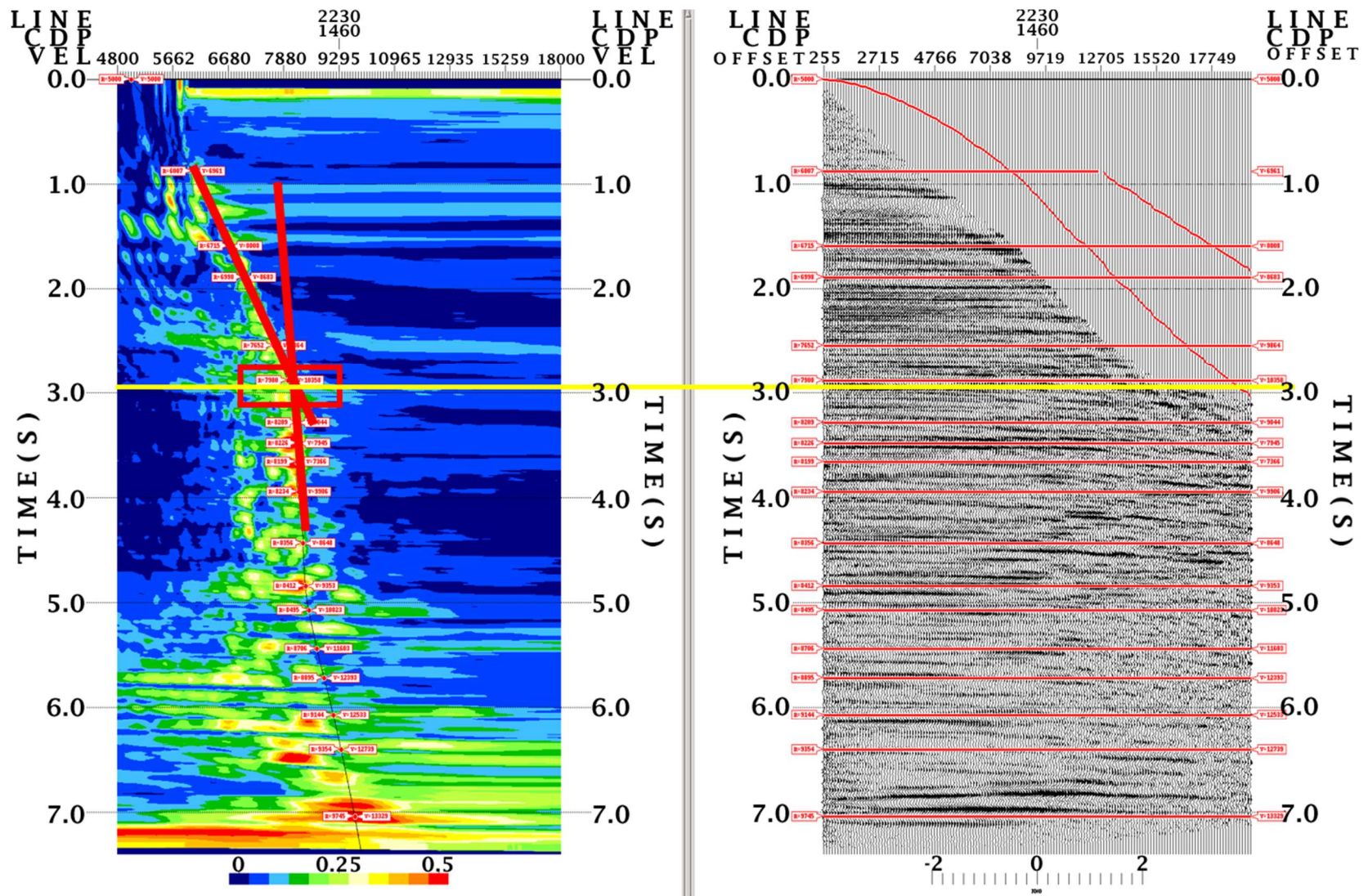


Figure 3.7 Final PSDM interval velocity picking panel with semblance gather (left) and CDP gather (right) with NMO correction applied based on picks. The PSDM semblance gather shows an improved coherency trend over PSTM. Red box indicates top of geopressure.

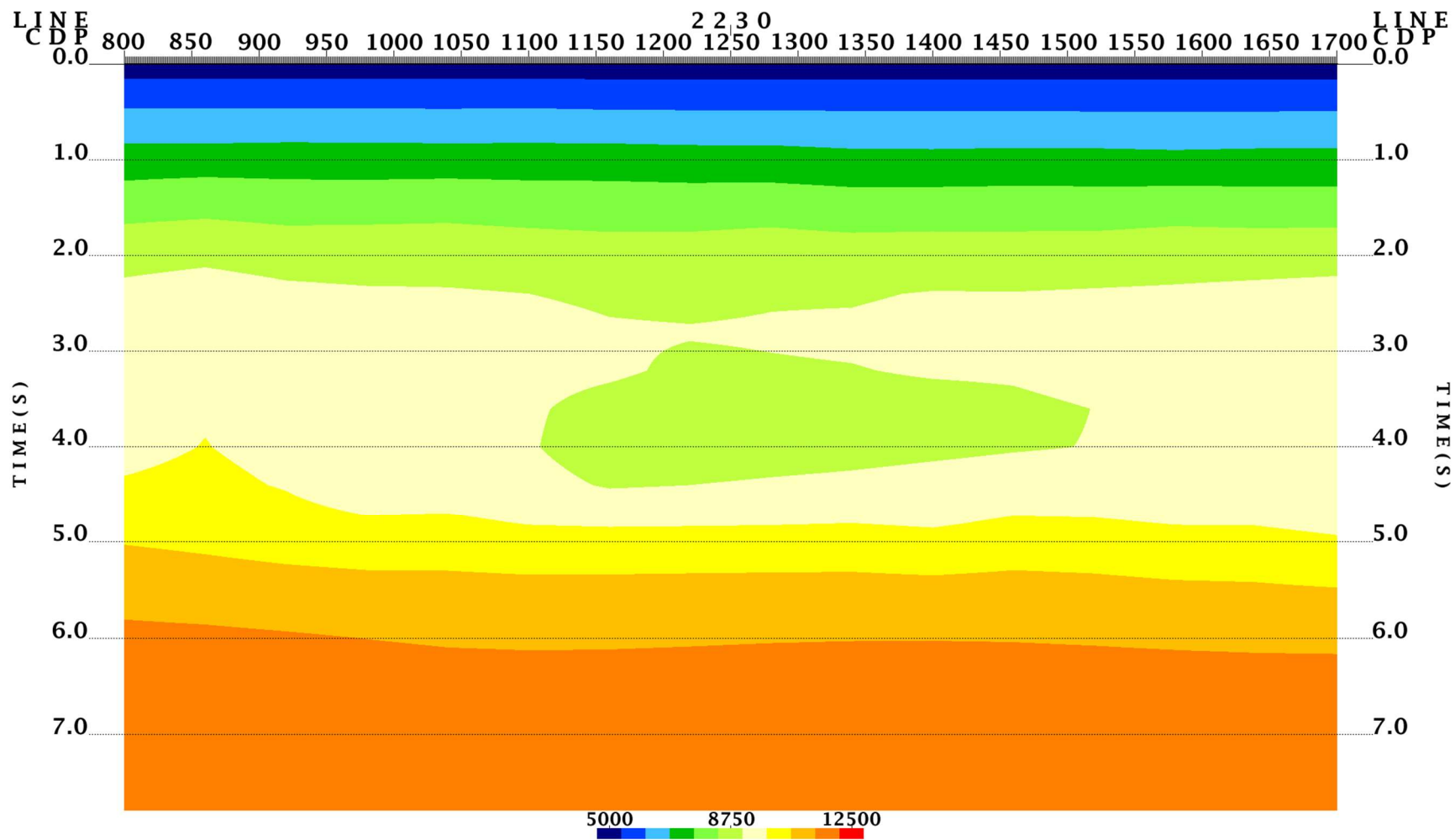


Figure 3.8 Smoothed interval velocity field from Kirchhoff PSTM velocity analysis. The main feature is the low velocity zone in the center of the field. Otherwise, the velocity trend is largely smooth in the vertical and lateral sense.

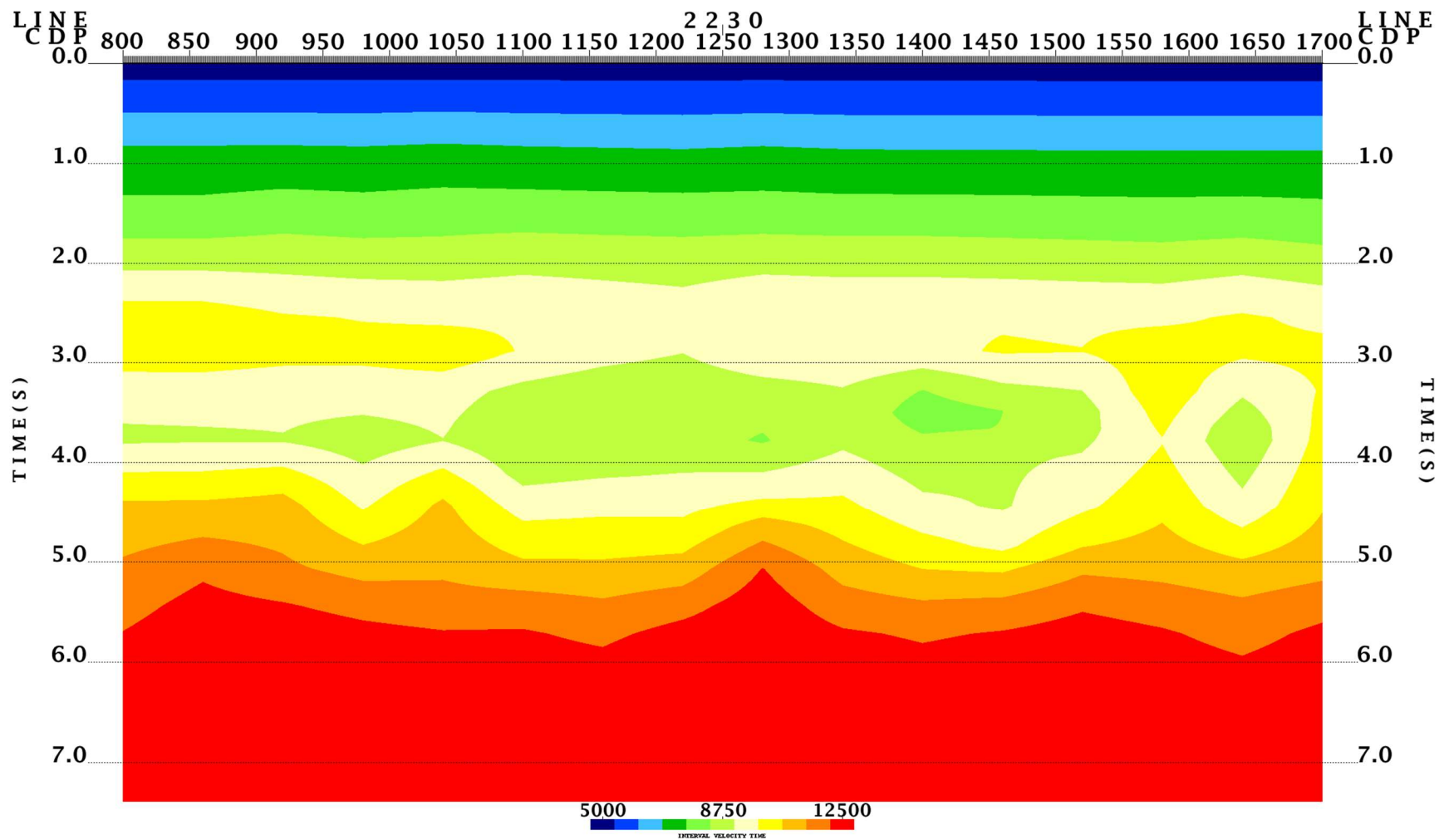


Figure 3.9 Smoothed interval velocity field from Kirchhoff PSDM velocity analysis. Compared to the PSTM velocity model, the PSDM velocity field shows a more nuanced low velocity zone at around the same time.

3.3 STACK COMPARISON

Figure 3.10, Figure 3.11, and Figure 3.12 show the full stack section across a single line at the stages of preprocessed, pre-stack time migrated, and pre-stack depth migrated, respectively. Figure 3.13, Figure 3.14, and Figure 3.15 display a comparison between the preprocessed stack and the PSTM stack section at different time intervals. Figure 3.16, Figure 3.17, and Figure 3.18 display a comparison between the PSTM stack and the PSDM stack section at different time intervals. For consistency, the PSDM section was first converted into time using the depth migrated velocity field. Generally, signal strength, event continuity, fault continuity, and artifacts have been greatly improved across the board after migration application. Particularly in the area around ~3.5 seconds, events are significantly more pronounced after PSTM compared to the preprocessed section.

Overall, PSDM has helped to increase both the quality of the velocity picking and the resulting stack section. Signal strength and fidelity has been boosted and events appear more continuous. One major difference in terms of PSTM vs. PSDM is in areas which require PSDM, the velocity analysis process is more interpretation-oriented since it must match the geologic velocity model more closely. PSDM is more applicable in areas with complex lateral velocity variations, which typically involves the presence of salt bodies or other major geologic changes.

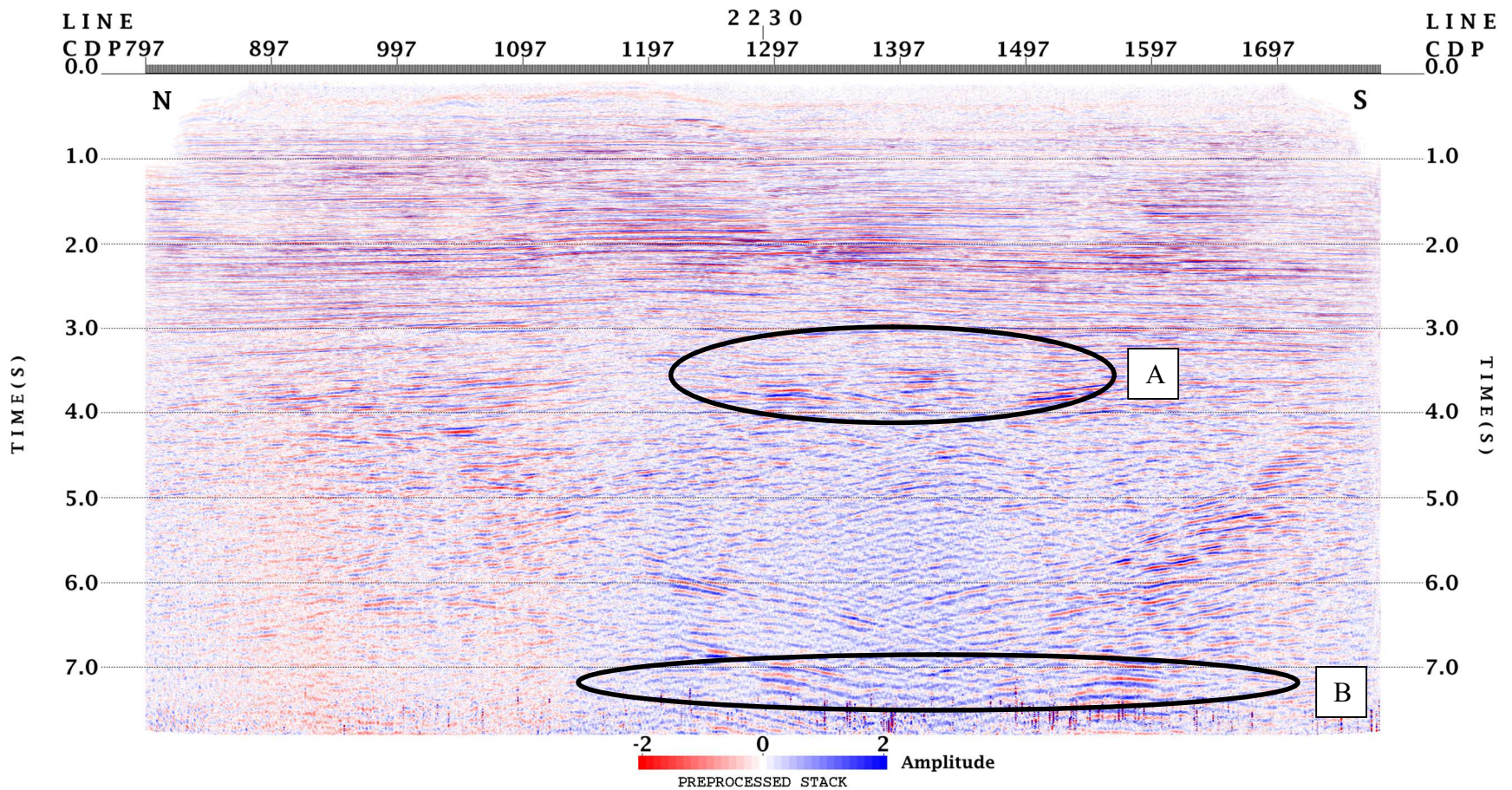


Figure 3.10 Preprocessed EI 26 stack. Due to the complex structures below ~3.5 seconds, there are many event crossovers (A). Pre-stack migration should be able to correct these and improve the reflection events. Bottom of the dataset (B) shows some artifacts, possibly instrument noise during field recording. Overall quality of the section is decent and provides a broad perspective of the subsurface structure.

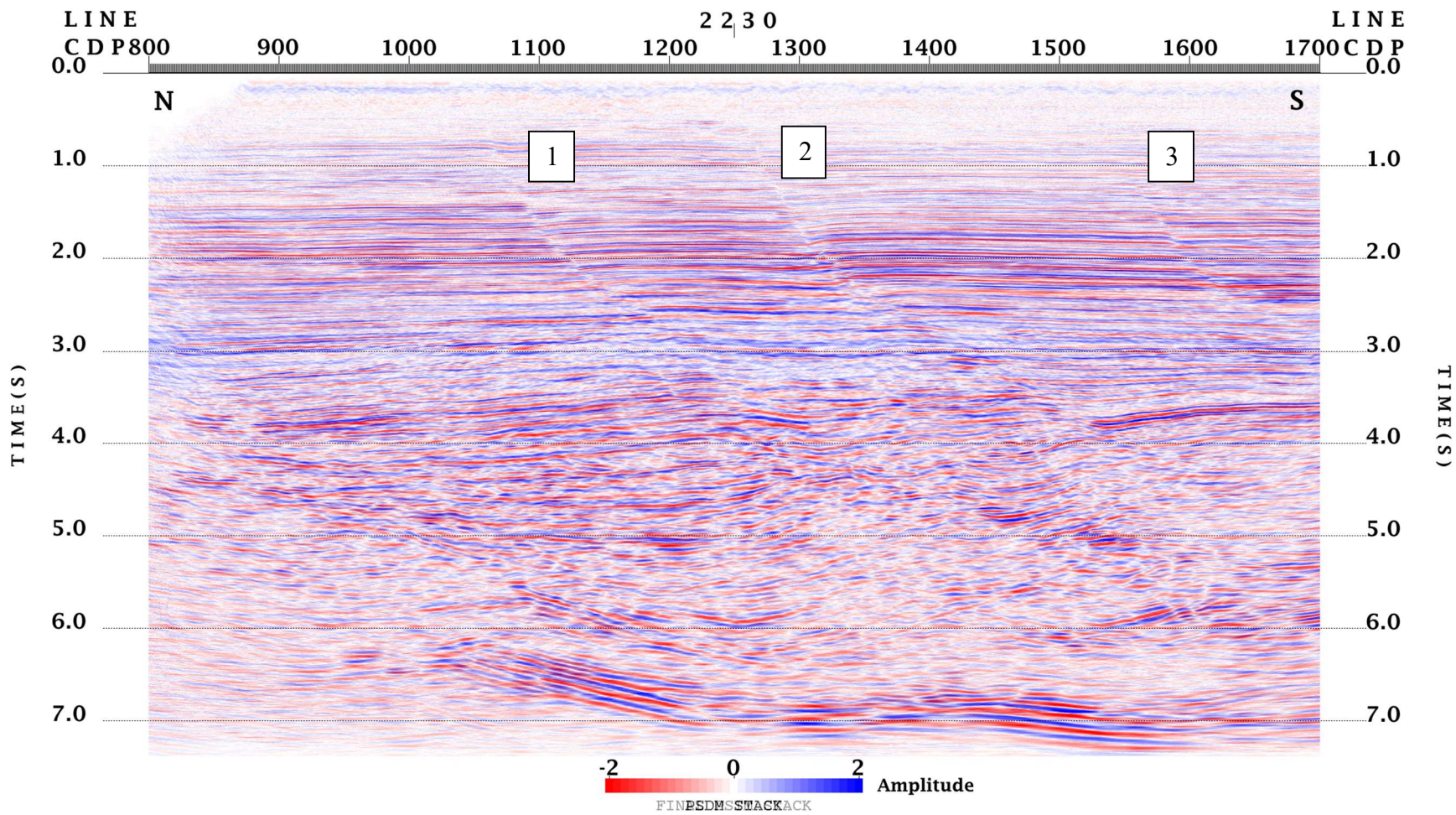


Figure 3.11 PSTM full stack section. Three faults (1), (2), and (3) are now identifiable from the stack.

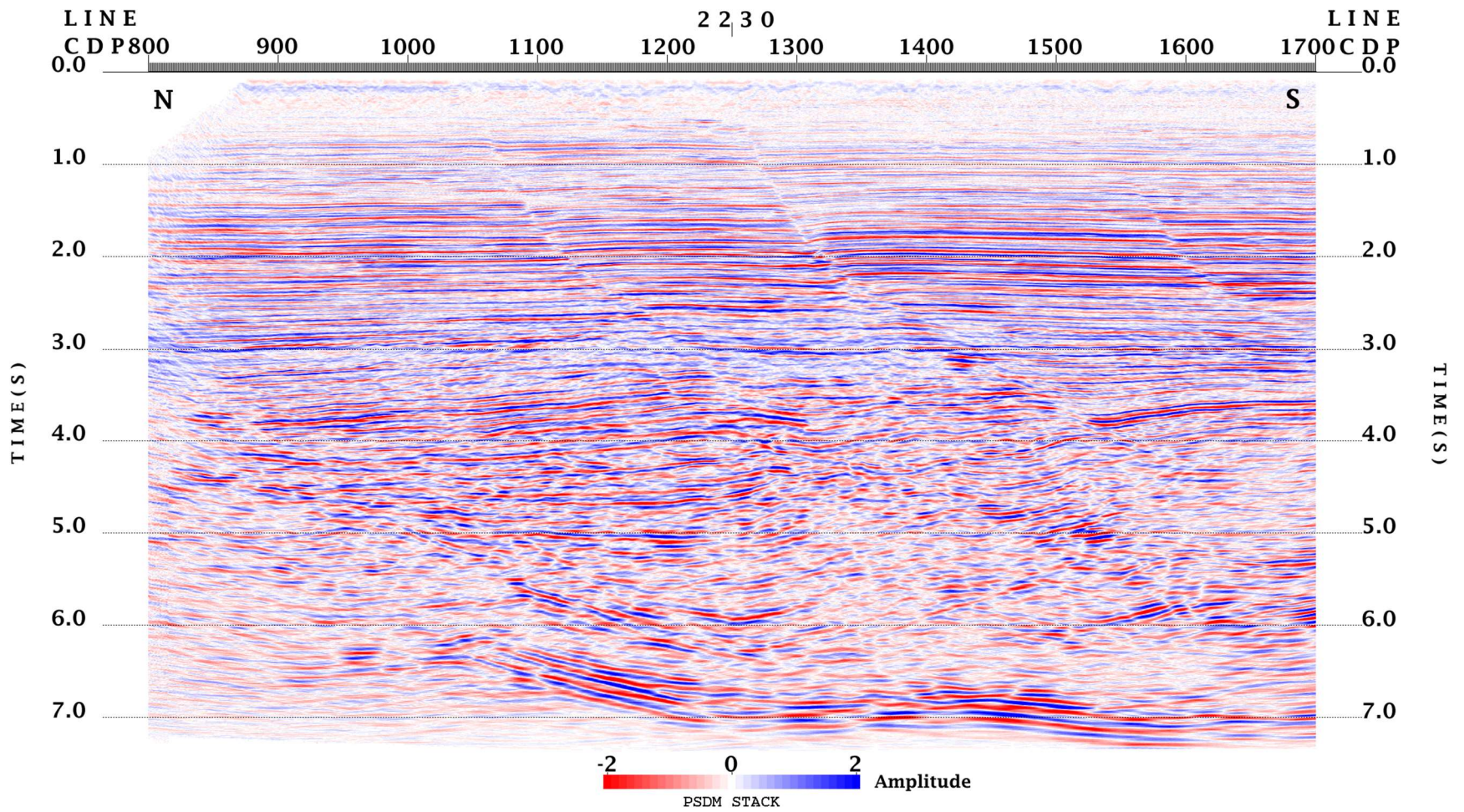


Figure 3.12 PSDM full stack section. Compared to the PSTM, events and signals have been boosted without any significant structural changes. The three faults are now more easily resolved.

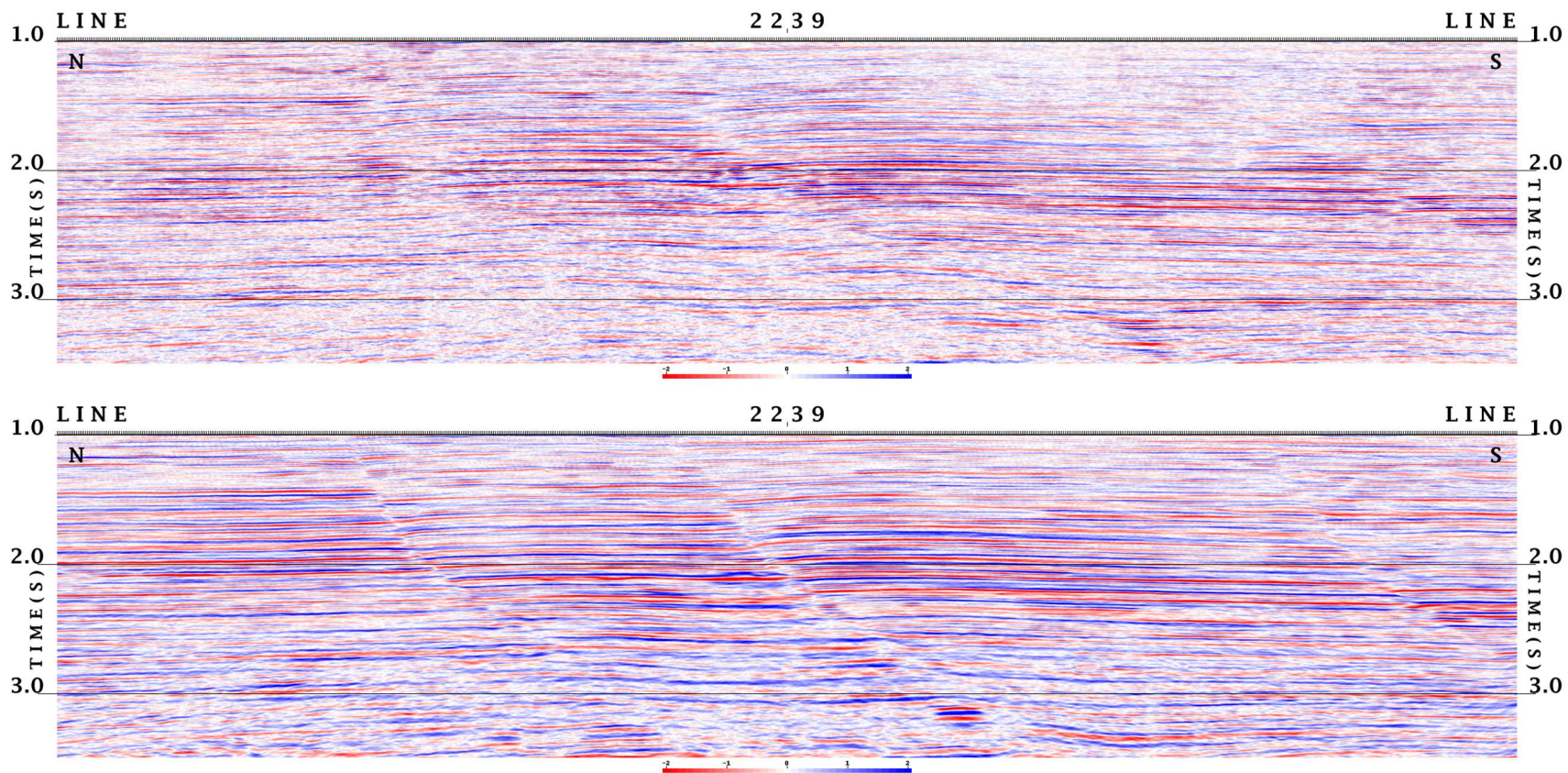


Figure 3.13 Preprocessed stack (top) and PSTM stack (bottom) from 1.0-3.5 seconds. From the PSTM section, three major faults are distinguishable while these are present but obscure and difficult to trace in the preprocessed section.

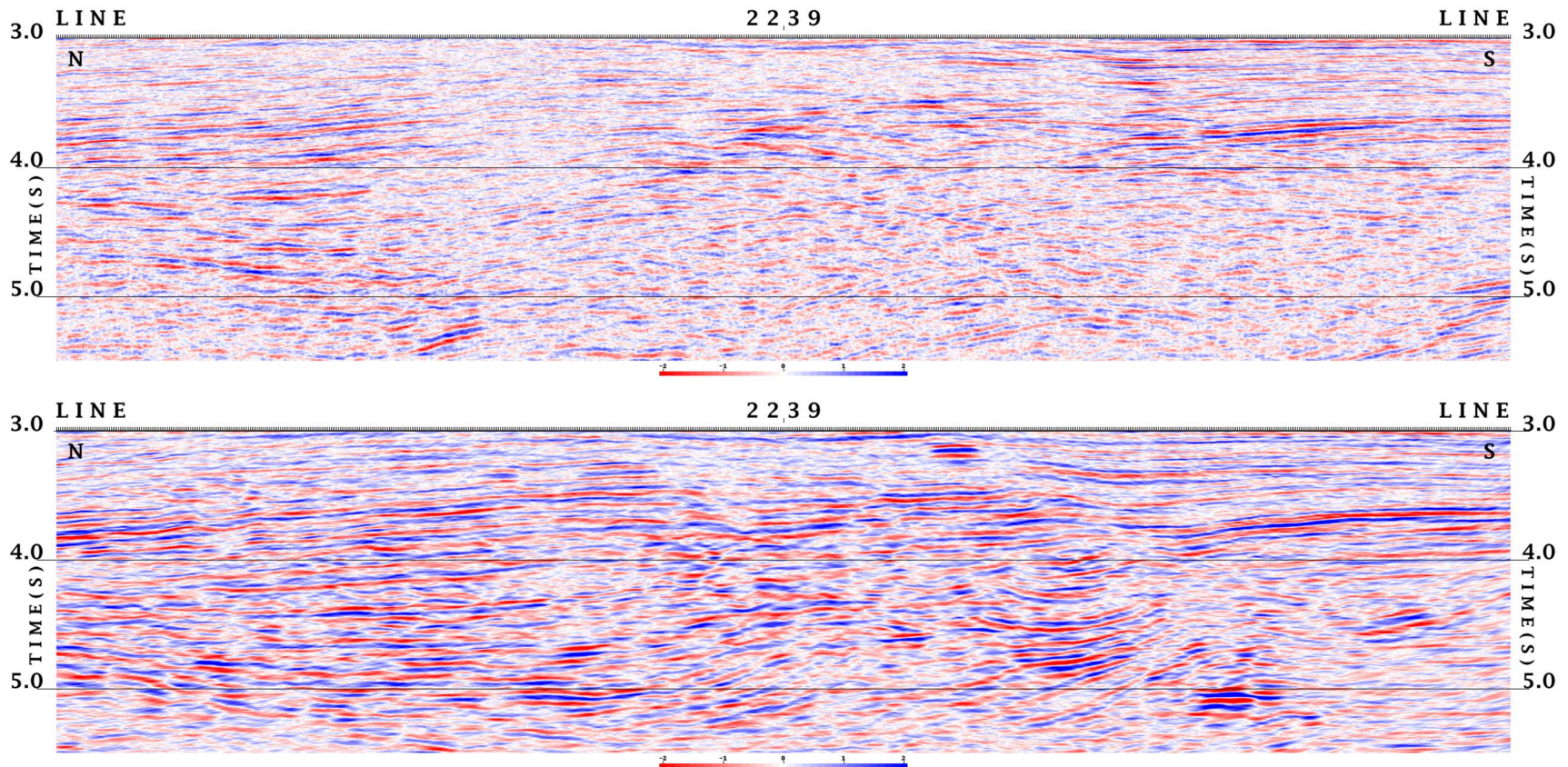


Figure 3.14 Preprocessed stack (top) and PSTM stack (bottom) from 3.0-5.5 seconds. This time interval contains more complex geology and the preprocessed section has poor image quality in this area. After PSTM, amplitudes and continuity across the section is greatly improved, and fault dipping to the south also becomes visible. The preprocessed stack also contains false events known as the “bow-tie effect”, an error caused by reflections from synclines. These have been corrected by migration as well.

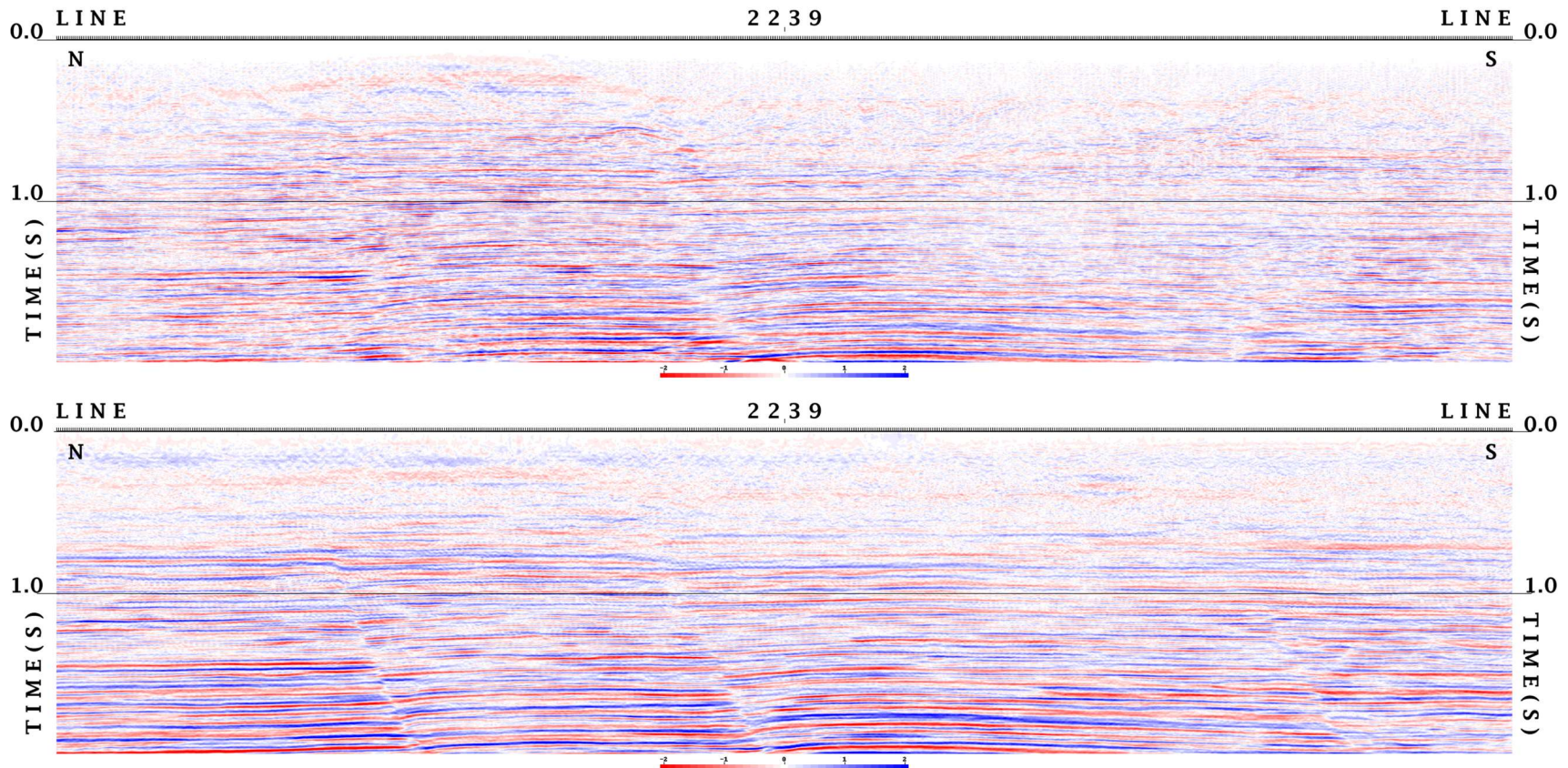


Figure 3.15 Preprocessed stack (top) and PSTM stack (bottom) from 0.0-1.5 seconds. Because the survey was performed via OBC in a very shallow marine environment, the top of the sections does not display the typical ocean bottom reflection seen in marine surveys. Instead it appears more similar to land data. Due to low signal quality from the unconsolidated sediments on the ocean floor, the top of the section is unclear across both sections.

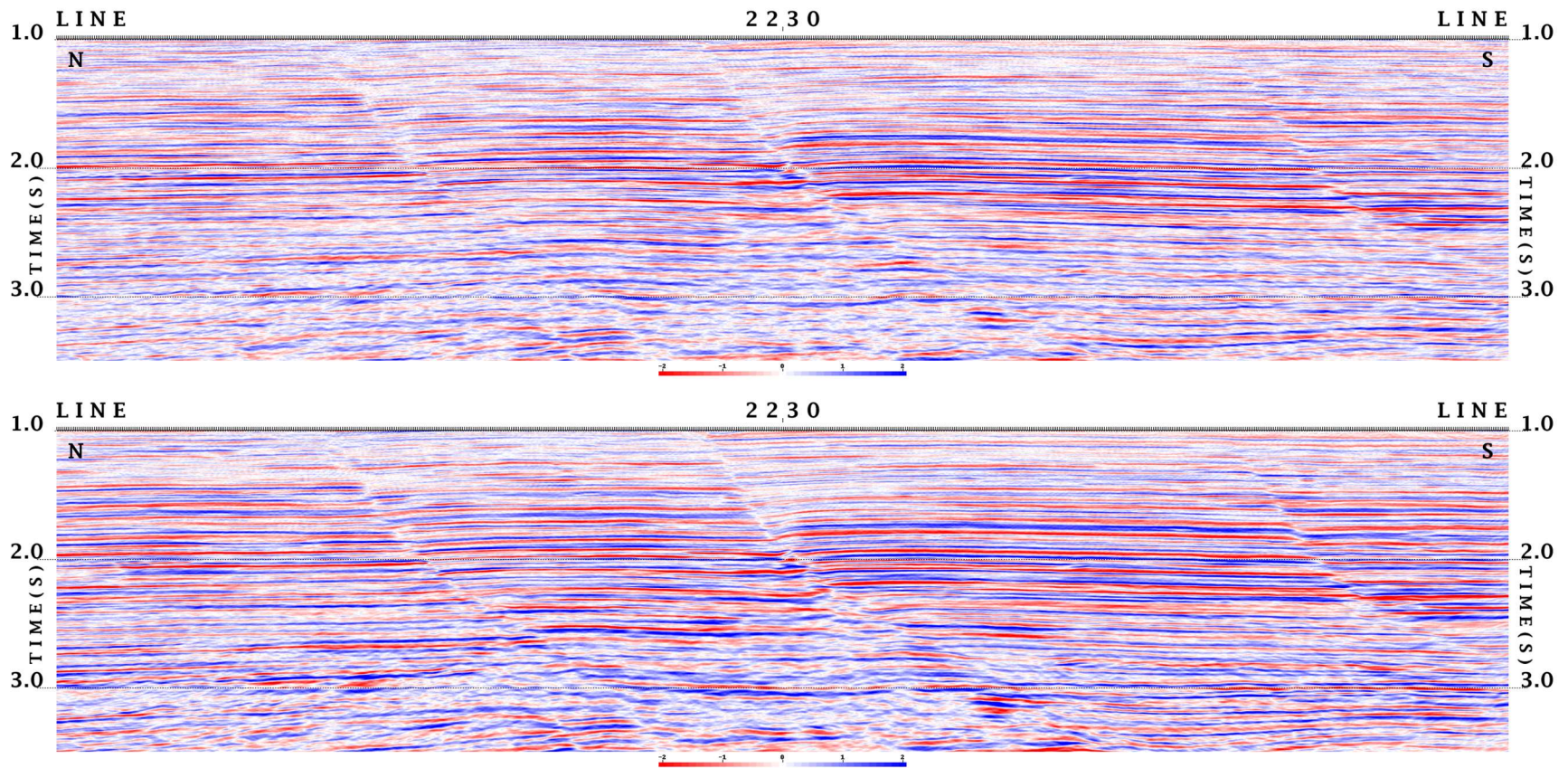


Figure 3.16 PSTM stack (top) and PSDM stack (bottom) from 1.0-3.5 seconds.

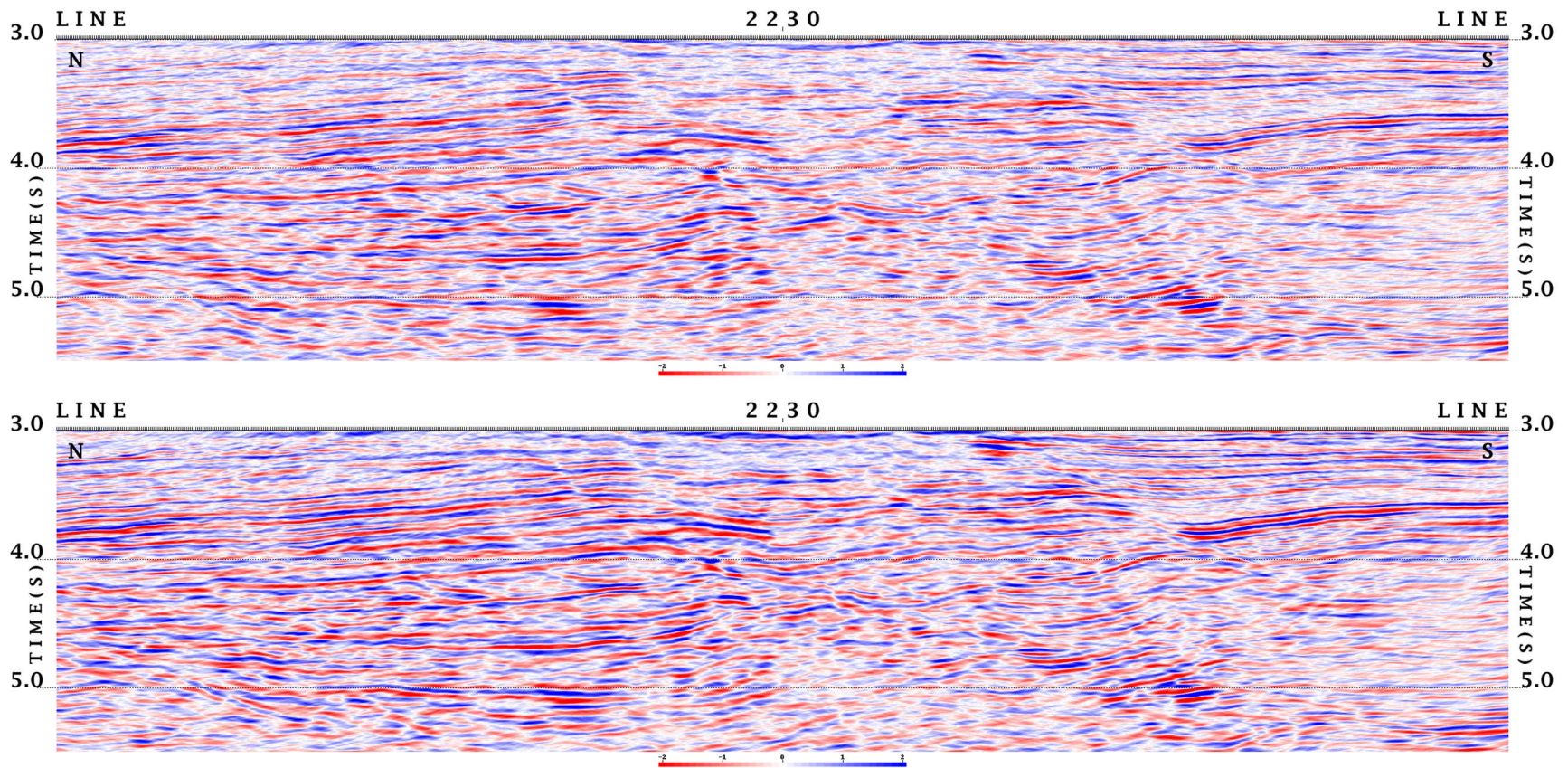


Figure 3.17 PSTM stack (top) and PSDM stack (bottom) from 3.0-5.5 seconds.

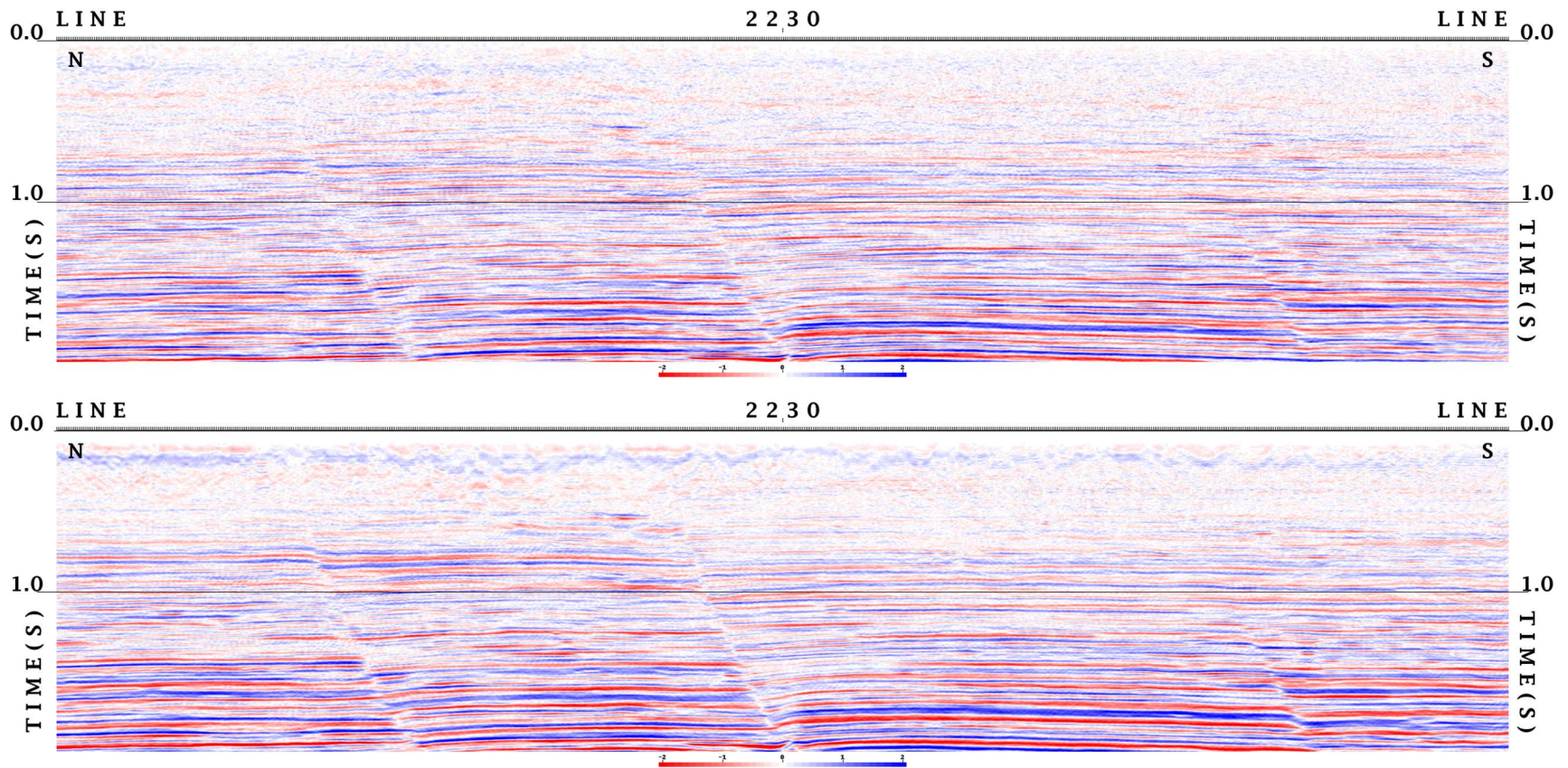


Figure 3.18 PSTM stack (top) and PSDM stack (bottom) from 0.0-1.5 seconds.

3.4 ANGLE GATHERS AND STACKS

Displaying the data as a function of incident angle can be helpful in identifying AVO responses across the dataset. The most obvious response is a sizeable increase in amplitude as the angle increases. Figure 3.19 is the full angle PSTM CDP gather with no angle mutes. Figure 3.20, Figure 3.21, and Figure 3.22 are angle gathers of a PSTM migrated section at 0-15, 15-30, and 30-70 degrees, respectively. Figure 3.23, Figure 3.24, and Figure 3.25 are the stack sections relating to the angle gathers at the same intervals.

From the angle gathers and stacks we observe several factors:

1. Faults are detectable at near, mid, and far angles.
2. The far stack loses some structural information especially at deeper depths, whereas the near and mid angles have higher resolution.
3. The far angle gathers experiences more distortion, likely due to a variety of factors such as NMO stretch and phase changes due to higher reflection angles.
4. When tying the well log and far angle gathers (Figure 3.22), the high percentage sand volume ends at about 9000 feet, which roughly correlates to 3 seconds. This further supports the previously seen estimation through velocity analysis that the onset of abnormal pressure begins at 3 seconds.
5. Reflection amplitude increases from near to mid to far angles, indicating the possibility of a Class II or III AVO anomaly
6. At approximately 1.950 s, a high amplitude is observed between CDPs at approximately 1260-1310 that terminates at a fault. It is bright on all three offset stacks, which is a characteristic of a Class III gas anomaly. The shape, position, and amplitude suggest a gas-saturated interval. This anomaly was just missed with Well 3149.

7. On the other side of the fault from Well 3129, there are several indicators of gas-saturated sands. On all offset stacks, from CDPs 1340-1450 at approximately 2.080 seconds is the downdip termination of an event whose amplitude conforms to structure. On the far-offset stack there is a flat spot associated with this event to suggest a gas-brine interface. In fact, there are numerous flat spots at this CDP location and approximate time interval to suggest multi-pay intervals,
8. In the far stack, the high amplitude between 1.5 – 2.5 seconds corresponds to an interval with a high percentage of clean sands. This analysis is based on the available well control. Because of the high sand percentage, it is unlikely for overpressure to occur in this time interval.
9. In Figure 3.24 and Figure 3.25, there is also evidence that there are three flat spots, indicated by the arrows, and a potential gas/water contact that is now visible, indicating that this area is gas bearing. This also provides two potential drilling locations for gas reservoirs.

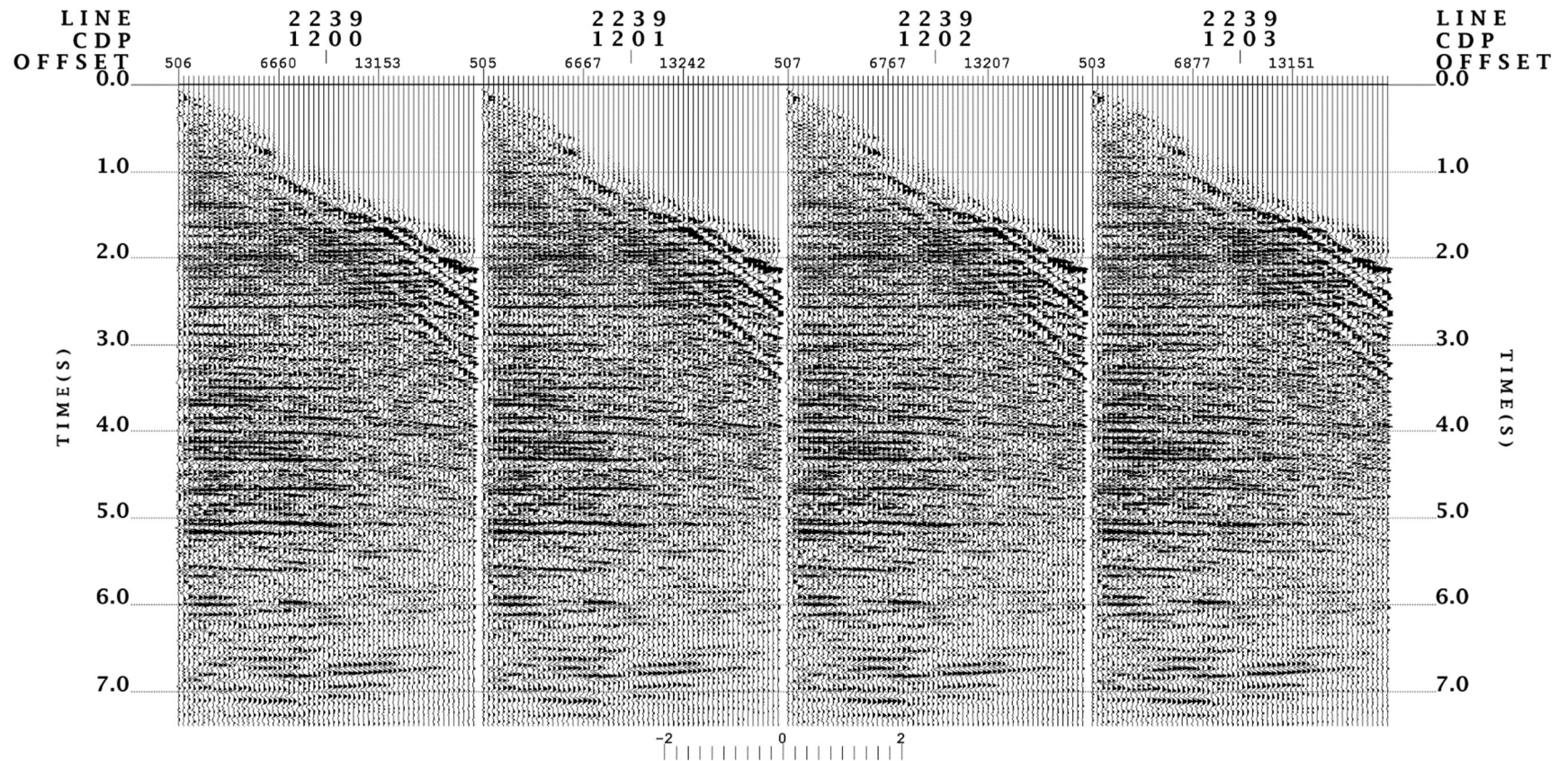


Figure 3.19 PSTM full angle CDP gather

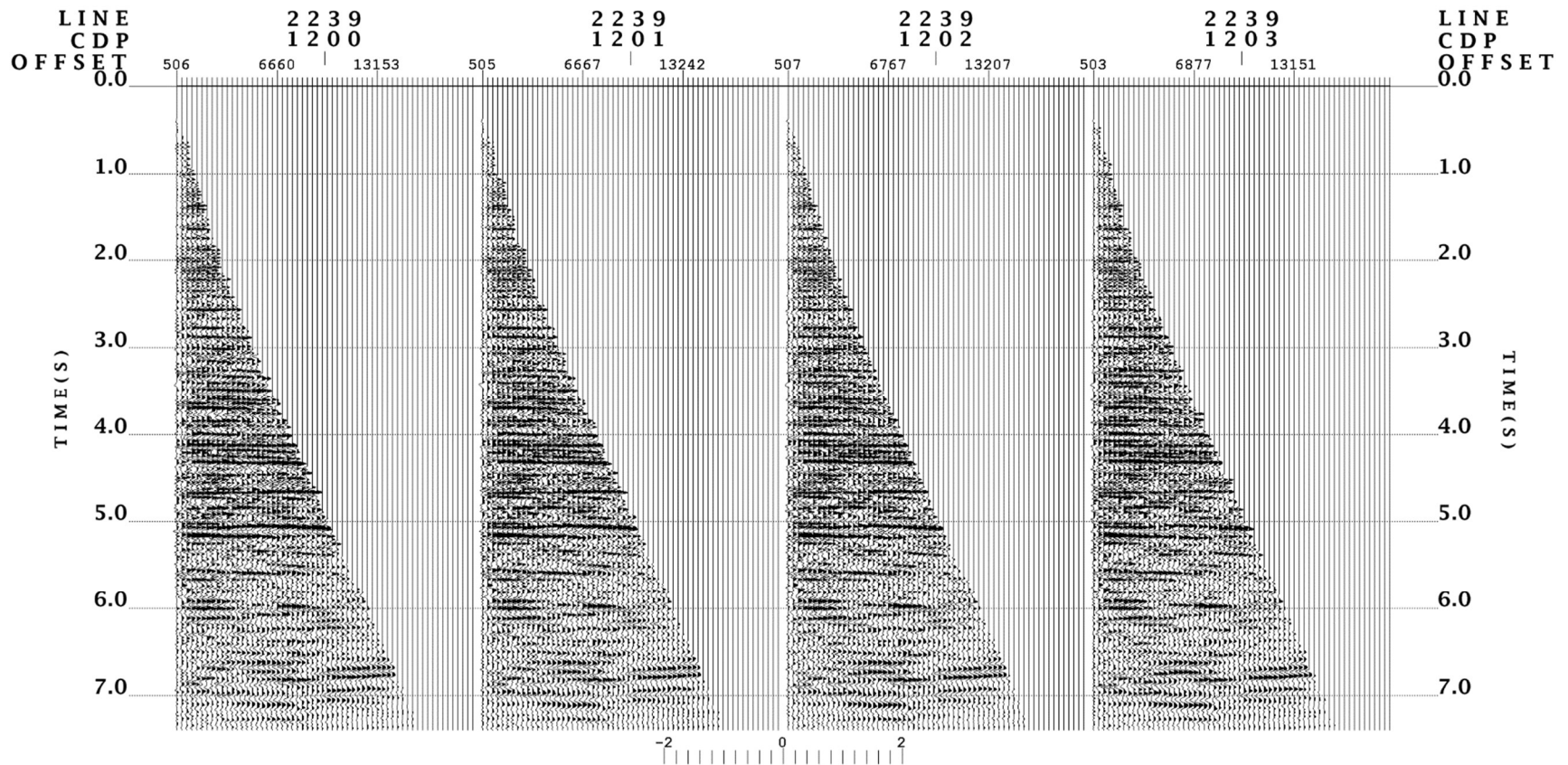


Figure 3.20 PSTM angle gathers from 0 to 15 degrees

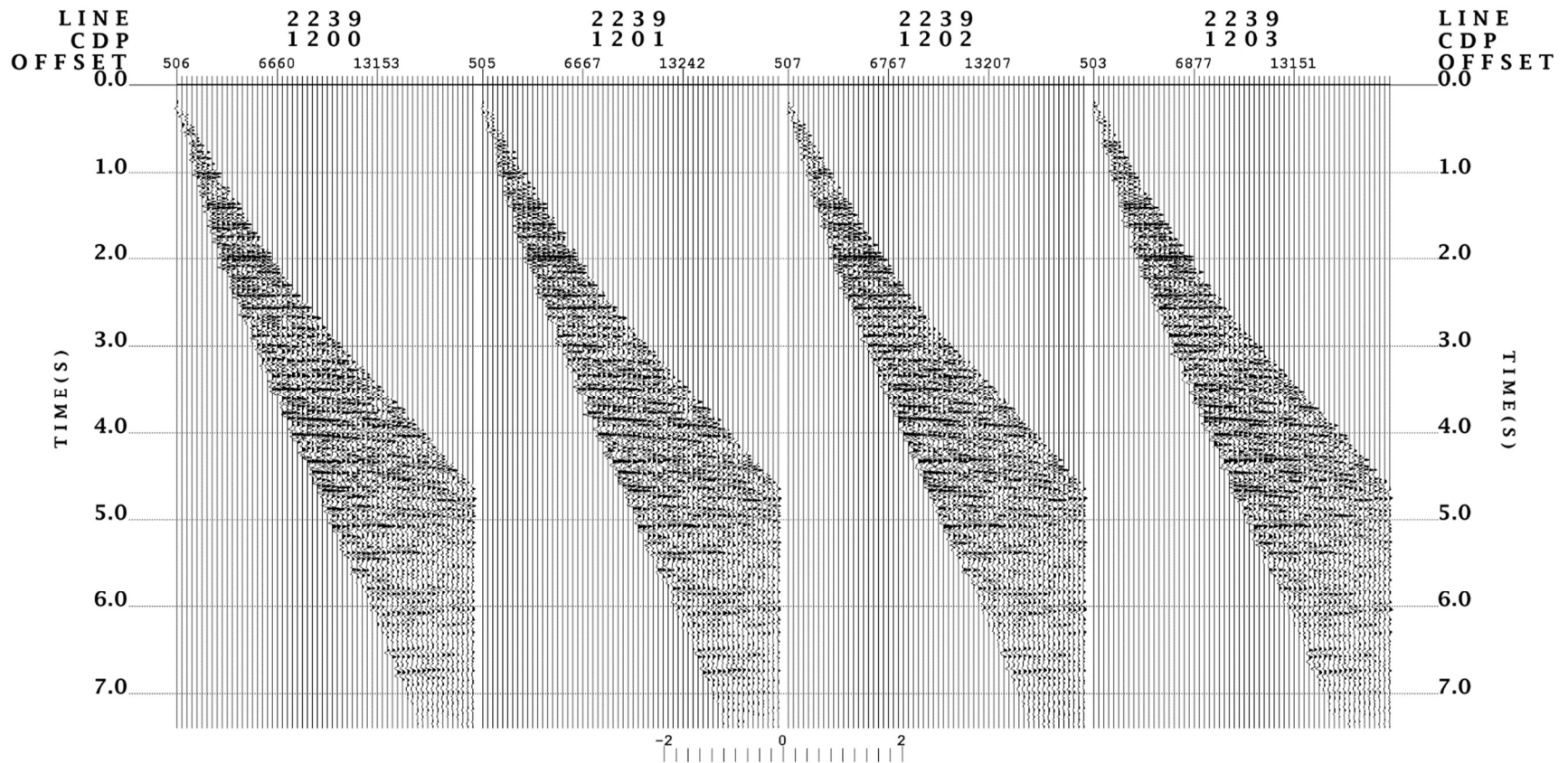


Figure 3.21 PSTM angle gathers from 15 to 30 degrees

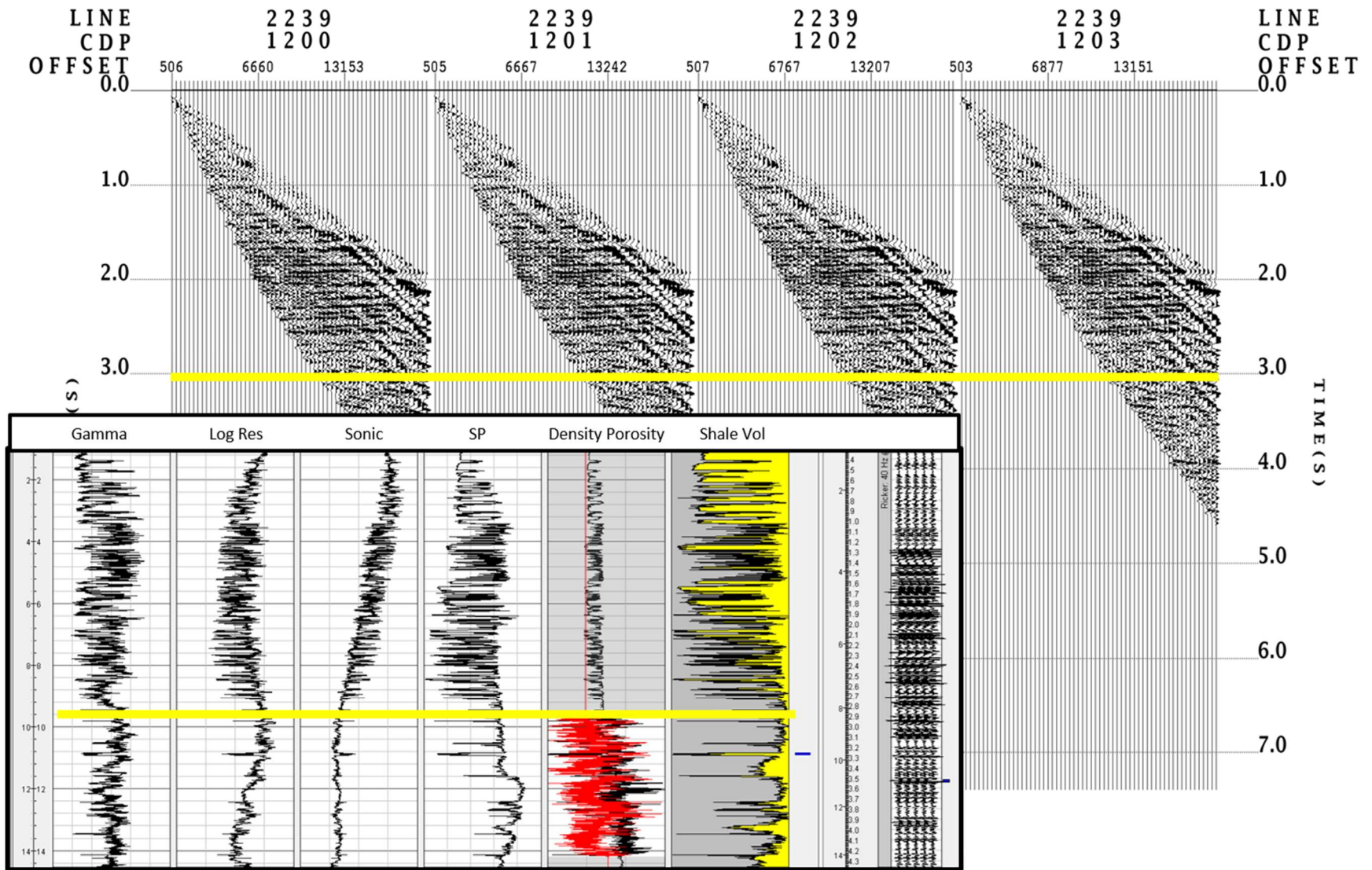


Figure 3.22 PSTM angle gather from 30 to 70 degrees.

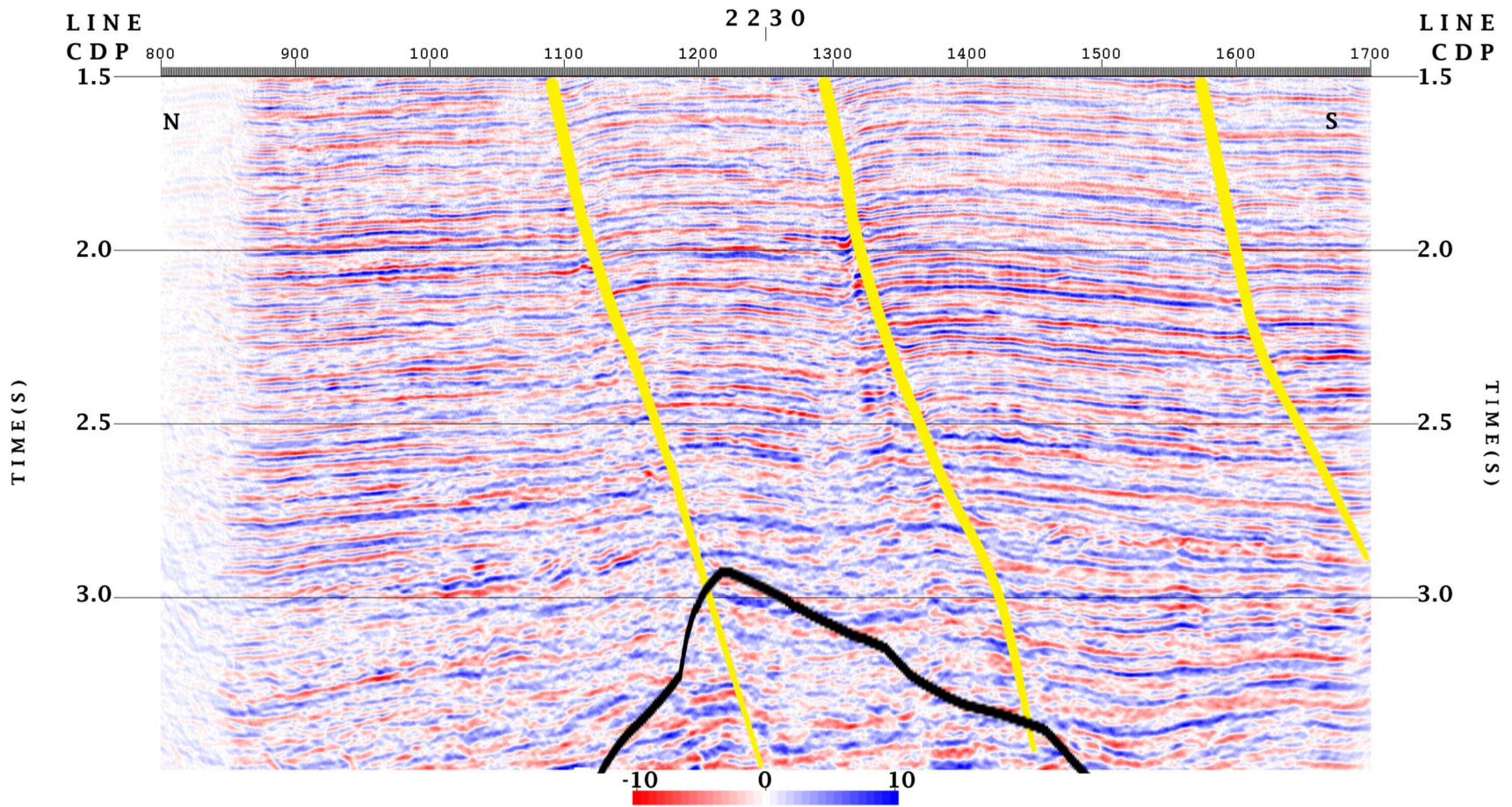


Figure 3.23 PSTM angle stack from 0 to 15 degrees

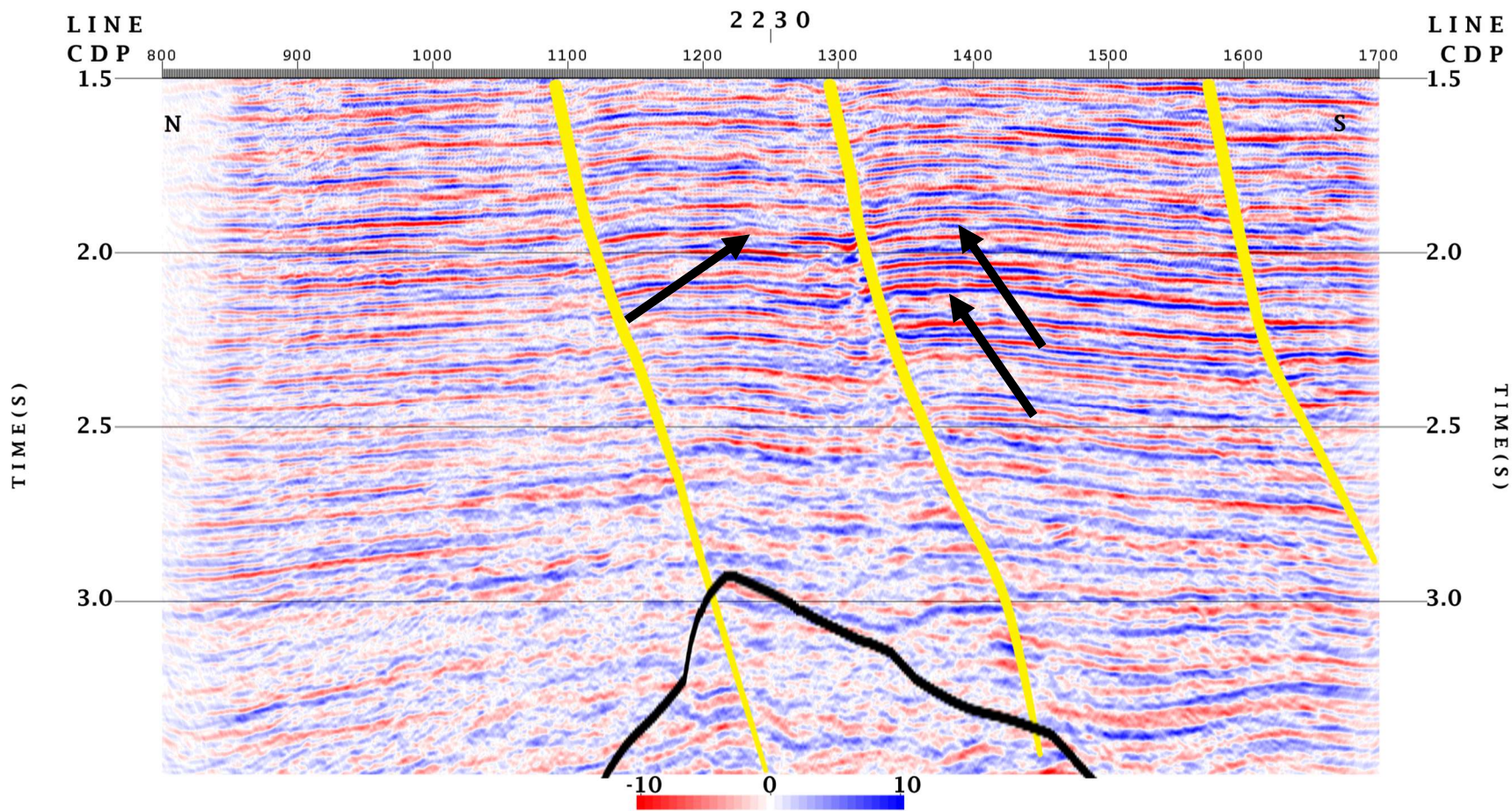


Figure 3.24 PSTM angle stack from 15 to 30 degrees, the arrows indicate flat spots

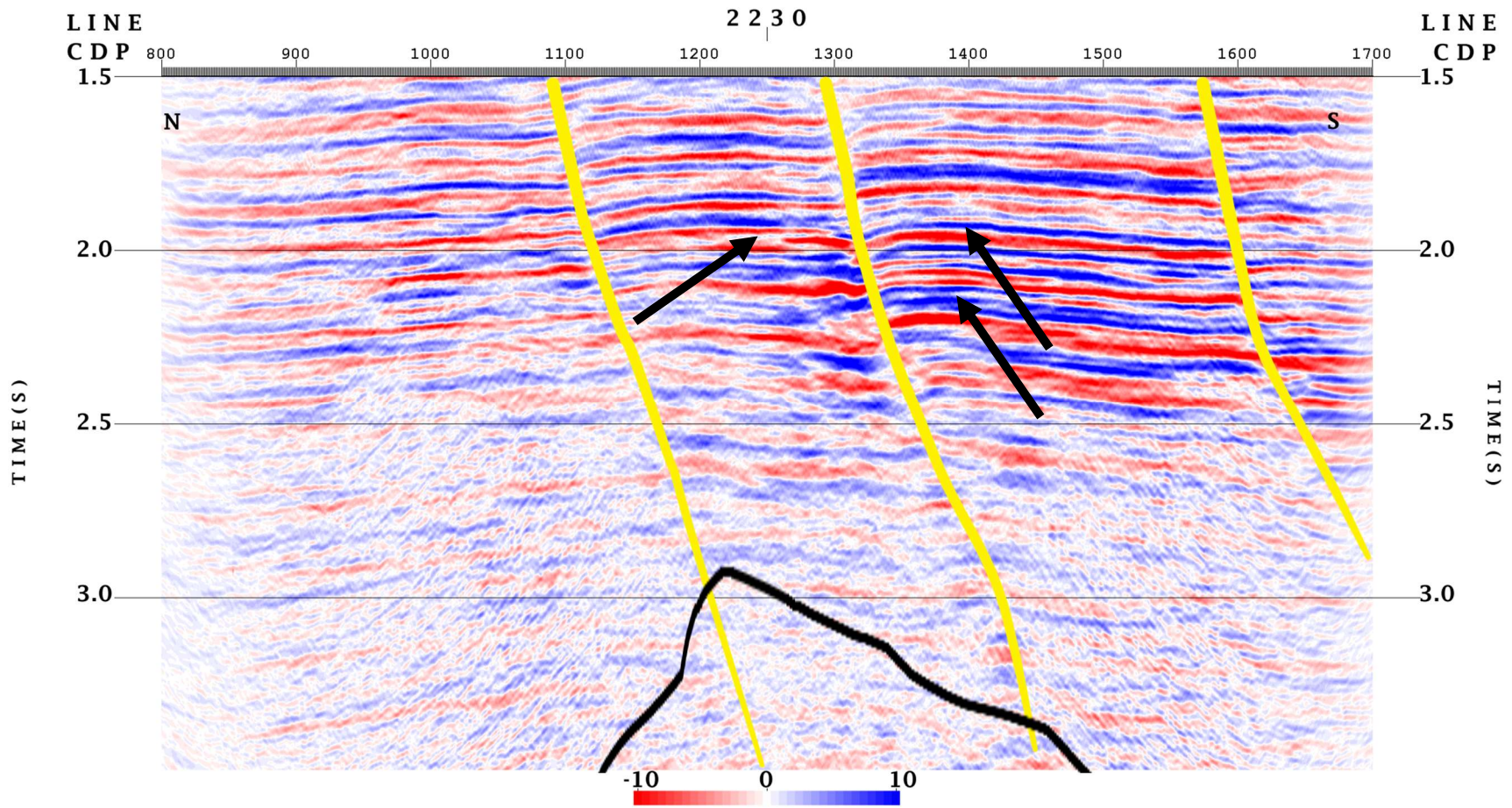


Figure 3.25 PSTM angle stack from 30 to 70 degrees, the arrows indicating flat spots

3.5 FAULT DISCRIMINATION

Faults are an important structural feature both for interpretation and for processing. Clear-cut faulting which is traceable through a stack section can be an indication of a good processing job. A poor processing job would make the fault blurry or even erase faults entirely. For interpreters, faults are prime candidates for consideration as structural traps for hydrocarbons. As depicted in Figure 3.26, there are three major faults dipping towards the southern direction. The layers between these faults are bounded on both sides by faulting, which could prevent or allow hydrocarbons to leak. Figure 3.27 shows a time slice through the PSTM stack section at 1.9 seconds with the same faults overlaid on top, which provides an overhead view of the faults' placement and orientation. Figure 3.28 shows a deeper time slice at 5.8 seconds, which indicates the presence of a synclinal structure. However, this is much deeper than our target zone.

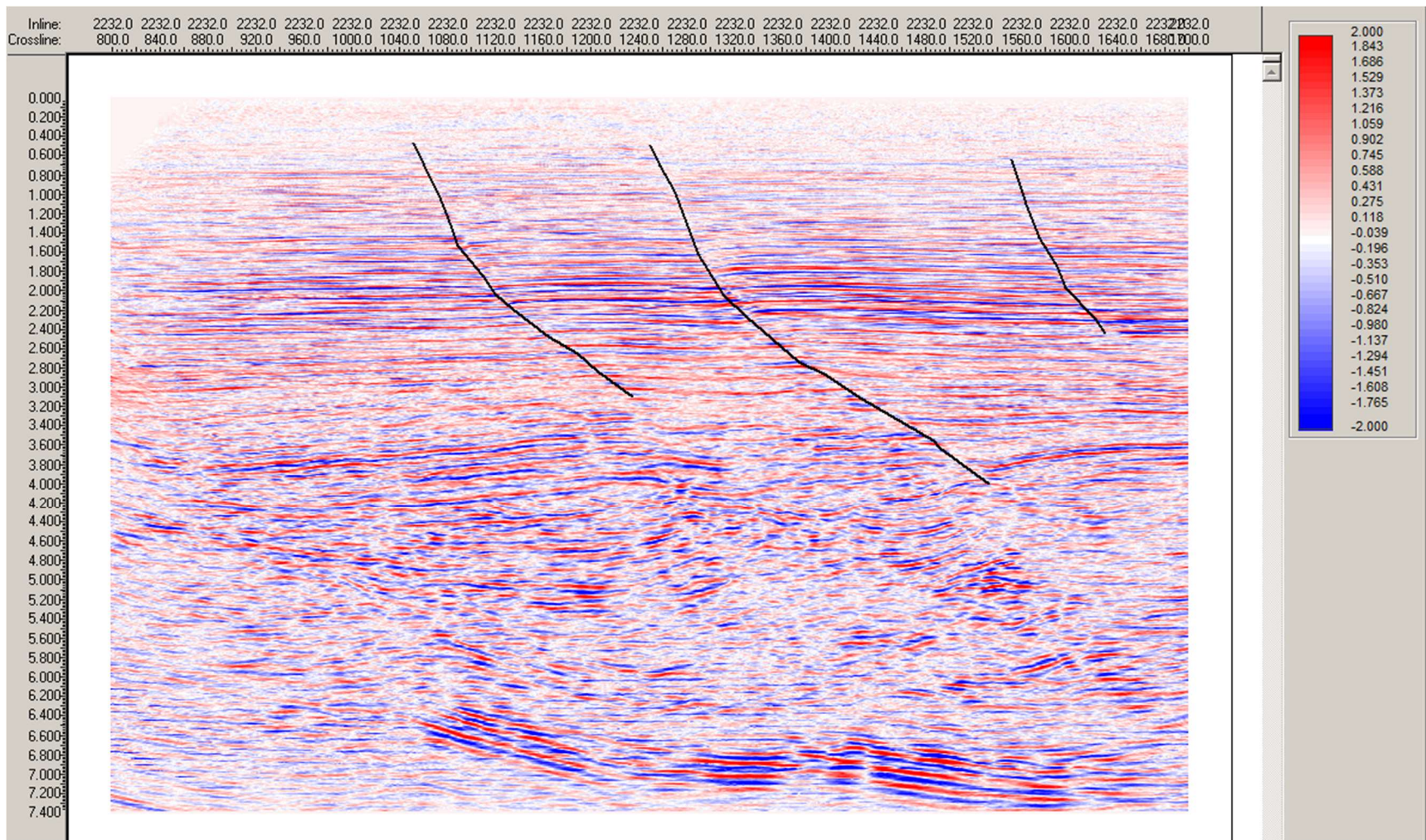


Figure 3.26 PSTM stack section with interpreted fault lines in black.

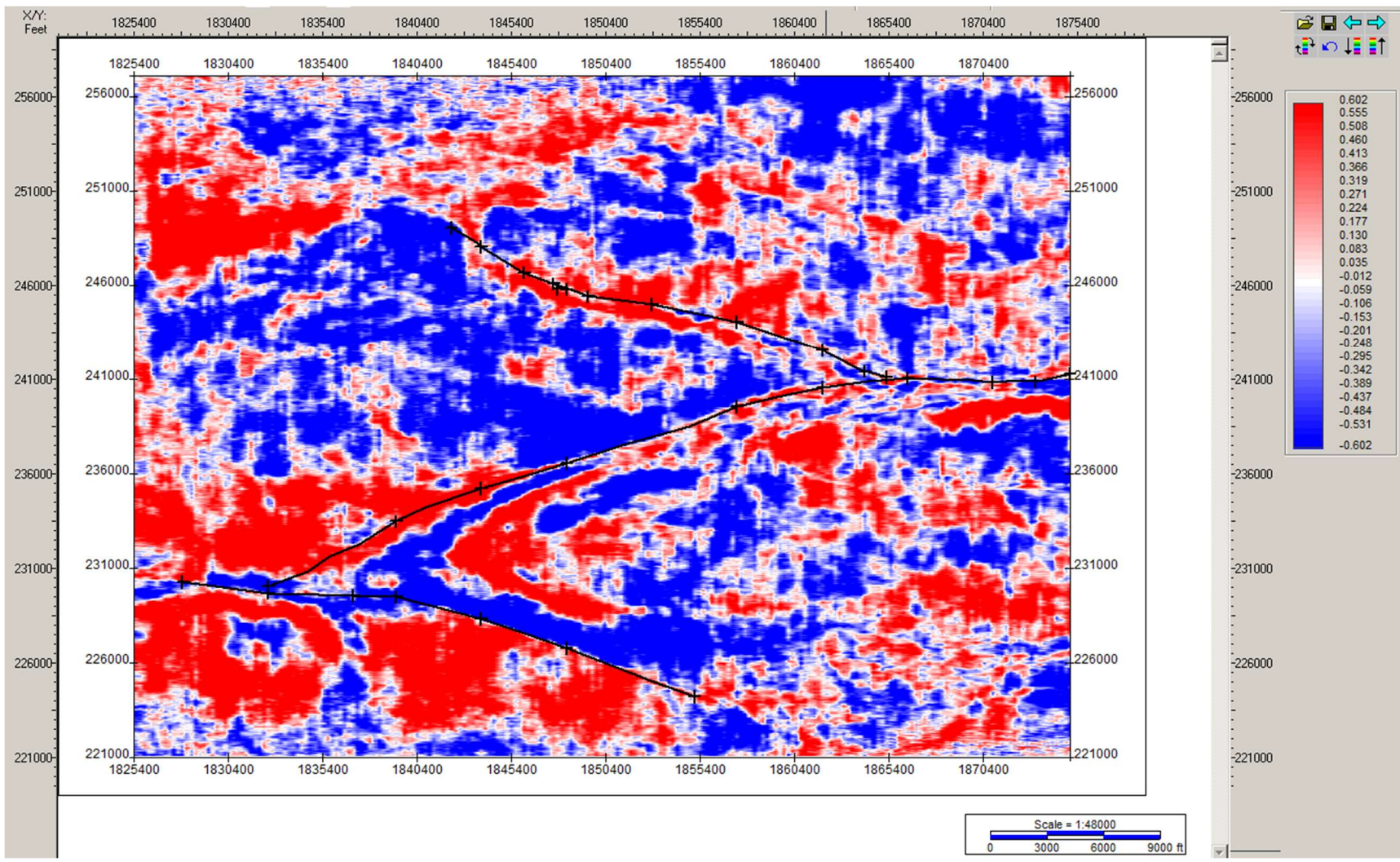


Figure 3.27 Time slice through the 3D stack volume at 1.9 seconds with interpreted faults in black.

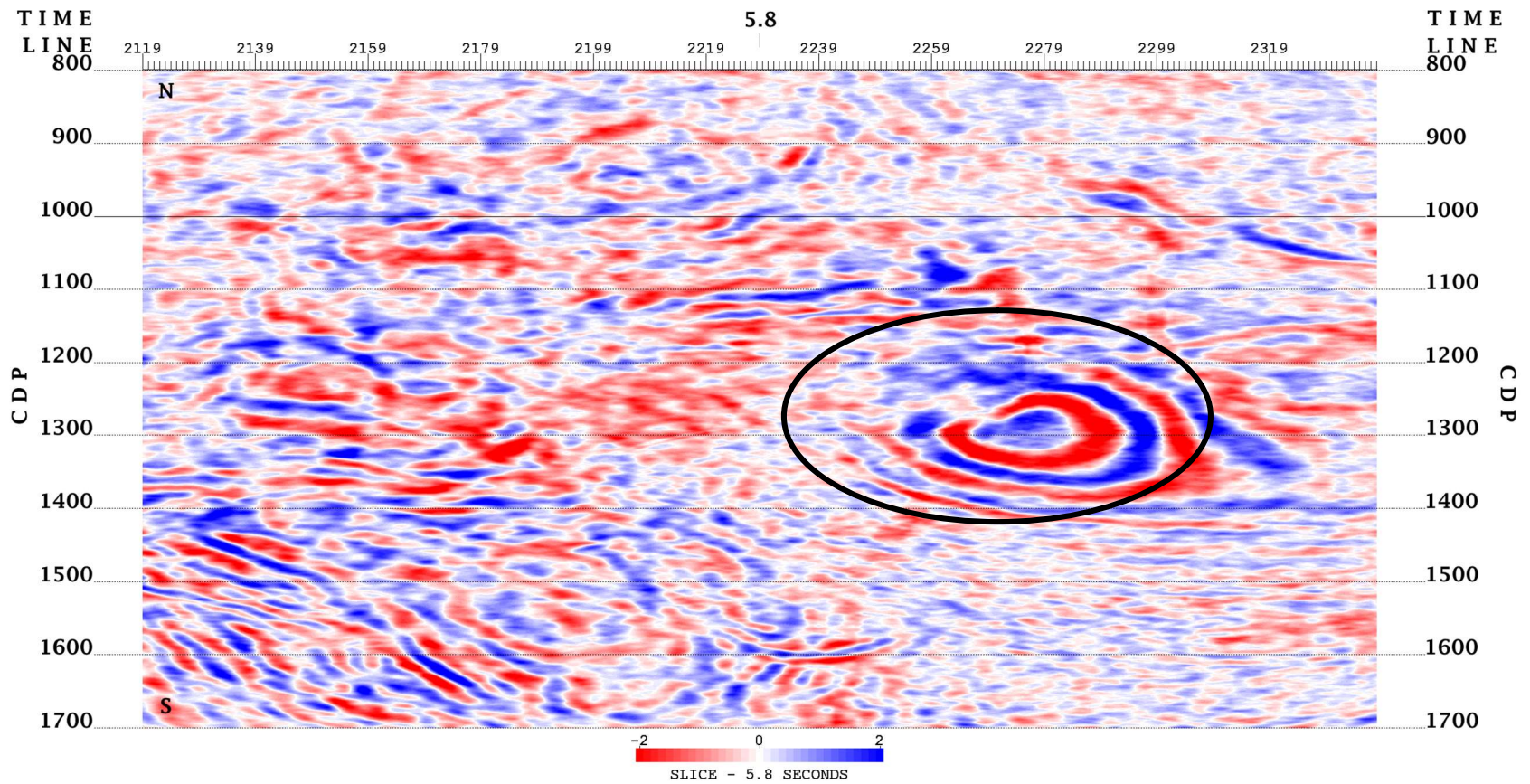


Figure 3.28 Time slice through the PSTM 3D volume at 5.8 seconds depth. A large syncline structure is observable and outlined with a black circle.

3.6 AVO PROCESSING OUTPUTS

Because the (A*B) AVO attribute enhances Class III AVO responses and makes them appear as bright spots, these should be visually apparent on an A*B section. The AVO attribute product A*B is shown in Figure 3.29 with Well 3149's location. There is a positive Class III hydrocarbon response (high amplitude, blue) around 2.0 and 2.25 seconds, which is consistent with the previous areas of interest indicated in the angle stacks. Particularly interesting is that the positive response is cut off on either side by two faults, strongly indicating the presence of a stratigraphic hydrocarbon trap. With these numerous hydrocarbon indicators, the prospect between CDP 1340-1450 has a low risk of failure. As was indicated in the angle stacks, the same flat spots that were visible there can also be seen here.

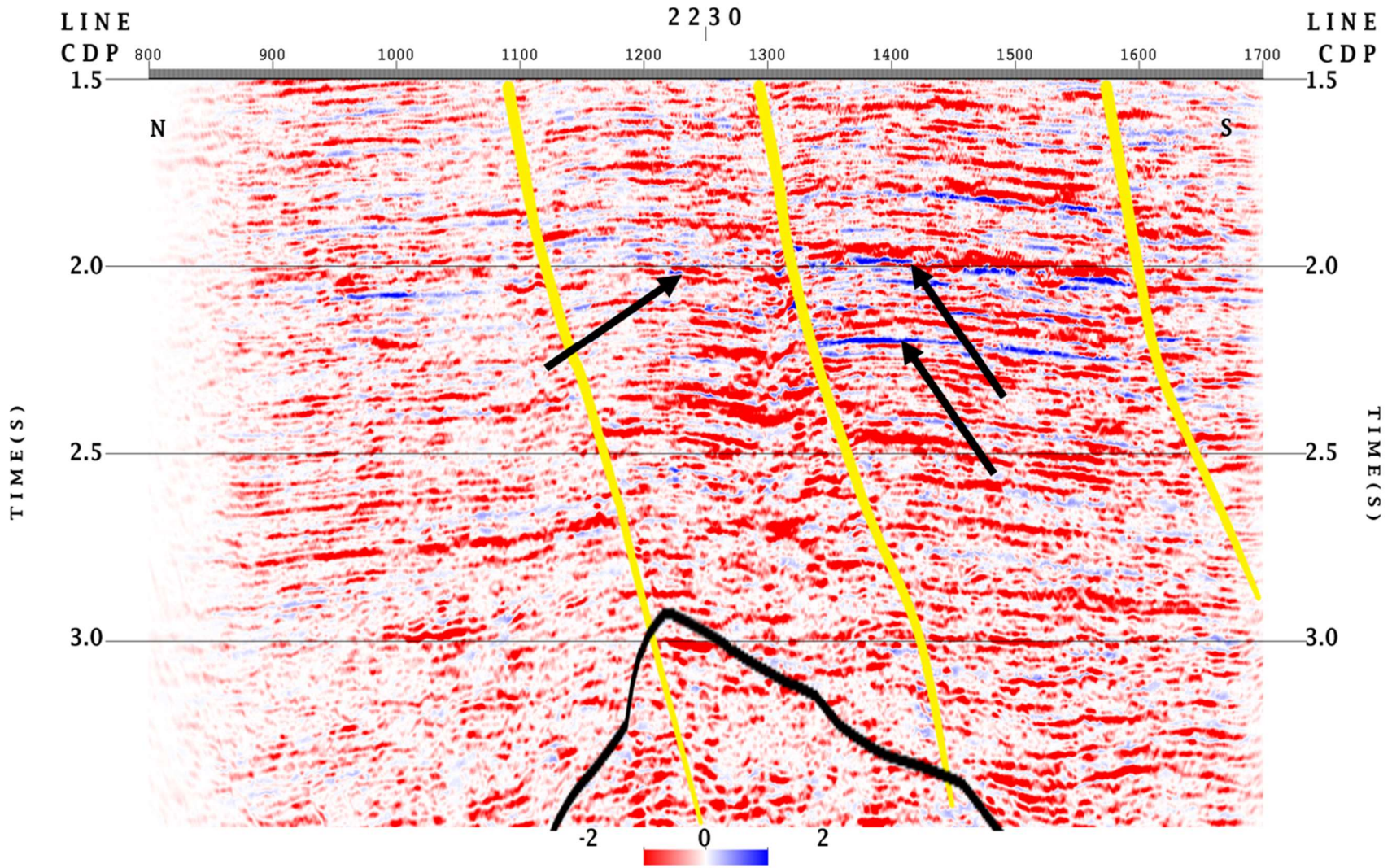


Figure 3.29 Well 3149 AVO (A*B) response

3.7 PORE PRESSURE PROCESSING OUTPUTS

Using the final velocity field picked from the time migrated section, Eaton's and Bowers' method from Equations 1.12 and 1.13 are used to estimate the pore-pressure field. Figure 3.30 displays the Bower's method PPG field while Figure 3.31 show Eaton's method PPG field. Bowers' method indicates a high pore pressure trend along the middle of the survey and also in particular, an anomalous high-pressure zone around ~15,000 feet. Both Eaton and Bowers' method exhibit an increase in pore pressure trend towards the center of the survey however the pressure anomaly is particularly pronounced from Bowers' method in Figure 3.30. From Bowers (1995), the Bowers' method specifically accounts for the loading and unloading effects typically seen in the Gulf of Mexico (Wang and Wang 2015). While Bowers' method uses effective stress, Eaton's method uses effective stress gradient which may follow the pore pressure trend in the Gulf of Mexico less accurately.

Based on the pore pressure outputs, the results are meant to be representative of broad pore pressure trends based on the seismic velocity field. Seismic attributes between CDP 1340~1450 indicates potential gas reservoirs on the downthrown side of the high pore-pressure fault block. This suggests the high pressure zone forced the migration of any hydrocarbon reservoirs into the fault planes to migrate upwards until a structural sand trap was found.

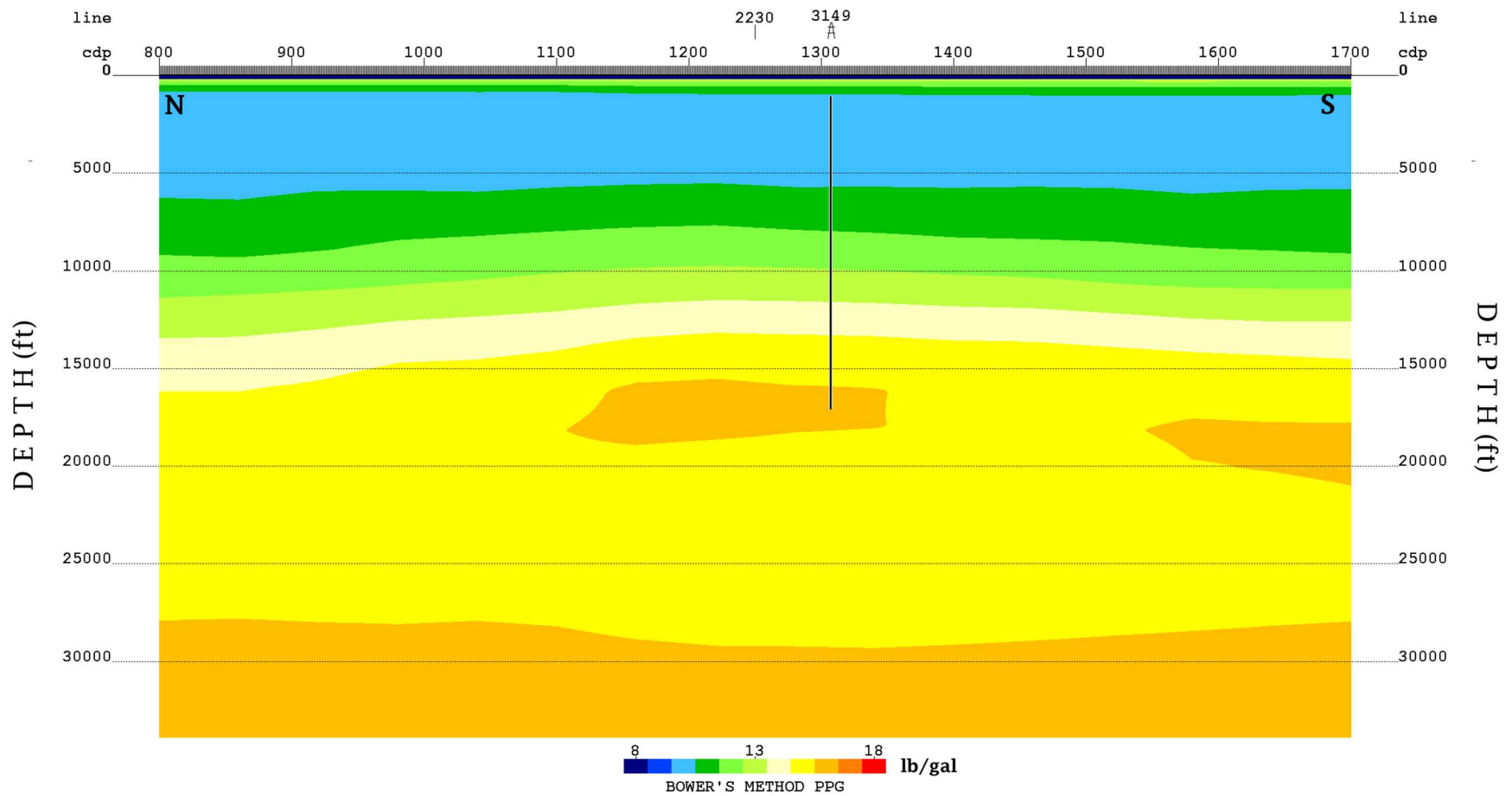


Figure 3.30 Bower's Method - Well 3149 pore pressure gradient field

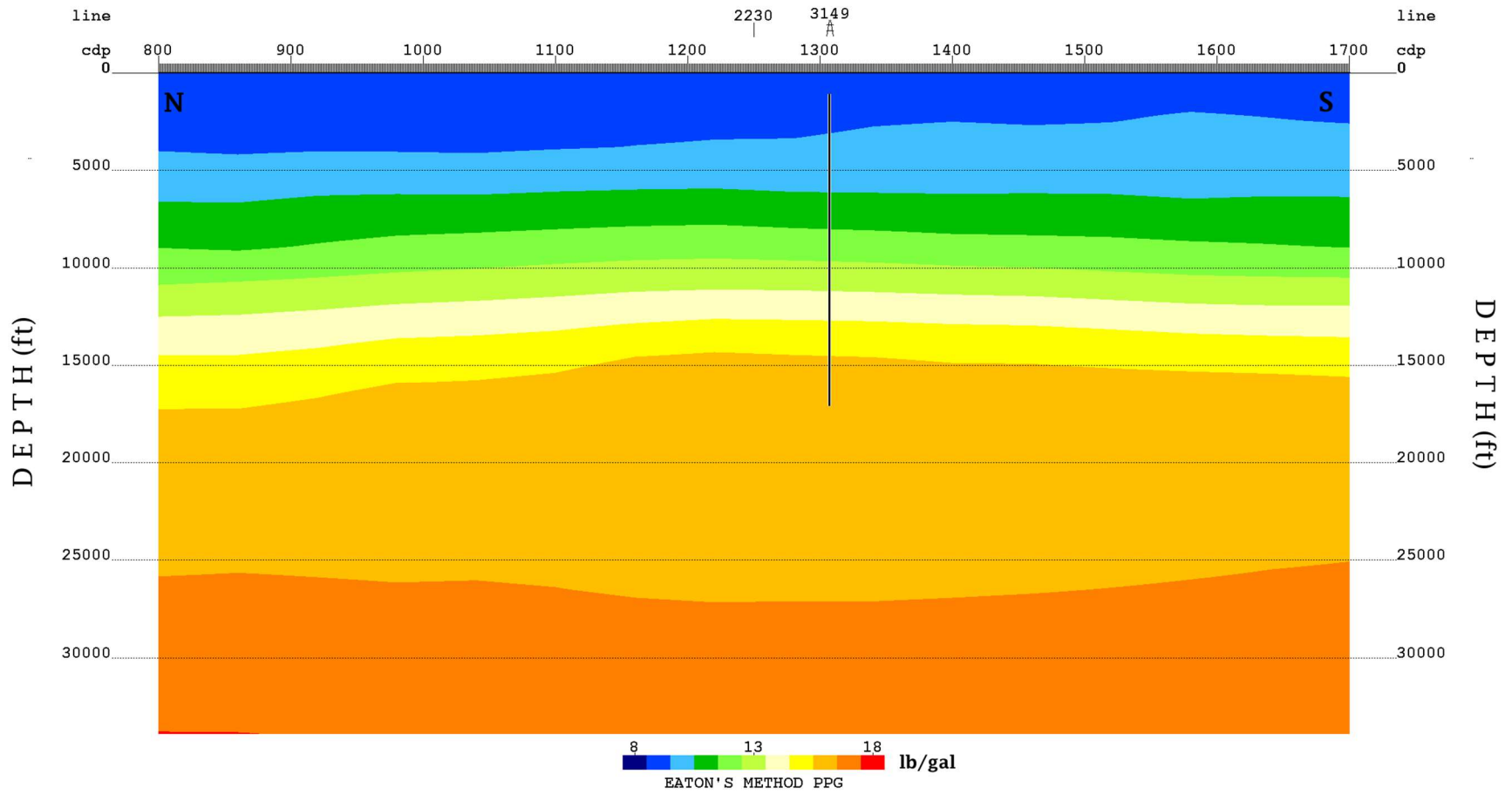


Figure 3.31 Eaton's Method - Well 3149 pore pressure gradient field

3.8 COMPILING THE RESULTS

Four wells with promising suites of well-log curves were chosen for AVO and well-tie analyses (Figure 3.32). Unfortunately, the majority of the available wells are located along the edges of the seismic survey where there is less fold, and the only well near the center is Well 3149. Well 3149 is missing sonic log information at our target depth, so conditions are less than ideal. However, by estimating the sonic log from the resistivity log, a 1D synthetic was generated from Well 3149 and tied to the seismic data as shown in Figure 3.33 by stretching and squeezing the 1D synthetic. Overall, the 1D synthetic has limited correlation with the seismic data. The well synthetic was also overlaid on top of the AVO A*B attribute section, and the strong positive response does seem to correspond with the well around the 2.0 second mark. However due to the missing sonic information, this cannot be considered a reliable well tie result.

Figure 3.34, Figure 3.35, and Figure 3.36 tie the low velocity zone relative to the fault locations, AVO A*B section, and the full stack section. The low velocity zone is correlated by the structural continuity of reflections in Figure 3.36 and is structurally bound within a fault block. The seismic attributes between CDP 1340-1450 indicated potential gas reservoirs on the downthrown side of the high pore-pressure fault block. This suggests the high pressure zone forced the migration of any hydrocarbon reservoirs into the fault planes to migrate upwards until a structural sand trap was found. This is another example of interpretation integration to lower the exploration risk.

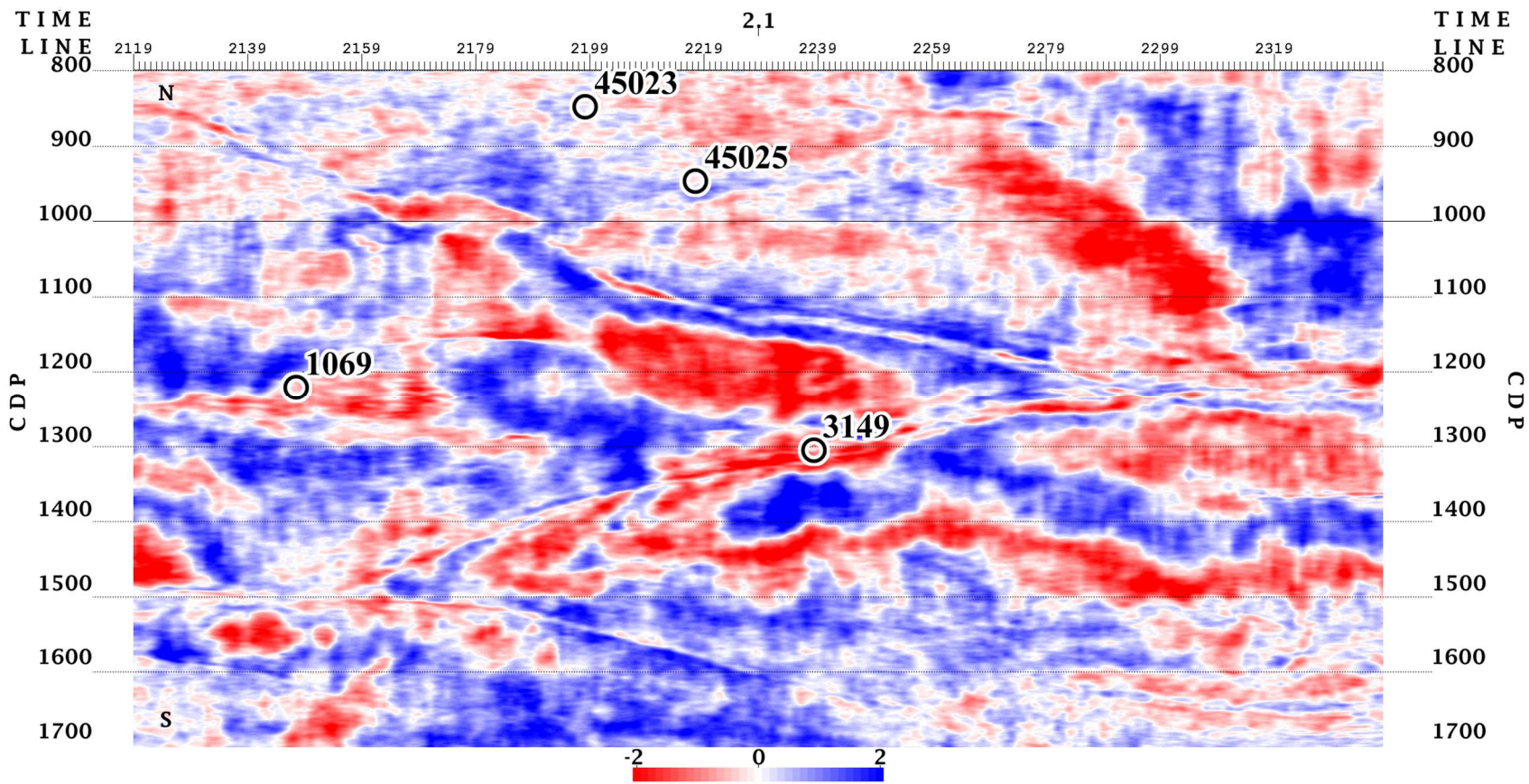


Figure 3.32 Time slice through PSTM stack section at 2.1 seconds with well locations marked.

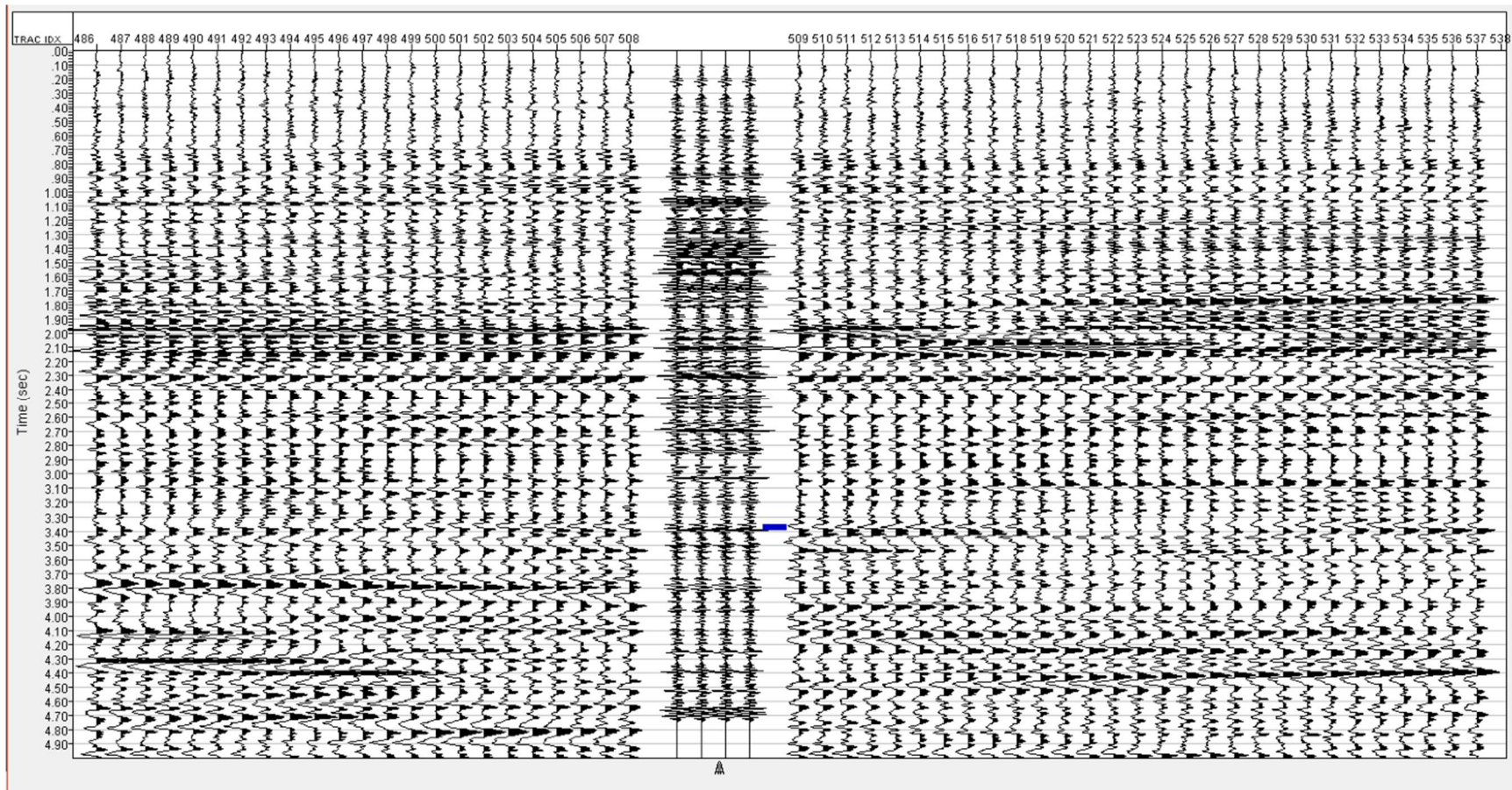


Figure 3.33 Well 3149 well-tie with processed seismic data from Inline 2230.

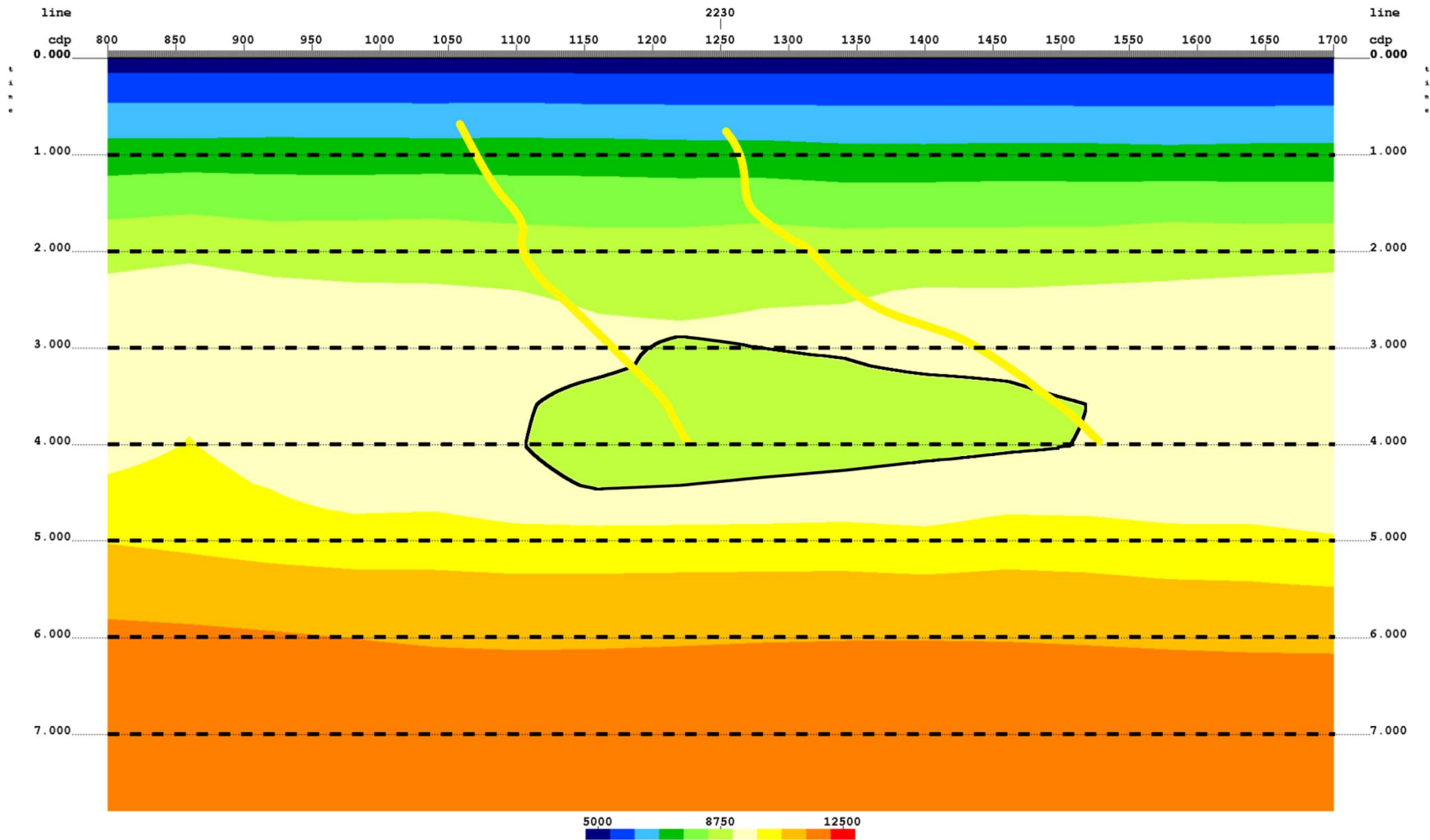


Figure 3.34 Velocity field tie with interpreted fault locations. Low velocity zone outlined in black.

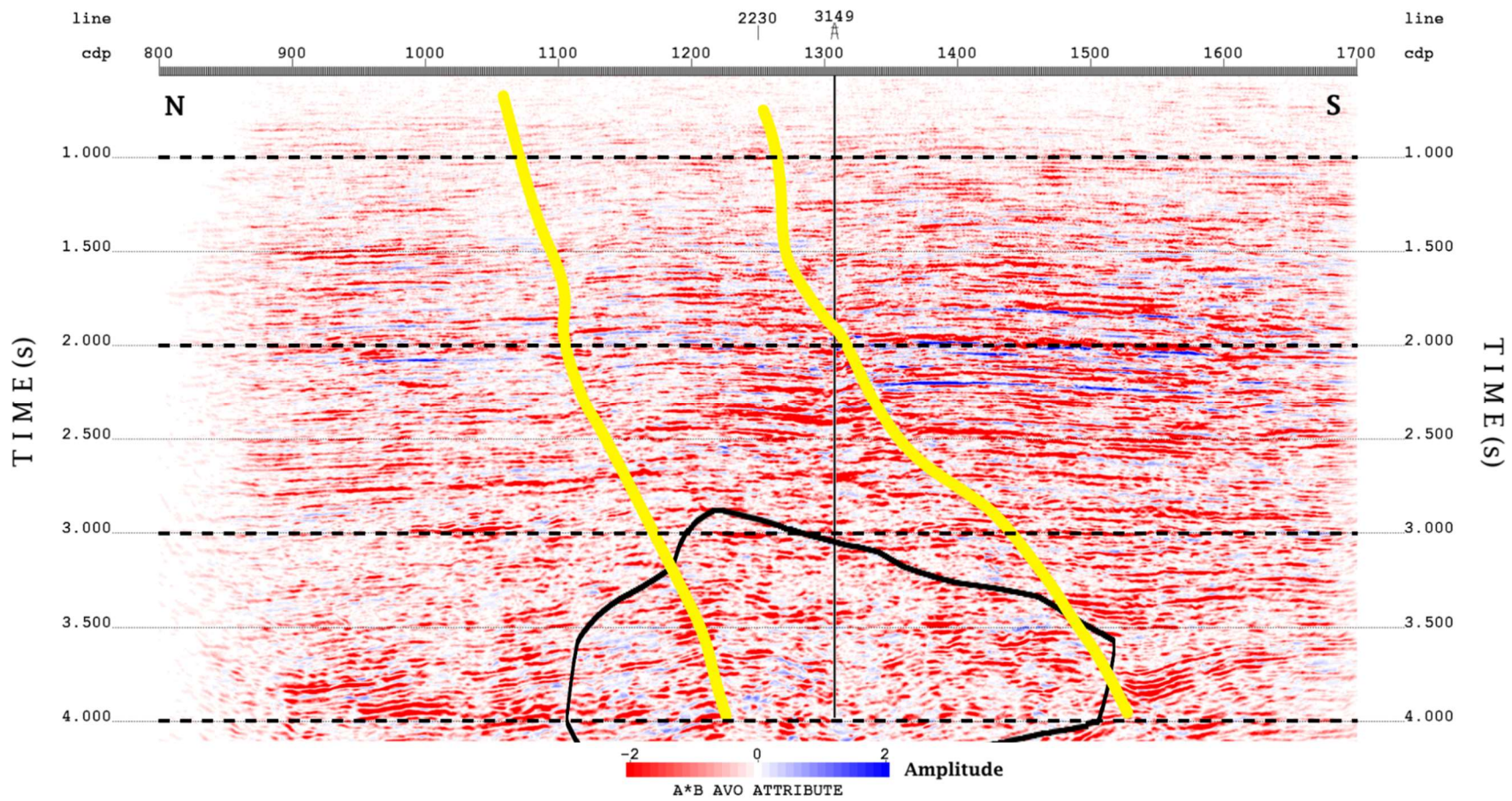


Figure 3.35 AVO A*B section tie with low velocity zone (black) and fault (yellow) locations

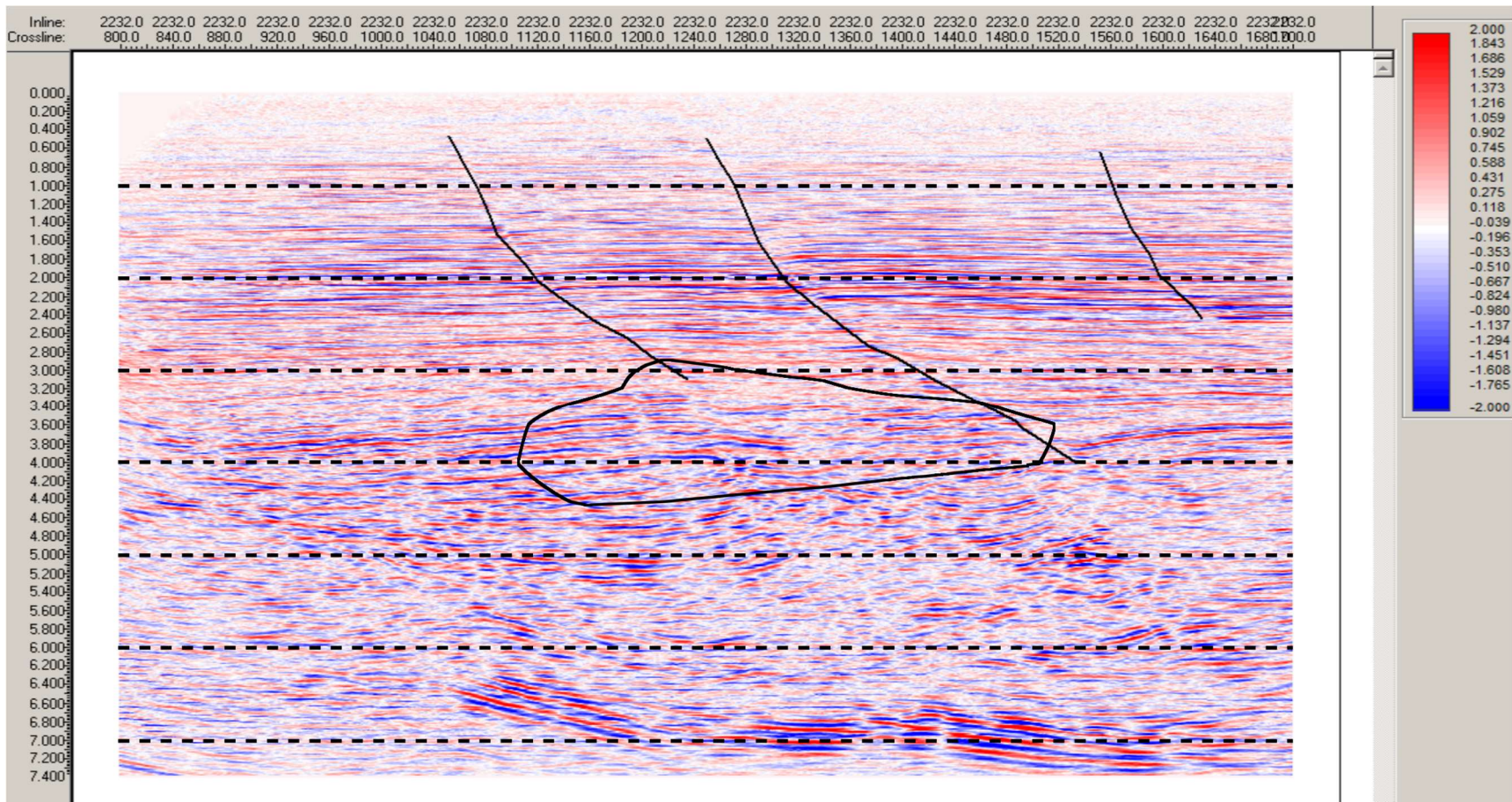


Figure 3.36 Full stack section with low velocity zone and fault locations annotated

4. DISCUSSION AND CONCLUSION

This exploration study in the Gulf of Mexico is a practical demonstration of integrating different geophysical tools. By using seismic data processing, AVO analysis, pore pressure analysis, and well log analysis, many insights were made into the subsurface geologic structure, pore fluid content, and the local pressure regime. The intent of this research was to tie all of these commonly used techniques together into a single workflow and clarify how they relate to each other. In terms of lessons learned, the success of an exploration project greatly depends on the quality of the velocity model building phase, which is directly tied to the results of processing, AVO analysis, pore pressure, and the well-tie. Since the velocity model is a physical representation of the subsurface conditions, the presence of an interpreter or a processor with interpretation experience who knows the geologic background or depositional history of the area can have a significant impact on velocity picking.

For the EI 26 survey specifically, there are several conclusions which can be made:

1. Rock-property attributes derived from well-log crossplots indicate a wide variety of rock-properties are suitable for discriminating pore-fluid type. Then, AVO synthetics indicated a Class III environment which means seismic amplitude on near, mid and far-offset stacks are useful for pore-fluid estimation. The seismic synthetic AVO inversion also showed that the intercept and gradient are Class III meaning A^*B will yield a large positive amplitude.
2. Conventional hydrocarbon exploration techniques have been generated and correlated to each other

3. Preserving seismic amplitude is important and a processing workflow was shown that accomplished this goal for recognizing Class III amplitudes.
4. Gas prospects in the 2.00 to 2.25s interval are noted in:
 - a. Two fault blocks
 - b. Near and mid offset stacks
 - c. A*B AVO anomaly stack
5. Gas prospects in the 2.00 to 2.25s interval are conformable with the integration of:
 - a. Pore-pressure anomalies
 - b. Structural fault block interpretation
 - c. AVO Offset stack amplitudes
 - d. Lithology prediction
 - e. HCI Attributes
 - f. Risk-reduction attributes of fluid boundaries (flat spots) and conformable amplitude and structure analysis
6. AVO synthetics and their rock-property and reflectivity attributes indicate a Class III environment. However, the product of intercept and gradient for gas sands appear to be affected by pre-stack noise
7. This study has produced two viable drilling locations for gas reservoirs

BIBLIOGRAPHY

- Aki, K, and PG Richards (1980). *Quantitative Seismology: Theory and Methods*. WH Freeman and Co.
- Archie, G. (1942). The Electrical Resistivity Log as an Aid in Determining Some Reservoir Characteristics. *Transactions of the AIME*, 146(01), pp.54-62.
- Ashton, Peter, Brad Bacon, Christian Deplante, Sinclair Thor, Mann Angus, Moldoveanu Nick, and Redekop Glen. 1994. "3D Seismic Survey Design." *Oilfield Review*.
- Avseth, Per, Tapan Mukerji, and Gary Mavko. 2005. *Quantitative Seismic Interpretation: Applying Rock Physics Tools to Reduce Interpretation Risk*. Cambridge, UK ; New York: Cambridge University Press.
- Boorman, C., M. Cowgill, E. Ginal, R. Mandley, J. Thompson, G. Roberts, and S. Archer, 2006, Huge potential still waiting in the Gulf of Mexico: *GEO Expro* Issue No. 4/5.
- Bowers, Glenn L. 2002. "Detecting High Overpressure." *The Leading Edge* 21 (2): 174–177.
- Bowers, Glenn L., and others. 1995. "Pore Pressure Estimation from Velocity Data: Accounting for Overpressure Mechanisms besides Undercompaction." *SPE Drilling & Completion* 10 (02): 89–95.
- Bruce, Bob, and Glenn Bowers. 2002. "Pore Pressure Terminology." *The Leading Edge* 21 (2): 170–173.
- Bruce, Clemont H. 1984. "Smectite Dehydration—its Relation to Structural Development and Hydrocarbon Accumulation in Northern Gulf of Mexico Basin." *AAPG Bulletin* 68 (6): 673–683.

- Burke, Lauri A., Scott A. Kinney, Russell F. Dubiel, and Janet K. Pitman. 2012. "Regional Map of the 0.70 Psi/Ft Pressure Gradient and Development of the Regional Geopressure-Gradient Model for the Onshore and Offshore Gulf of Mexico Basin, USA."
- Eaton, Ben A. 1972. "The Effect of Overburden Stress on Geopressure Prediction from Well Logs." *Journal of Petroleum Technology* 24 (08): 929–34.
- Ensley, Ross Alan. 1984. "Comparison of P-and S-Wave Seismic Data: A New Method for Detecting Gas Reservoirs." *Geophysics* 49 (9): 1420–1431.
- Freed, Robert, and Donald Peacor. 1989. "Geopressured Shale and Sealing Effect of Smectite to Illite Transition." *AAPG Bulletin* 73 (10): 1223,1232.
- Hilterman, Fred J. 2001. "Seismic Amplitude Interpretation." *SEG, EAGE*, 2001 Distinguished Instructor Short Course.
- Losh, S., Cathles L. 2009. Phase fractionation and oil-condensate mass balance in the South Marsh Island Block 208–239 area, offshore Louisiana. *Marine and Petroleum Geology* 27.2 (2010): 467-75.
- Morris, Scott, Brian Vestal, Kelsey O'Neill, Michael Moretti, Cesar Franco, Nathan Hitchings, Jianmin Zhang, and John D. Grace. 2015. "The Pore Pressure Regime of the Northern Gulf of Mexico: Geostatistical Estimation and Regional Controls." *AAPG Bulletin* 99 (01):91–118.
- National Oceanic and Atmospheric Administration (2017). Bathymetric Data Viewer. [image].
- Ostrander, W.J. 1984. "Plane-Wave Reflection Coefficients for Gas Sands at Nonnormal Angles of Incidence." *Geophysics* 49 (10): 1637–1648.
- Papoulis, A.,1962. *The Fourier integral and its applications*, 318 p., McGraw-Hill.

- Reymond, B. and Stampfli, G. (1996). Three-dimensional sequence stratigraphy and subtle stratigraphic traps associated with systems tracts: West Cameron region, offshore Louisiana, Gulf of Mexico. *Marine and Petroleum Geology*, 13(1), pp.41-60.
- Ross, Christopher P., and Daniel L. Kinman. 1995. "Nonbright-Spot AVO: Two Examples." *Geophysics* 60 (5): 1398–1408.
- Rutherford, Steven R., and Robert H. Williams. 1989. "Amplitude-versus-Offset Variations in Gas Sands." *Geophysics* 54 (6): 680–688.
- Sheriff, R. E., Geldart, L. P. (1995). *Exploration Seismology* (2nd ed.). Cambridge University Press. ISBN 0-521-46826-4.
- Shuey, R. T. 1985. "A Simplification of the Zoeppritz Equations." *GEOPHYSICS* 50 (4): 609–14.
- Swan, Herbert W. 2001. "Velocities from Amplitude Variations with Offset." *Geophysics* 66 (6): 1735–1743.
- United States Department of the Interior Mineral Management Service (2000). WESTERN GULF OF MEXICO PLANNING AREA LEASE SALE 177. [image].
- United States Department of the Interior Mineral Management Service (2008). Active Leases and Bids Received for Central Planning Area (CPA) Sale 206 Easter Planning Area (EPA) Sale 224. [image].
- Verm, R. and Hilterman, F. (1995). Lithology color-coded seismic sections: The calibration of AVO crossplotting to rock properties. *The Leading Edge*, 14(8), pp.847-853.
- Verm, Richard, Luh Liang, and Fred Hilterman. 1998. "Significance of Geopressure in Predicting Lithology." *The Leading Edge* 17 (2): 227–227.

- Wang, Zizhen, and Ruihe Wang. 2015. "Pore Pressure Prediction Using Geophysical Methods in Carbonate Reservoirs: Current Status, Challenges and Way Ahead." *Journal of Natural Gas Science and Engineering* 27 (November): 986–93.
- Wiggins, R., Kenny, G. S. and C. D. McClure, 1983, A method for determining and displaying the shear-velocity reflectivities of a geologic formation, 1983, European Patent Application 0113944.
- Yu, Hua. 2013. "Calibration of Effective Pressure Coefficient for the Gulf of Mexico." PhD Thesis, University of Houston.
- Zaman, S. (2017). REDUCING RISK IN LITHOLOGY AND FLUID DISCRIMINATION WITH ATTRIBUTES DERIVED FROM SEISMIC INVERSION. Master of Science. University of Houston - Department of Earth and Atmospheric Sciences.
- Zhang, Brown, and James Brown. 2001. "A Review of AVO Analysis." *CREWES Research Report* Volume 13.
- Zhang, Jincai. 2011. "Pore Pressure Prediction from Well Logs: Methods, Modifications, and New Approaches." *Earth-Science Reviews* 108 (1–2):50–63.
- Zhou, Hua-Wei. 2014. *Practical Seismic Data Analysis*. New York: Cambridge University Press.